



**HAL**  
open science

# Understanding, computing and identifying the nonlinear dynamics of elastic and piezoelectric structures thanks to nonlinear modes

Olivier Thomas

► **To cite this version:**

Olivier Thomas. Understanding, computing and identifying the nonlinear dynamics of elastic and piezoelectric structures thanks to nonlinear modes. Model Order Reduction for Design, Analysis and Control of Nonlinear Vibratory Systems, 2024, 10.1007/978-3-031-67499-0\_4 . hal-04596527

**HAL Id: hal-04596527**

**<https://hal.science/hal-04596527v1>**

Submitted on 4 Dec 2024

**HAL** is a multi-disciplinary open access archive for the deposit and dissemination of scientific research documents, whether they are published or not. The documents may come from teaching and research institutions in France or abroad, or from public or private research centers.

L'archive ouverte pluridisciplinaire **HAL**, est destinée au dépôt et à la diffusion de documents scientifiques de niveau recherche, publiés ou non, émanant des établissements d'enseignement et de recherche français ou étrangers, des laboratoires publics ou privés.



Distributed under a Creative Commons Attribution - NonCommercial 4.0 International License

# Understanding, Computing and Identifying the Nonlinear Dynamics of Elastic and Piezoelectric Structures Thanks to Nonlinear Modes

Olivier Thomas

**Abstract** This chapter addresses the computation and the experimental identification of the nonlinear dynamics of mechanical structures through the use of nonlinear modes. They enable to reduce the dynamics, for efficient computation as well as for qualitative understanding. An overview of the complex vibratory behaviours often observed when non-linearities are at hand is proposed through selected didactic examples, as well as a classification of the sources of non-linearities encountered in mechanical engineering. Then, a focus on geometrically nonlinear structures is proposed, since they show most of the classical nonlinear dynamical phenomena and are still a computation challenge. An overview of the main models of beams, plates and shells is proposed, as well as some finite-element discretisations. The case of a piezoelectric coupling with an electronic circuit is also considered. The several definitions of nonlinear modes are considered and compared, with a focus on the normal form method to compute a reduced order model. All the particular features of nonlinear modes are addressed, in the case of a simple dynamics involving a single mode, but also when several modes are strongly interacting through internal resonances. Numerical and experimental continuation methods are also addressed, as a mean of efficiently compute and identify the dynamics of the system. Finally, a few representative examples are proposed, with focuses on internal resonances, quality of reduced order models and piezoelectric structures computations.

## 4.1 Introduction

The central purpose of this article is to address the computation of the nonlinear dynamics of mechanical structures. Non-linearities bring a lot of complex dynamical phenomena that do not exist in the dynamics of linear systems. To cite a few of them, the characteristic frequencies (free oscillation frequencies or resonance frequencies) of a nonlinear system can change as a function of the amplitude of

---

O. Thomas (✉)

Arts et Métiers Institute of Technology, LISPEN, 59000 Lille, France  
e-mail: olivier.thomas@ensam.eu

the motion; several solution branches can coexist for a given forcing, giving rise to possible sudden jumps of amplitude; strong energy transfers between separate frequency bands can occur, thanks to harmonic (sub- or super-) resonances or internal resonances between modes; oscillations with complex frequency content, such as quasi-periodic or chaotic solutions, can occur; all those complex phenomena being linked to bifurcations and instabilities.

In this context, computing the dynamical behaviour of a nonlinear system brings several features. First, most of the algorithms dedicated to linear system computations fail in the case of non-linearities and must be adapted, to the price of more complexity, possible instabilities, and, more importantly, a huge increase of computation time. Even if time integration schemes are implemented and well mastered in modern commercial finite-element codes, because of the increased computation time and of the nonlinear phenomena enumerated above, blind computations in the case of a nonlinear system can lead the structural engineer to miss important features of the dynamics.

Then, efficiently computing the nonlinear dynamics of a structural system needs, currently, three ingredients. The first one is to qualitatively understand the possible nonlinear phenomena, enumerated above, that can be observed. Secondly, considering reduction methods seems mandatory. Several strategies exist to reduce the dynamics, but we focus here on those which attack directly the nonlinear characteristic of the system, based on the concept of nonlinear mode. Thanks to the invariant manifold approach, they have the advantages of giving reduction strategies that lead to either efficiently and quantitatively compute the dynamics, but also give a mean of qualitatively understanding the encountered nonlinear phenomena. Thirdly, dedicated computation methods are mandatory, such as continuation methods, to either assist or replace standard time integration methods available in most current finite-element software packages.

In this context, the purpose of this article is to give an overview of the use of nonlinear modes to qualitatively understand and quantitatively compute the dynamics of nonlinear structural systems. We will particularly consider structures subjected to geometrical non-linearities, since they are naturally subjected to most of dynamical phenomena and therefore constitute an easy illustration of them. We will also include linear piezoelectric coupling in the discussion since their mix with the geometrical non-linearities brings particular features and also interesting phenomena such as parametric resonances. Systems subjected to self-sustained oscillations won't be considered here, nor friction damped systems.

The text is also a mixture between (i) mathematical proofs, (ii) relevant examples to understand the mechanisms and (iii) general synthetic comments, that we hope as balanced and didactic as possible.

In Sect. 4.2, very general issues about non-linearities (their definition and smoothness, the associated physics encountered in solid mechanics, an overview of the phenomena they often create and finally an overview of the computation strategies) are addressed as a preliminary. In Sect. 4.3, the most common models of elastic and piezoelectric structures subjected to geometrical non-linearities are described. Then, the concept of nonlinear modes is addressed in details in Sect. 4.4, with a

particular focus on the normal form method, as a way of reducing and understanding the nonlinear dynamics of the geometrically nonlinear structures of Sect. 4.3. In Sect. 4.5, an overview of frequency domain continuation methods is proposed, both for efficient numerical computation and experimental identification. Finally, Sect. 4.6 gathers some test cases examples, with focus on the effect of the loss of transverse symmetry (curvature, lamination etc.) of a structure on the reduced-order modelling, on the topology of some frequency response in the case of internal resonances and on the reduced-order modelling of a piezoelectric structure.

## 4.2 Generalities

This section gathers a few general considerations about non-linearities, in general but also specifically in the field of solid mechanics.

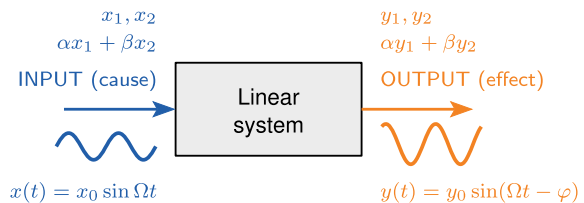
### 4.2.1 Definition of Non-linearities

Non-linearities are a feature related to a given model of a system or a phenomenon. They can take many forms and are usually defined by contradiction: one first defines properly a *linear system* and then defines a *nonlinear system* as any system that is *not linear*.

By definition, as illustrated in Fig. 4.1, a given system is said *linear* if it satisfies the *superposition principle*. It means that if two inputs  $x_1$  and  $x_2$  produce the two outputs  $y_1$  and  $y_2$ , then  $\alpha x_1 + \beta x_2$  produces the output  $\alpha y_1 + \beta y_2$ ,  $\forall \alpha, \beta \in \mathbb{R}$ . The system is *non-linear* in any other cases.

When the considered system has a given dynamics, meaning that the input  $x(t)$  and output  $y(t)$  are functions of time  $t$ , if the system is *linear*, its behaviour can be described by *linear* equations (often a Partial Differential Equation (PDE), or a set of Ordinary Differential Equations (ODE), or if constraints are included, a set of Differential Algebraic Equations (DAE)). Then, considering a sinusoidal input  $x(t) = x_0 \cos \Omega t$  (with angular frequency  $\Omega$  and amplitude  $x_0$ ), the linearity of the systems results in an output which is *also a sinusoidal function*, oscillating at the *same frequency*  $\Omega$  ( $y(t) = y_0 \cos(\Omega t + \varphi)$ , with  $y_0(\Omega)$  its amplitude and  $\varphi(\Omega)$  its

**Fig. 4.1** A linear system

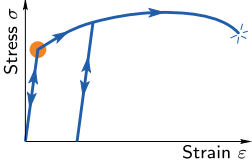

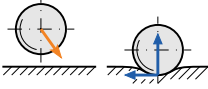
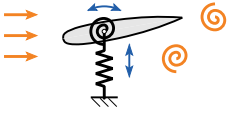


phase, often functions of  $\Omega$ ). This means that the output of a *nonlinear system* to a sinusoidal input is often not sinusoidal. It can be periodic at the same frequency  $\Omega$ , showing harmonic distortion, can be quasi-periodic or even much more complex in the case of chaos. Illustrations will be given in the following.

### 4.2.2 An Overview of Non-linearities in Solid Mechanics

The present section gives an overview of several causes, sources and physical mechanisms that give birth to non-linearities. A classification is proposed, viewed from the side of solid mechanics. The sources of non-linearities are gathered in four families as summarised in Table 4.1. The first three ones (material, geometric and contact) are usual and are often used to organize the computation procedures in standard finite-element commercial simulation software packages (see e.g. Abaqus (2024)).

**Table 4.1** Overview of non-linearities in solid mechanics. S/NS means smooth/non-smooth and C/NC means conservative/non-conservative

Type of non-linearity	Examples	Smoothness	Conservativity
<b>Material</b> Nonlinear constitutive law 	Elasto-plastic (metals...) Hyperelastic (elastomers...) Shape memory alloys	NS S NS	NC C/NC NC
<b>Geometric</b> Large deflection 	Multibody systems Thin structures	S S	C C
<b>Contact</b> 	Hertz law Dry friction Shocks	S NS NS	C NC C/NC
<b>Coupling</b> (fluids, electricity...) 	Aeroelastic oscillations Aeroelastic damping Electrostatic Piezoelectric Electromagnetic	S NS S NS S	NC NC C C/NC C/NC

The last one, about the coupling of solid mechanics to other physical domains such as fluid mechanics or electrical engineering, is less standard, but mandatory since typical non-linearities arise because of these couplings.

**Material nonlinearities:** in this case, it is the *constitutive law* (in mechanics, it is the stress-strain law) of the material which is non-linear. Typical examples are:

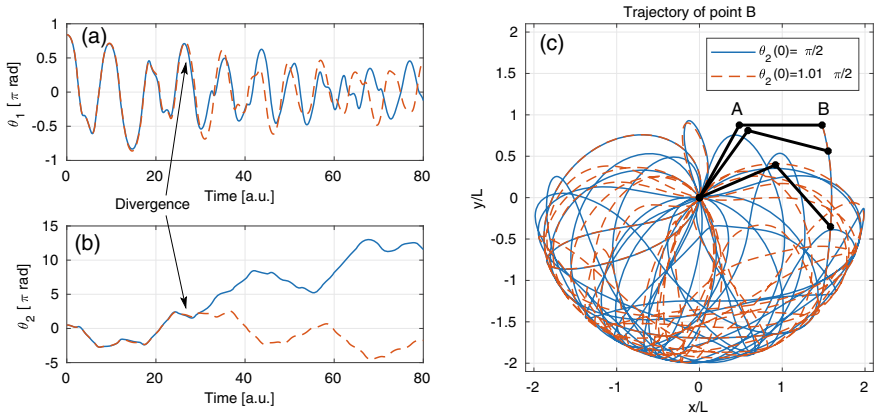
- *elasto-plastic materials*: the transition from elastic to plastic deformations corresponds to a *non-smooth* stress-strain law; plastic deformations are *irreversible* and manifest themselves through an *hysteretic behaviour* since they depend on the history of the transformation. Those three characteristics are non-linear. Locally, the plastic part of the stress-strain law is very similar to the  $(F_c, x)$  graph of the Coulomb law for dry friction considered in Sect. 4.2.3. Most metals exhibit this behavior when stresses exceed their yield point.
- *nonlinear elastic materials*: in this case, the path of deformation is perfectly reversible (elasticity) and smooth, but it is the stress-strain relationship that is non-linear. It is often modeled with a hyperelastic constitutive law, for which the elastic forces derives from a potential energy (Ogden 1997). These materials are also generally highly dissipative because of visco-elasticity (which can be considered as linear, Morin et al. (2018)). Elastomers and rubber materials fall into this family.
- *shape memory alloys*: these materials are subjected to metallurgical phase changes according to the stresses and strains applied to them as well as the changes in temperature (thermal coupling). Their main nonlinear characteristic is that the stress/strain relationship exhibits hysteresis and is also non-smooth (see e.g. Lacarbonara et al. (2004)).

**Geometric non-linearities:** they are observed when the system encounters a *large change of configuration* (due for instance to large displacement/deformations), for which the geometry change of the system under loading cannot be neglected because it influences the force distribution into the system. The most known manifestation of geometrical non-linearities is buckling, for which a loading in one direction creates a response of the structure in an orthogonal direction. More generally, geometric non-linearities are encountered in two families of systems.

- *Multibody systems*: this family includes all systems modeled as rigid solids connected together by joints. Non-linearities arise from large rotations of the system components relative to one another, which create nonlinear relationships between the forces in the joints and the generalised coordinates of the system. The simplest example is a pendulum in a gravity field: in this case, the restoring force is non-linear as a function of the pendulum's angle  $\theta$  with the gravitational acceleration vector:  $F = mg \sin \theta$  (with  $m$  the pendulum's mass and  $g$  the gravitational acceleration), coming from the projection of the gravity force onto the tangent to the pendulum's trajectory. For small angle,  $\sin \theta \simeq \theta$  and  $F$  is linear in  $\theta$ . For large  $\theta$ , this approximation is no longer valid since  $F$  increases less than  $mg\theta$  when  $\theta$  is large, because of the projection effect ( $\sin \theta < \theta$  for  $\theta \in [0, \pi]$ ). It leads to a

well known softening nonlinear effect, illustrated in Fig. 4.4. Another example is a double pendulum which is well known for its chaotic behaviour in free vibrations. It is illustrated in Fig. 4.2, obtained by numerical time integration of the equations of motion. Two time evolutions of the system are shown, for two slightly different initial conditions, showing the classical sensitivity of chaotic systems to a change in the initial conditions: on the initial time interval  $t \in [0, 26]$ , the two time evolutions are approximately identical, whereas after, they diverges from each other, showing two completely different trajectories.

- *Thin structures:* the cause of non-linearity is analogous to the one for multibody systems: the large rotations of the deformable fibers create nonlinear relationships between displacements and strains in the structure, due to the redistribution of forces linked to the change of geometry. Those non-linearities are most commonly associated to thin structures (beams, plates, shells...), due to their low transverse stiffness, which allows large displacements obtained for moderate external forces. On the contrary, massive structures are too rigid in all directions, which in practice prevents the occurrence of large displacements and therefore the manifestation of geometric non-linearities. Geometric non-linearities in thin structure will be specifically addressed in Sect. 4.3.



**Fig. 4.2** Free oscillations of a double pendulum for two slightly different initial conditions; ‘—’:  $\theta_1(0) = 0.84\pi$ ,  $\theta_2(0) = \pi/2$ ; ‘- -’:  $\theta_1(0) = 0.84\pi$ ,  $\theta_2(0) = 1.01\pi/2$ , with  $(\theta_1, \theta_2)$  the angles of the two members of the system. Both members have the same length. **a, b** Time evolution of  $\theta_1$  and  $\theta_2$ ; **c** Trajectory of the tip  $B$  of the second member in the physical plane of motion of the system. Three configurations of the system are also shown, at  $t \in \{0, 0.79, 1.59\}$

In many engineering applications, geometric non-linearities are linked to material non-linearities. In the case of metal forming and crash tests, thanks to plasticity, the large change of geometry leads undoubtedly to geometric non-linearities. Rubber bushings, used as vibration isolator, are also linked to large strains associated to their nonlinear elastic behaviour.

**Contact non-linearities:** they appear at the interface between several solid components of a system. One can gather them into three families.

- *Localised contact:* when the contact surface between two elements is reduced in size (we often talk of non-conformal contact), the size of the contact area depends on the relative displacement of the two elements, resulting in a nonlinear relationship between this displacement and the associated force. This is well predicted by Hertz's theory (for example, the contact force  $P$  between two elements in point contact is of the form  $P = K \delta^{3/2}$  with  $\delta$  the relative displacement of the elements and  $K$  a constant (see e.g. Johnson (1985)). This appears in practice in the case of joints with rolling elements or gears.
- *Dry friction:* when two elements of a system are in non-lubricated contact, we observe alternations between sticking and slipping situations, which creates a non-smooth relationship between friction force and sliding speed, as illustrated in Sect. 4.2.3.
- *Intermittent contact:* if two elements are linked with unilateral joints, dynamic forces can create alternations between times of loss of contact and elastic penetrations, creating shocks. Those non-linearities are also non-smooth by nature.

**Coupling non-linearities:** they are encountered when the behaviour of a given mechanical system is coupled to another physical field, such as a fluid or an electronic circuit, through an electromechanic transducer. Those non-linearities can be issued from the other physical domain, or because of the coupling. Five families of problems are reported here.

- *Aeroelastic oscillations:* when a flexible structure is subjected to a fluid flow, a strong coupling can occur such that the oscillations of the structure produce a change in the fluid flow that in return modifies the pressure on the structure in such a way that the oscillations are amplified. This leads to self-sustained oscillations of the structure, often of large amplitude, named generally flow induced vibrations. Examples are aeroelastic flutter, vortex induced vibrations... (see e.g. Païdoussis et al. (2011), Amandolèse et al. (2024)).
- *Aeroelastic damping:* it is caused by the aeroelastic drag resulting from the motion of a body into a fluid. It creates a force basically proportional to the square of the relative velocity of the body and the fluid, and always opposed to the motion. In the case of a one dimensional motion of amplitude  $x(t)$ , this effect adds the quadratic non-smooth term  $|\dot{x}|\dot{x}$  in the equations. Qualitatively, the non-linearity manifests itself by the amplitude of the damping force, which increases with the square of the oscillations of the body (see e.g. Colin et al. (2020), Debeurre et al. (2024a)).

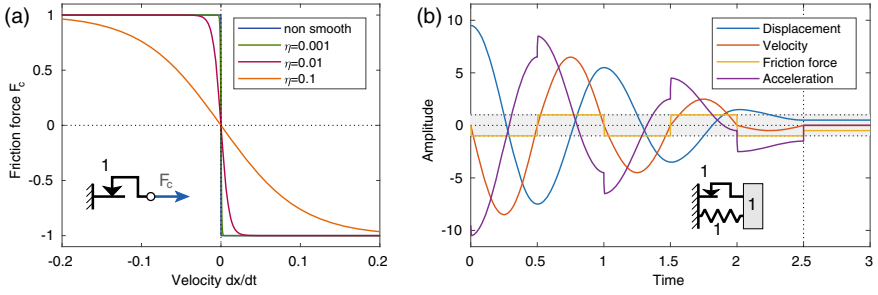


- *Electrostatic coupling*: this is the most common effect used to couple the deformations of an elastic body to an electronic circuit in Nano/Micro Electro Mechanical Systems (N/MEMS). Indeed, it is easy to implement and becomes powerful at small scales because of size effects. Basically, a movable electrode electric capacitive effect is created between two electrodes, one on the moving body and one on the ground. The non-linearities are then intrinsic to the coupling since the mechanical forces are inversely proportional to the gap between the two electrodes, and thus to the distance between the body and the ground (see e.g. Younis (2011), Corigliano et al. (2018) and Chap. 3 this book).
- *Piezoelectric coupling*: this coupling appear in certain materials that have the property to create electric charges when deformed. This transformation being thermodynamically reversible, the inverse effect is possible: when subjected to an electric field, the piezoelectric material deforms. Piezoelectric materials are widely used as sensors or/and actuators for vibration measurement, monitoring and control (Preumont 2011), clock reference oscillators (Bottom 1982) or more recently in N/MEMS (refer to the third chapter of this book). The coupling appears in the constitutive law, that links the mechanical fields (stress and strain) to the electrical fields (electric field and displacement), as addressed in Sect. 4.3.4. In a lot of applications, this constitutive law is considered linear. However, nonlinearities can be easily observed in experiments (see Givois et al. (2020a), Frangi et al. (2020)) and modelled in the form of non-smooth terms that include absolute values of the unknowns (see Leadenham and Erturk (2015)).

### 4.2.3 Smooth and Non-smooth Non-linearities

An important feature of the non-linearities introduced in the previous section is their *smoothness*, that has important consequences both in term of phenomenology and for computational issues.

To be precise, the smoothness is a characteristic of the model of a non-linearity. It is said smooth if the mathematical functions included in its governing equations are continuous, with a number of their derivatives which are also continuous. As illustrated in Table 4.1, a number of non-linearities can be naturally modelled by non-smooth laws, like in the case of contact non-linearities in mechanical systems or for modelling diodes, switches or saturated electronic components in electrical engineering (refer to Acary and Brogliato (2008) for examples in electrical engineering and Shami et al. (2023a) for an application in vibration damping using a diode).



**Fig. 4.3** **a** Dry friction force as a function of the velocity in the case of a classical Coulomb law with friction coefficient  $\mu = 1$  (Eq. (4.1)). Effect of the regularisation parameter  $\eta$  on the regularised law (4.2). **b** Free oscillations of a mass spring system with a Coulomb damper, of ordinary differential equation  $\ddot{x} + x - F_c(\dot{x}) = 0$ , with  $\mu = 1$ . Position  $x$ , velocity  $\dot{x}$ , acceleration  $\ddot{x}$  and friction force  $-F_c$  as a function of time

A typical example of a non-smooth law is the Coulomb law for dry friction, for which the friction force  $F_c$  can be written as:

$$\begin{cases} F_c = -\mu & \text{if } \dot{x} > 0, \\ F_c \in [-\mu, \mu] & \text{if } \dot{x} = 0, \\ F_c = \mu & \text{if } \dot{x} < 0, \end{cases} \quad (4.1)$$

where  $\mu$  is a friction coefficient. The non-smooth characteristics of this law appears with the multivalued part at zero velocity ( $\dot{x} = 0$ ), for which the friction force can take any value in  $[-\mu, \mu]$ , depending on the equilibrium of the system. This law is shown in Fig. 4.3a.

From a physical point of view, non-smooth non-linearities can be responsible for discontinuities, leading to jumps in the time evolution of the generalised coordinates (and their time derivatives) of the system. Figure 4.3b shows the free oscillations of a mass-spring system with a Coulomb damper, in which the acceleration has discontinuities at each change of sign of the velocity. This also leads to a complete change of the topology of the bifurcations, for which the smoothness of the response curves in the frequency domain is lost (see Leine and Nijmeijer (2004)).

From a computational point of view, most of the standard solvers, in particular the time integrators, are naturally designed for smooth laws and don't work for non-smooth models if written directly as in Eq. (4.1). It is however possible to regularize the non-smooth models by replacing it with smooth functions. An example is shown in Fig. 4.3a where the law  $(F_c, \dot{x})$  is replaced by the function:

$$F_c = \mu \tanh(-\dot{x}/\eta), \quad (4.2)$$

with  $\eta \in \mathbb{R}^+$  a regularisation parameter. As illustrated in Fig. 4.3a, if  $\eta \rightarrow 0$ , the function (4.2) tends to the Coulomb law (4.1). Then, choosing  $\eta$  small leads to approximate the Coulomb law by a smooth function that can be directly applied to standard numerical solvers. In particular, we experimented using a Runge-Kutta algorithm (i.e. `ode45` in Matlab (2017)) with  $\eta < 10^{-2}$  that no noticeable difference was observed in  $x(t)$ ,  $\dot{x}(t)$ ,  $\ddot{x}(t)$  and  $F_c(t)$ <sup>1</sup> with respect to the exact analytical piecewise solution. One could also notice that this regularised law is also sometimes closer to the real behaviour of a system subjected to a solid/solid contact, that always has a certain compliance. However, despite its apparent advantage, this regularised law depends on the parameter  $\eta$  that must be chosen in practice. It is also highly numerically stiff, leading to possible numerical issues in the case of more complex models, in term of dynamics and number of degrees-of-freedom than the one of Fig. 4.3. It is then often interesting to keep the non-smooth law (4.1) and to adapt the numerical tools, at the price of an increased complexity of the mathematical tools (functions are set-valued, differential equations become differential inclusions...).

In Table 4.1, the smoothness of each source of non-linearity is indicated. The present article will consider only smooth non-linearities and the interested reader can refer to the textbooks Leine and Nijmeijer (2004), Acary and Brogliato (2008) and to Chaps. 5 and 6 of the present book.

#### 4.2.4 Overview of Nonlinear Dynamical Phenomena

In this section, a rapid overview of the nonlinear dynamical phenomena that can be encountered in practice is given. Two families of nonlinear systems can be considered.

- Systems subjected to *self-sustained oscillations*: in this case, the input of the system is *independent of time* whereas the output is oscillatory. It is at least periodic and can be more complex, with a spectrum composed of several non-commensurable frequencies, or even chaotic in some cases. The oscillations appear after a Hopf bifurcation. This kind of phenomena appears classically in the case of flow induced vibrations and of dry friction with alternating stick and slip phases.
- Systems subjected to an input that depends on time, called *externally excited*. The input can be an impact, leading to free oscillations of the system, simply a sine (or periodic) signal in the case of rotating machinery or with a more complex time evolution such as the effect of a turbulent fluid (water or wind) on a structure.

The case of self-sustained oscillations will be left apart in the present article, in favor of externally excited systems.

---

<sup>1</sup> A slight drift in  $F_c(t)$ , that should remain constant in theory, was however noticed in the last stick phase for  $t > 2.5$  for not small enough regularisation parameter  $\eta < 5 \cdot 10^{-3}$ , a direct consequence of the regularisation.

In order to illustrate and introduce various nonlinear dynamical phenomena, two systems are considered in this section: firstly a simple one degree-of-freedom pendulum, with results stemming from basic time integration of the equation of motion, and then a shell of revolution harmonically forced, with experimental results.

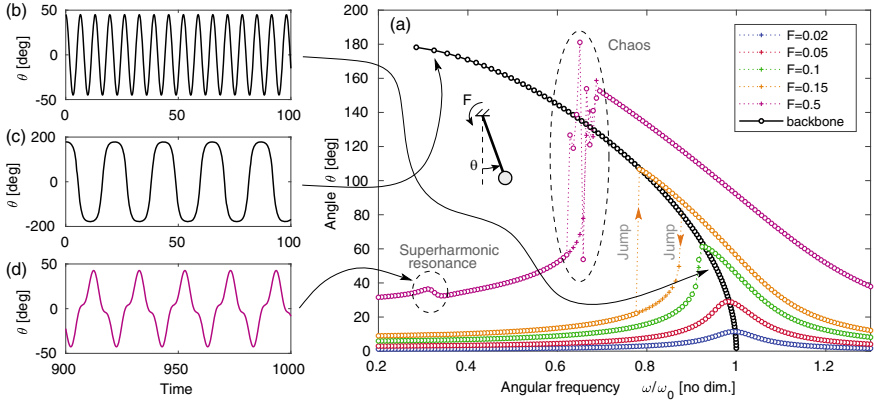
**A one degree-of-freedom system** As an elementary numerical experiment, we consider a pendulum in a gravity field whose angle with respect to the gravitational acceleration vector is denoted by  $\theta(t)$ , of non-dimensional equation of motion:

$$\ddot{\theta} + 2\xi\dot{\theta} + \sin\theta = F \cos\omega t, \quad (4.3)$$

with  $\xi$  the damping ratio and  $(F, \omega)$  the forcing level and frequency. We first look at its free undamped oscillations under non-zero initial angle  $\theta_0$  and initial zero velocity, i.e. with  $(\xi, F) = (0, 0)$ . The evolution of  $\theta$  as a function of time  $t$ , computed here with a Runge-Kutta algorithm (ode45 in Matlab (2017)), is always periodic, with a fundamental frequency denoted by  $\omega$ . If the system were linear,  $\theta(t)$  would be a purely sine function of frequency  $\omega = \omega_0$  (the natural frequency of the system, equal to  $\omega_0 = \sqrt{g/l} = 1$  in this case,  $g$  being the gravitational acceleration and  $l$  the length of the pendulum). On the contrary, because of the geometrical nonlinearities (see Sect. 4.2.2), (i)  $\omega$  is a decreasing function of the initial condition  $\theta_0$  (a so called *softening behaviour*) and (ii) the frequency content of  $\theta(t)$  *becomes richer* when  $\theta_0$  is increased. This is illustrated in Fig. 4.5a–c, which show the curve  $(\theta_m, \omega)$  (the so called *backbone curve*), with  $\theta_m$  the maximum value of  $\theta(t)$  over one period, as well as  $\theta(t)$  for two initial conditions, where the change of frequency and harmonic content is obvious (notice the increase of the period of oscillations and the “rounding” of  $\theta(t)$  (because of harmonic distortion) in Fig. 4.5c).

We now move to damped and forced oscillations of the pendulum, by applying a harmonic torque at the hinge with a viscous damping force, i.e. with  $(\xi, F) \neq (0, 0)$  in Eq. (4.3). We simulate by time integration a stepped sine experiment: it consists in choosing a frequency of excitation  $\omega$  and a forcing level  $F$ , computing  $\theta(t)$ , picking up its maximum amplitude  $\theta_m$  in the steady state and doing this operation for a list of successive frequencies  $\omega$ , in an increasing (upward stepped sine) or decreasing (downward stepped sine) order, around the resonance. By choosing the initial conditions at a given frequency step equal to the final state of the pendulum at the previous step, and also choosing an integer number of periods for each step, one obtains the curves  $\theta_m = f(\omega)$  shown in Fig. 4.4a. The first observation is that the obtained resonance curves are bent to the left and follows the shape of the backbone curve, being coincident with it close to the resonance points. Moreover, at high levels, it exist a frequency band in which two solutions coexist for a given driving frequency  $\omega$ : one of high amplitude, obtained by a downward stepped sine, and one of low amplitude, obtained by an upward stepped sine.

In fact, as will be discussed in Sect. 4.5 and observed in Figs. 4.15, 4.18 and 4.19, a third solution exists in theory, but since it is unstable, it cannot be computed by simple time integration as done here. This existence of *multiple solutions* is responsible for an hysteretic behaviour and *jump phenomena* under frequency sweeps. In addition,



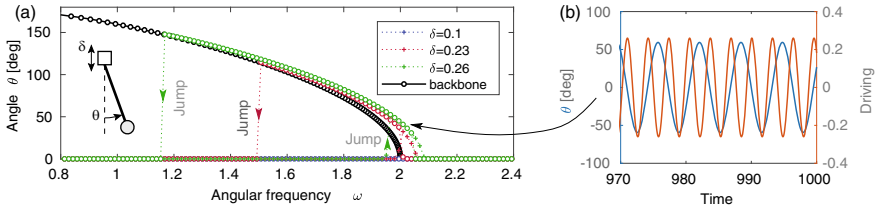
**Fig. 4.4** Oscillations of a simple pendulum in a gravity field, of Eq. (4.3), obtained by stepped sine time integration. **a** Maximum amplitude of the oscillations in the steady state as a function of the frequency  $\omega$ . The undamped free oscillations (backbone curve) are shown by the black curve and the forced oscillations in colored curved, each curve corresponding to a given forcing level  $F$  (damping ratio  $\xi = 0.01$  and forcing level  $F \in \{0.02, 0.05, 0.1, 0.15, 0.5\}$ ). ‘o’: downward stepped sine; ‘+’: upward stepped sine. **b**, **c** Time evolution of the angle  $\theta(t)$  for two points on the backbone curve; **d**  $\theta(t)$  at the superharmonic resonance for  $F = 0.5$  in the steady state

plotting  $\theta(t)$  in this forced experiment would lead to similar graphs than those of Fig. 4.4b, c, showing that the nonlinearities create a *harmonic distortion*: an input sine signal leads to a periodic output with non-zero harmonic components. Moreover, at the largest simulated amplitude ( $F = 0.5$ ) in Fig. 4.5, *chaotic oscillations* are observed. They emerge from a cascade of period-doubling bifurcations, see Bryant and Miles (1990). Finally, at the same forcing level, a small secondary resonance appears around  $\omega \simeq 0.3$ . It is called a *super-harmonic resonance* since in this case, the third harmonic of  $\sin \theta(t)$  ( $3 \times 0.3 \simeq 1$ ) in the equation of motion can be viewed as a forcing signal that drives the oscillator close to its resonance, creating a strong  $3\omega$  component in  $\theta(t)$ , visible in Fig. 4.4d (see also Volvert and Kerschen (2022)).

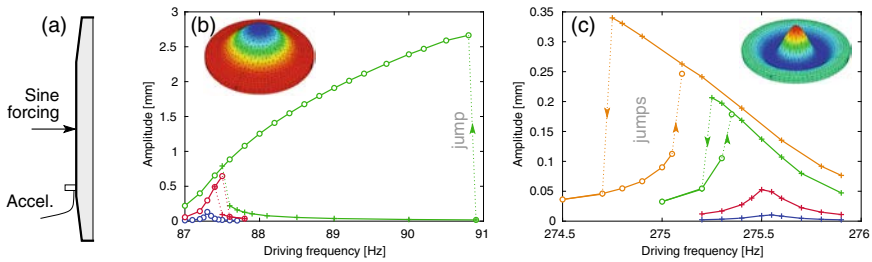
Another way of producing oscillations is to shake harmonically the pendulum in a direction parallel to the gravitational acceleration, with a signal  $\delta \cos \omega t$ . This produces a so-called *parametric excitation* of the pendulum since it is equivalent to modulating the gravity acceleration with this signal. The scaled equation of motion reads:

$$\ddot{\theta} + 2\xi\dot{\theta} + (1 + \delta \cos \omega t) \sin \theta = 0. \quad (4.4)$$

In this case, it is clear that the trivial solution  $\theta(t) \equiv 0 \forall t$  is admissible. However, above a certain threshold of the driving amplitude  $\delta$ , the trivial solution becomes unstable after a period doubling bifurcation, giving birth to a sub-harmonic oscillatory solution for  $\theta(t)$ , of fundamental frequency  $\omega/2$ , as shown in Fig. 4.5b. Performing a stepped sine numerical computation results in the resonance curves of Fig. 4.5a, usually called *parametric resonances*, which are bended to the left and follow the



**Fig. 4.5** Oscillations of a simple pendulum in parametric driving, of equation  $\ddot{\theta} + 2\xi\dot{\theta} + (1 + \delta \cos \omega t) \sin \theta = 0$ , obtained by time integration at fixed frequency  $\omega$ . **a** Maximum amplitude of the oscillations in the steady state as a function of the frequency  $\omega$ . The undamped free oscillations (backbone curve) are shown by the black curve and the forced oscillations in colored curves, each curve corresponding to a given forcing level  $\delta$  (damping ratio  $\xi = 0.01$  and forcing level  $\delta \in \{0.1, 0.23, 0.26\}$ ). ‘o’: downward stepped sine; ‘+’: upward stepped sine. **b** Time evolution of the angle  $\theta(t)$  and the driving  $\delta \cos \omega t$  for one point close to the parametric resonance for  $\delta = 0.26$  in the steady state

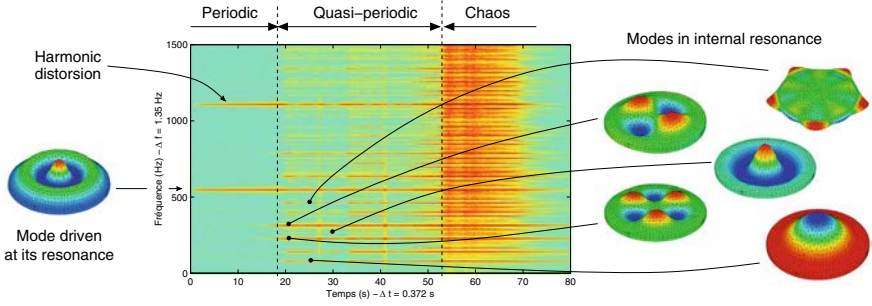


**Fig. 4.6** Experimental forced response of a chinese gong around its two first axisymmetric resonances obtained by stepped sine measurement. **a** cutaway view of the structure showing the driving at center and the acceleration measurement; **b**, **c** resonance curve of the first and second axisymmetric modes and their deformed shape, from a finite-element computation. Each color correspond to a given (constant) level of the forcing. ‘o’: upward stepped sine; ‘+’: downward stepped sine (from Chaigne et al. (2005))

backbone curve and cross it close to the resonance points. An example of parametric resonance of a piezoelectric structure will be addressed in Sect. 4.6.5.

**A continuous system** We now consider a more complex example: the forced response of a thin shell. This example is taken from Chaigne et al. (2005), in which the vibrations of an orchestral gong (a musical instrument also known as chinese tam-tam), known for its strong nonlinear vibratory and acoustic behaviour, is addressed. It has the form of a thin shell of revolution with a profile sketched in Fig. 4.6a. In the experiment, it is subjected to a sine forcing in the middle (created by a coil/magnet exciter) and the vibrations are measured by an accelerometer. Because of the symmetry of revolution, the mode shapes can be gathered into two families. The first one includes all the modes with an axisymmetric shape, that have only nodal circles, whereas the second groups all the others, that have an asymmetric shape with nodal diameters. Some mode shapes are shown in Fig. 4.7.

We first consider a stepped sine experiment, as explained above in the case of the pendulum, to measure the resonance curves of the two first axisymmetric modes.



**Fig. 4.7** Spectrogram of the acceleration signal of the chinese gong of Fig. 4.6 under sine excitation at fixed frequency (556 Hz, at the third axisymmetric resonance) and slowly increasing amplitude. Mode shapes of the modes involved in the vibration response (from Chaigne et al. (2005))

As shown in Fig. 4.6b, c, the same hysteretic behaviour as in the case of the pendulum is observed. However, the resonance curve of the first mode bends to the high-frequencies (Fig. 4.6b), whereas the one of the second mode bends to the low frequencies, leading respectively to so-called *hardening* and *softening* behaviours.

We now consider another experiment, with the same setup (Fig. 4.6a), in which we drive the shell by a sine signal of fixed frequency  $f_{dr}$ , chosen at the resonance of the third axisymmetric mode ( $f_{dr} = 556$  Hz), and with a slowly increasing amplitude. Figure 4.7 shows the time/frequency plot (spectrogram) of the measured acceleration signal, showing three successive vibratory behaviour. At low forcing amplitude (remember that the forcing increases with time), the response of the structure is *periodic* at fundamental frequency  $\omega$ , with an *harmonic distortion* that increases with the forcing level. Then, for a certain forcing amplitude, a sudden transition (a bifurcation, at  $t \simeq 17$ s) leads to the appearance in the spectrum of subharmonics, two at the beginning and then up to nine for a higher forcing level. Looking at the values of the frequencies, one can observe that they fulfill the following *internal resonance* relationship:

$$f_{dr} = 2f_i = f_j + f_k, \quad (4.5)$$

with  $f_i, f_j, f_k$  three subharmonic frequencies. Since those frequencies (except  $f_i$ ) are non-commensurable with  $f_{dr}$ , the obtained vibration signal is by definition *quasi-periodic*. Moreover, it can be shown that the values of  $f_i, f_j, f_k$  are all very close to the natural frequencies of some modes of the shell, whose mode shapes are shown in Fig. 4.7. Finally, a second bifurcation appears for a higher forcing level (at time  $t \simeq 53$  s), giving rise to a more complex vibratory response with a continuous frequency spectrum. It is a strongly *chaotic response*, known as *wave turbulence*, by analogy to what appends in a fluid (Cadot et al. 2016).

To conclude this section, the chosen examples highlight the main nonlinear phenomena that are commonly encountered in dynamics. As a summary, non-linearities are often responsible for:

- the possible appearance of three kind of responses, of increasing complexity: *periodic*, *quasi-periodic* or *chaotic*;
- the bending of the resonance curves, leading to hysteresis, *jumps during sine sweeps*, characterised by a *hardening* or *softening* behaviour;
- the appearance of *instabilities* and *bifurcations*;
- the appearance of *secondary resonances*;
- the creation of *new frequencies* in the output spectrum of the system:
  - at least *harmonic distortion* for a one mode response, but also
  - *sub- and super-harmonics* (periodic response) and *non-commensurable frequencies* (quasi-periodic response) linked to energy transfers between the modes of the structure, in particular because of *internal resonances* or
  - a full continuous spectrum (chaotic response), also facilitated if internal resonances are present (see Touzé et al. (2011)).

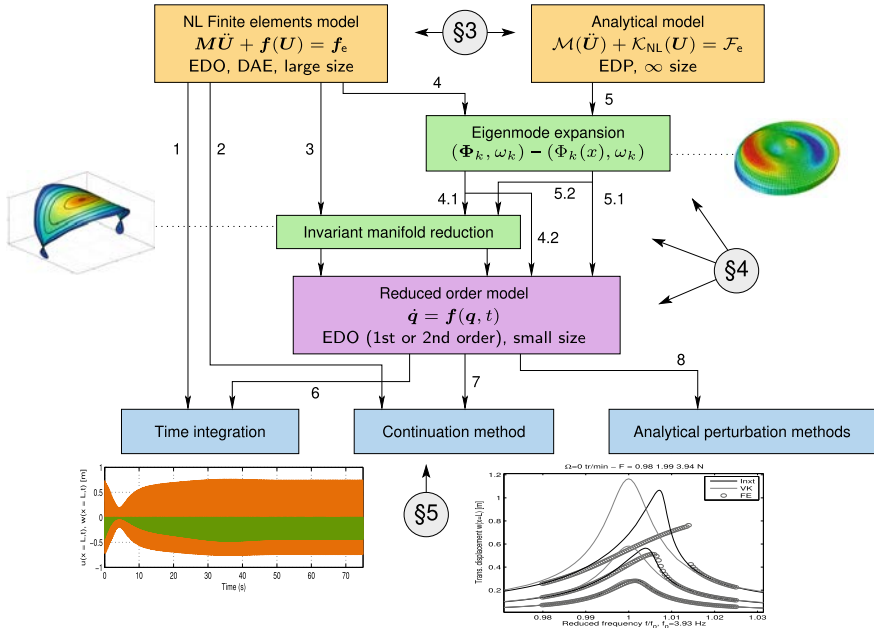
As discussed in the introduction, these nonlinear phenomena are very rich and often complicate the process and the analysis of numerical computation. The above catalogue can be viewed as a map, in particular to guide the analyst in designing a suitable reduced-order model. The remaining of the article will address those phenomena, both qualitatively and quantitatively.

#### 4.2.5 Computation Strategies

Various strategies are available to compute the nonlinear response of a system, summarised in Fig. 4.8. We focus here on the vibrations of a deformable body. The basic way of computing the dynamics of a system is to rely on time integration, either with powerful algorithms dedicated to small size first order dynamical equations (EDOs), path 6 of Fig. 4.8 (such as the Runge-Kutta family of algorithms, see e.g. Hairer et al. (2008)) or to algorithms dedicated to second order EDOs and implemented in finite-element codes, path 1 of Fig. 4.8 (see the Newmark and HHT families of algorithms, G eradin and Rixen (2015)). However, targeting the nonlinear behaviours enumerated in Sect. 4.2.4 with *time integration* can be very time consuming (even impossible for large size finite-element models) and does not provides insights on instabilities, bifurcations, multiple possible solutions and frequency domain steady states in a robust way, as *continuation methods* do. As discussed in Sect. 4.5, these methods, dedicated to nonlinear dynamics computations, are available as open source codes well suited for small size systems (path 7 of Fig. 4.8). For large size finite-element models (path 2 of Fig. 4.8), no commercial solutions exist at the moment; some private codes exist (see Blahoř et al. (2020)) but the computation time remain huge. For small size reduced-order models (1, 2 or 3 degrees-of-freedom, it is also possible to use analytical perturbation methods (see e.g. Nayfeh and Mook (1979), Sanders et al. (2007)).

In front of these huge computation times necessary for direct simulations of finite-element models, several reduction methods have been developed. Tradition-





**Fig. 4.8** Flowchart of several possible strategies to compute the nonlinear dynamics of a structure. The sections in which the topics are treated are indicated (Sects. 4.3–4.5)

ally, the analytical models of structures (relegated to simple geometries such as straight beams, circular or rectangular plates, cylindrical and spherical shells..., see Sect. 4.3) are discretised by expansions on truncated eigenmode bases (path 5.1 of Fig. 4.8, see Sect. 4.4.2). Owing to the high physical content of eigenmode and their orthogonality properties that uncouple a linear dynamics, it is also possible to expand a finite-element model onto a reduced eigenmode basis (path 4.2 of Fig. 4.8, see Sect. 4.4.2). However, as shown in Chaps. 2 and 3 of this book and in Sects. 4.4 and 4.6, using invariant manifold reduction methods (paths 3, 4.1 and 5.1 of Fig. 4.8) is a powerful, robust and theoretically consistent method to obtain the most accurate reduced order models.

### 4.3 Structures with Geometrical Non-linearities

This section gathers a few models of geometrically nonlinear structures. The main aims are (i) to give an overview of the different form of governing equations encountered with some well known models, (ii) to analyse the effect of symmetries in the geometry of the structures or of their dynamics and (iii) to address the physical mechanisms that create the geometrical nonlinearities.

### 4.3.1 Three-Dimensional Elastic Structures

We consider a continuous elastic medium subjected to large rotations and small strains. From a physical point of view, this means that the deformation of the continuous medium can be described as follows: each of its fibers undergoes a transformation that can be split in (i) a rigid body motion of any amplitude (the angle  $\theta$  in Fig. 4.9 can be arbitrary large) (ii) onto which is superimposed a small deformation, associated to small (local) strains.

In this context, a correct strain measure is the Green-Lagrange strain tensor, defined by:

$$\boldsymbol{\varepsilon} = \frac{1}{2} (\mathbf{F}^T \mathbf{F} - \mathbf{1}) = \frac{1}{2} (\nabla \mathbf{u} + \nabla^T \mathbf{u} + \nabla^T \mathbf{u} \nabla \mathbf{u}), \quad (4.6)$$

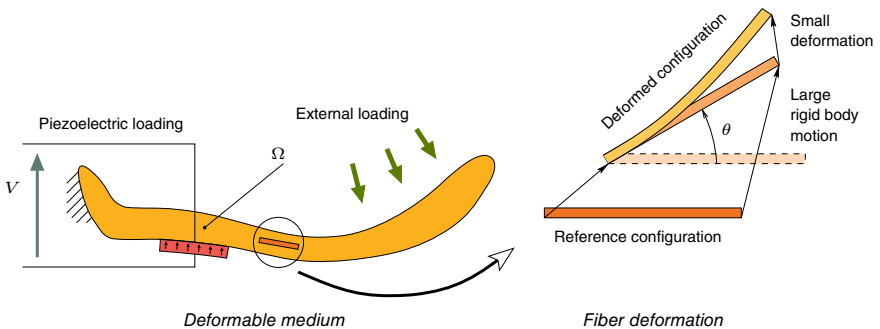
where  $\mathbf{u}$  is the displacement field,  $\mathbf{F} = \mathbf{1} + \nabla \mathbf{u}$  is the deformation gradient,  $\mathbf{1}$  the identity tensor and  $\nabla$ ,  $\nabla^T$  are the tensor gradient and its transpose. The strain tensor  $\boldsymbol{\varepsilon}$  is energetically conjugated to the second Piola-Kirchhoff stress tensor  $\boldsymbol{\sigma}$  and, because the medium is elastic,  $\boldsymbol{\sigma}$  derives from a potential energy density  $\mathcal{W}$  (with unit [J/m<sup>3</sup>]). Moreover, since the local strains are small, it allows to chose a linear constitutive law (sometimes known as a Saint Venant-Kirchhoff model (Holzapfel 2000)). This reads:

$$\boldsymbol{\sigma} = \frac{\partial \mathcal{W}}{\partial \boldsymbol{\varepsilon}} \Rightarrow \boldsymbol{\varepsilon} = \frac{1 + \nu}{Y} \boldsymbol{\sigma} - \frac{\nu}{Y} \text{tr} \boldsymbol{\sigma} \mathbf{1}, \quad (4.7)$$

where  $(Y, \nu)$  are Young's modulus and Poisson's ratio of the material and  $\text{tr}$  the trace operator.

The principle of virtual work states that for all time  $t$  and virtual displacement  $\delta \mathbf{u}$ :

$$- \int_{\Omega} \boldsymbol{\sigma} : \delta \boldsymbol{\varepsilon} \, d\Omega + \int_{\Omega} \mathbf{f}_e \cdot \delta \mathbf{u} \, d\Omega + \int_{\partial\Omega} \mathbf{F}_e \cdot \delta \mathbf{u} \, dS = \int_{\Omega} \rho \ddot{\mathbf{u}} \cdot \delta \mathbf{u} \, d\Omega, \quad (4.8)$$



**Fig. 4.9** Deformation of a deformable medium with large displacement/rotations and small strain

$\Omega$ ,  $\partial\Omega$  being the domain and its boundary, occupied by the initial configuration of the medium. Moreover, “ $\cdot$ ” denotes the doubly contracted product of two tensors and  $\rho$  is the density of the material. Considering the linear elastic constitutive law (4.7),  $\boldsymbol{\sigma}$  is a linear function of  $\boldsymbol{\varepsilon}$  and thus a quadratic function of the displacement field  $\mathbf{u}$ . In addition, taking the first variation of Eq. (4.6) shows that  $\delta\boldsymbol{\varepsilon}$  is linear in  $\mathbf{u}$ . As a consequence, the first term of (4.8) is a polynomial function of  $\mathbf{u}$ , with *quadratic* and *cubic nonlinearities* at most.

Finally, applying any three-dimensional finite-element discretisation method to (4.8) with (4.7) leads to:

$$\mathbf{M}\ddot{\mathbf{x}} + \mathbf{K}\mathbf{x} + \mathbf{f}_{\text{nl}}(\mathbf{x}) = \mathbf{f}_e, \quad (4.9)$$

where  $\mathbf{x} \in \mathbb{R}^N$  gathers all the displacement components of the nodes of the finite-element mesh, with  $N$  the associated number of degrees-of-freedom, and with  $\mathbf{M}$ ,  $\mathbf{K}$  the mass and stiffness matrices, of size  $N \times N$ ,  $\mathbf{f}_e$  the external force vector and  $\mathbf{f}_{\text{nl}}$  the internal nonlinear force vector, of size  $N$ , that can be formally written  $f_{\text{nl}i} = G_{ijk}x_jx_k + H_{ijkl}x_jx_kx_l$  (with Einstein’s notation), that includes *quadratic and cubic only polynomial* terms. This formulation is the one implemented in most nonlinear finite element codes (see e.g. Abaqus (2024), Aster (1989–2024)). However,  $\mathbf{f}_{\text{nl}}$  is never written with quadratic and cubic components ( $G_{ijk}$ ,  $H_{ijkl}$ ) but simply computed upon request for a given  $\mathbf{u}$ .

The above model does not include dissipation, a subject addressed in Sect. 4.4.1. Moreover, for more details about continuum mechanics, refer to Holzapfel (2000), Salençon (2001), Wriggers (2008).

### 4.3.2 Beam Models

A beam is a continuous medium obtained by moving a plane surface  $\mathcal{S}(x)$  (called *cross section*) on a curve  $\mathcal{C}$  (called *middle line*,  $x \in \mathbb{R}$  being an arclength parametrisation) and keeping  $\mathcal{S}(x)$  orthogonal to  $\mathcal{C}$ . This medium is *slender* if the characteristic size  $\phi(x)$  of the cross section remains small with respect to the length  $L$  and the local curvature radius  $R(x)$  of the middle line:

$$\forall x, \quad \phi(x) \ll L, \quad \phi(x) \ll R(x)$$

In practice,  $\phi(x) < L/20$  (and  $R(x) < L/20$ ) are correct upper limits for the beam model described hereafter to be valid at less than 1%.

In a beam structural model, two main assumptions are stated. The first (and fundamental) one is about the motion of the cross sections during deformation. The simplest models prescribe that the *cross sections remain rigid* during deformation, stuck to the middle line which deforms (Assumption 1). Then, the so-called Euler-Bernoulli (or sometimes Kirchhoff) assumptions state that the cross sections remain *orthogonal to the deformed middle line* during deformation, whereas Timoshenko

assumptions, more general, allow a *shear angle* (the angle  $\tilde{\gamma}$  in Fig. 4.10) between the deformed cross section and the plane orthogonal to the middle line.

The second assumption is about the stresses in the cross section. Because of its slender geometry, a beam balances external forces mainly by creating traction/compression stresses in its longitudinal fibers. The stress  $\sigma_{xx}$  is then much larger than the transverse stresses  $\sigma_{yy}$  and  $\sigma_{zz}$ . Then,  $\sigma_{yy}$  and  $\sigma_{zz}$  are neglected in the beam model (Assumption 2).

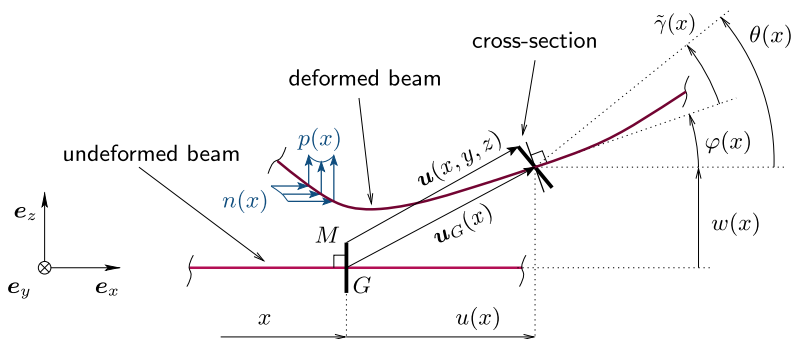
**Geometrically exact model** The geometrically exact beam model is based on the two assumptions introduced above (beam kinematics and transverse stresses neglected). It introduces no truncation on the rigid body rotations of the cross sections, such that it has no limit in term of deformation validity. This model was proposed and used in different scientific communities (physics of solids, computational mechanics, nonlinear dynamics...) receiving different names (Kirchhoff theory, elastica theory, Cosserat theory, geometrically exact theory, Simo-Reissner theory...). The interested reader can refer to Antman (1974), Reissner (1972), Simo and Vu-Quoc (1988), Lacarbonara and Yabuno (2006), Thomas et al. (2016), G eradin and Cardona (2001), Bauchau (2011), Meier et al. (2019) for historical details.

For the sake of simplicity, the derivations reported here are restricted to a straight beam ( $\mathcal{C}$  is straight) with deformations restricted to the plane ( $\mathbf{e}_x, \mathbf{e}_z$ ) (2D or plane deformations). All derivations are taken from Thomas et al. (2016). The interested reader can refer to G eradin and Cardona (2001) for the 3D case and to Linn et al. (2013), Meier et al. (2019) for the case of a curved middle line.

We consider that the geometric center  $G(x)$  of any cross section  $\mathcal{S}(x)$  is a point of the center line  $\mathcal{C}$ . Its position with respect to the center  $O$  of a reference frame is  $\mathbf{OG} = x\mathbf{e}_x$ , such that the position of any point  $M$  of the beam contained in the cross section  $\mathcal{S}(x)$  is  $\mathbf{OM} = x\mathbf{e}_x + y\mathbf{e}_y + z\mathbf{e}_z$  with  $(x, y, z) \in \mathbb{R}^3$  its coordinates.

Assumption 1 is satisfied by writing the displacement field  $\mathbf{u}(x, y, z)$  of any point  $M$  of coordinates of the beam domain as (using the addition of vectors):

$$\mathbf{u} = \mathbf{u}_G + [\mathbf{R}(\theta) - \mathbf{1}] \mathbf{GM}, \quad (4.10)$$



**Fig. 4.10** Beam kinematics. The time dependence of quantities is omitted for simplicity

where  $\mathbf{u}_G(x, t)$  is the displacement vector of the geometric center  $G \in \mathcal{C}$  of the cross section  $\mathcal{S}(x)$ ,  $\mathbf{R}(\theta)$  is a rotation operator,  $\theta(x, t)$  is the rotation of the cross section around vector  $\mathbf{e}_y$  and  $\mathbf{GM} = y\mathbf{e}_e + z\mathbf{e}_e$  is the position vector of point  $M$  in the cross section  $\mathcal{S}(x)$ . Indeed, as shown in Fig. 4.10, the motion of any cross section is the combination of a translation  $\mathbf{u}_G$  and a rotation  $\mathbf{R}$ . With deformations in the plane  $(\mathbf{e}_x, \mathbf{e}_z)$ , the rotation operator is given by:

$$\mathbf{R}(\theta) = \begin{pmatrix} \cos \theta & -\sin \theta \\ \sin \theta & \cos \theta \end{pmatrix}, \quad (4.11)$$

expressed in the frame  $(\mathbf{e}_x, \mathbf{e}_z)$ .

The displacement of any point of the middle line being written  $\mathbf{u}_G = u\mathbf{e}_x + w\mathbf{e}_z$ , with  $(u(x, t), w(x, t))$  the axial and transverse displacement fields, the displacement field  $\mathbf{u} = \mathbf{u}(x, y, t)$  of the continuum (it does not depend on  $y$  because of the motion restriction in  $(\mathbf{e}_x, \mathbf{e}_z)$ ) can be written as:

$$\mathbf{u} = [u - z \sin \theta]\mathbf{e}_x + [w + z(\cos \theta - 1)]\mathbf{e}_z. \quad (4.12)$$

Computing the Green-Lagrange strain tensor with Eq. (4.12) leads to a cumbersome expression because of the nonlinear term in Eq. (4.6). It is possible to simplify it by considering that the local strains are small (see Fig. 4.9). However, to simplify the local strain part in  $\varepsilon$  without affecting the rigid body motion of the cross sections, one cannot attack directly the term  $\nabla^T \mathbf{u} \nabla \mathbf{u}$ . An elegant way to realize this operation is to use the following pseudo-polar decomposition of the deformation gradient:

$$\mathbf{F} = \mathbf{R}(\theta)\mathbf{U} \quad \Rightarrow \quad \mathbf{U} = \mathbf{R}(-\theta)\mathbf{F}, \quad (4.13)$$

where  $\mathbf{U}$  is a stretch tensor, that represents the local strain *free of the rigid body motion* of the cross section. Computing  $\mathbf{F}$  with Eq. (4.12) and using Eq. (4.13), one can show that  $\mathbf{U} = \mathbf{1} + \mathbf{L}$  with

$$\mathbf{L} = \begin{pmatrix} e - z\kappa & 0 \\ \gamma & 0 \end{pmatrix}, \quad \begin{cases} e = (1 + u') \cos \theta + w' \sin \theta - 1, \\ \kappa = \theta', \\ \gamma = -(1 + u') \sin \theta + w' \cos \theta, \end{cases} \quad (4.14)$$

with  $\circ' = \partial \circ / \partial x$ . In the above equations,  $e$  is the axial strain,  $\gamma$  is the shear strain and  $\kappa$  the curvature, directly related to the *local strains* of the beam (refer to Thomas et al. (2016) for more physical insight). Introducing Eq. (4.13) into (4.6) together with the properties of the rotation operator, one shows that:

$$\varepsilon = \frac{1}{2} \left( \mathbf{L} + \mathbf{L}^T + \mathbf{L}^T \mathbf{L} \right) = \begin{pmatrix} e - z\kappa & \gamma/2 \\ \gamma/2 & 0 \end{pmatrix}. \quad (4.15)$$

If the local strains are small,  $(e, \gamma, \kappa)$  are small,  $\mathbf{L}$  is small and the last term in the above equation can be cancelled since it is small with respect to the two others.

This operation is sometimes called in the literature a “consistent linearisation of the strains”, which leads to the final expression of the strain tensor  $\varepsilon$  written above.

Using the constitutive law (4.7) with  $\sigma_{yy} = \sigma_{zz} = 0$  (Assumption 2) leads to (using Eq. (4.14):

$$\sigma_{xx} = Y\varepsilon_{xx} = Y(e - z\kappa), \quad \sigma_{xz} = 2G\varepsilon_{xz} = G\gamma, \quad (4.16)$$

with  $G = Y/[2(1 + \nu)]$  the shear modulus of the material. Then, the stress resultants (axial force, shear force and bending moment) are obtained as:

$$N = \int_S \sigma_{xx} \, dS = YSe, \quad M = \int_S z\sigma_{xx} \, dS = YI\kappa, \quad T = \int_S \sigma_{xz} \, dS = kGS\gamma, \quad (4.17)$$

where there is a decoupling of the axial and bending motions because  $G$  was chosen as the geometric center of  $S(x)$ , where  $(S, I)$  are its area and second moment of area and  $k$  is a shear correction factor.

Finally, taking the first variation of Eq. (4.14) to obtain  $(\delta e, \delta\gamma, \delta\kappa)$  and using the principle of virtual work (4.8) with Eq. (4.16) and the definition (4.17) of  $(N, T, M)$  leads to the strong form of the governing equations of the geometrically exact beam, for all  $(x, t) \in ([0, L], \mathbb{R}^+)$ , with  $L$  the length of the beam:

$$\left\{ \begin{array}{l} \rho S \ddot{u} = (N \cos \theta - T \sin \theta)' + n, \\ \rho S \ddot{w} = (N \sin \theta + T \cos \theta)' + p, \\ \rho I \ddot{\theta} = T(1 + e) - N\gamma + M', \end{array} \right. \quad (4.18a)$$

$$\left. \begin{array}{l} \rho S \ddot{u} = (N \cos \theta - T \sin \theta)' + n, \\ \rho S \ddot{w} = (N \sin \theta + T \cos \theta)' + p, \end{array} \right\} \quad (4.18b)$$

$$\left. \begin{array}{l} \rho S \ddot{u} = (N \cos \theta - T \sin \theta)' + n, \\ \rho I \ddot{\theta} = T(1 + e) - N\gamma + M', \end{array} \right\} \quad (4.18c)$$

where  $(p(x, t), n(x, t))$  are transverse and axial external forces per unit length, along with the natural boundary conditions, at  $x = 0, L$ :

$$N \cos \theta - T \sin \theta = N_e, \quad N \sin \theta + T \cos \theta = T_e, \quad M = M_e, \quad (4.19a, b, c)$$

in which  $(N_e, T_e, M_e)$  are the forces and moments applied at the ends of the beam. The beam constitutive laws read, for all  $(x, t) \in ([0, L], \mathbb{R}^+)$ :

$$\left\{ \begin{array}{l} N = YS [(1 + u') \cos \theta + w' \sin \theta - 1], \\ T = kGS [-(1 + u') \sin \theta + w' \cos \theta], \\ M = EI\theta', \end{array} \right. \quad (4.20a)$$

$$\left. \begin{array}{l} N = YS [(1 + u') \cos \theta + w' \sin \theta - 1], \\ T = kGS [-(1 + u') \sin \theta + w' \cos \theta], \end{array} \right\} \quad (4.20b)$$

$$\left. \begin{array}{l} N = YS [(1 + u') \cos \theta + w' \sin \theta - 1], \\ M = EI\theta', \end{array} \right\} \quad (4.20c)$$

obtained by combining Eqs. (4.17) and (4.14).

A first comment on this model is that the geometrical exactness of the model, which enables, as discussed, to keep the rotation of the cross section exact, introduce *trigonometric nonlinear terms* of the form  $(\sin \theta, \cos \theta)$ , both in the equations of motion (4.18) and in the beam constitutive law. This model has very few exact analytical solutions (we can think if the static buckling of an elastica, Bažant and Cedolin (2010), Audoly and Pomeau (2010)) and may thus be solved numerically. To this purpose, a finite-element discretisation will be addressed at the end of the present Sect. 4.3.2. Other possibilities are to rely on truncated Taylor expansions

of the  $(\sin \theta, \cos \theta)$  nonlinearities to obtain simplified models, at the cost of getting back a validity limit. To this end, two widely used analytical models (the von Kármán model and the inextensible model) are reported hereafter.

**Von Kármán model (straight beam)** This model was initially proposed in Woinowsky-Krieger (1950), Mettler (1951), Eringen (1952) as a first correction to a linear beam model to take into account the nonlinear stretching effect observed in beams with axial ends restrained, a major effect of the geometrical nonlinearities that will be explained later in this section. It is analogous to what was proposed for plate by von Kármán in 1910 (von Kármán 1910), which justifies the name of this model used in this text.

Historically, this model was introduced by correcting an Euler-Bernoulli linear beam model by the fundamental assumption of *keeping in the axial strain the first nonlinear term in  $w$  only*. Consequently, it is based on four assumptions: (i) an Euler-Bernoulli kinematics (each cross section, during deformation, remains orthogonal to the deformed middle line), leading to neglect the shear strain ( $2\varepsilon_{xy} = \gamma = 0$ ), (ii) a linear relationship between the cross section rotation and the transverse displacement  $\theta = w'$ , (iii) a neglected rotatory inertia and (iv) a nonlinear term in  $w$  added in the axial strain  $\varepsilon_{xx}$ . This leads to:

$$e = u' + \frac{1}{2}w'^2, \quad \varepsilon_{xx} = e - z\theta' = e - zw''. \quad (4.21)$$

By considering for simplicity an homogeneous and isotropic material and a uniform cross section, using the same linear elastic constitutive law and stress resultant than in the geometrically exact theory (4.17), the strain expression (4.21) leads with the principle of virtual work (4.8) to the following governing equations for all  $(x, t) \in ([0, L], \mathbb{R}^+)$ :

$$\left\{ \begin{array}{l} \rho S \ddot{u} - N' = n, \\ \rho S \ddot{w} + YI w'''' - \underbrace{(Nw')}' = p, \\ \text{axial/bending coupling} \end{array} \right. \quad (4.22a)$$

$$(4.22b)$$

associated to the natural boundary conditions, at  $x = 0, L$ :

$$N = N_e, \quad Nw' - M' = T_e, \quad M = M_e. \quad (4.23a, b, c)$$

The beam constitutive laws reads:

$$N = YS \left( u' + \underbrace{\frac{1}{2}w'^2} \right), \quad M = YI w''. \quad (4.24a, b)$$

axial/bending coupling

Since with the Euler-Bernoulli assumptions the shear force  $T$  is associated to a zero virtual work, it does not appear naturally and it is identified in the boundary conditions (4.23b) as  $T = -M'$  (see Géradin and Rixen (2015)).

This model can be obtained and justified from the geometrically exact model thanks to a Taylor expansion and truncation to the *second order* in  $\theta$ . Indeed, we first assume:

$$\cos \theta \simeq 1 - \theta^2/2, \quad \sin \theta \simeq \tan \theta \simeq \theta, \quad (4.25)$$

and also that  $u$  is of the order of  $w^2$ , as they appear in those respective orders in the expression of  $e$  in (4.21). This is also justified by practical cases, as shown below. Then, Eq. (4.14) leads to:

$$\gamma = 0 \Rightarrow w'/(1 + u') = \tan \theta \simeq \theta \Rightarrow \theta \simeq w', \quad (4.26)$$

$$e = (1 + u')(1 - \theta^2/2) + w'\theta - 1 \Rightarrow e \simeq u' + w'^2/2, \quad (4.27)$$

whereas Eq. (4.18) are rewritten:

$$\rho I \ddot{\alpha} = T(1 + e) - N\chi + M' \Rightarrow T \simeq -M' = -YI\theta'' \simeq -YIw''', \quad (4.28)$$

$$\rho S \ddot{w} = [N\theta - YI\theta''(1 - \theta^2/2)]' + p \simeq (Nw')' - YIw''''', \quad (4.29)$$

$$\rho S \ddot{u} = [N(1 - \theta^2/2) + YI\theta'''\theta]' + n \simeq N' + n, \quad (4.30)$$

proving Eqs. (4.22–4.24).

This model can also be rigorously justified from 3D elasticity by asymptotic expansion as a function of a small parameter linked to the intensity of the external force (see e.g. Ciarlet (1980), Millet et al. (2001)).

In practice, the present von Kármán model is used for computing the transverse displacement field  $w(x, t)$ , leading often to consider the beam free of distributed axial force ( $n = 0$ ). The axial inertia, linked to the axial vibration motion which appear at high-frequencies, is also neglected. Equation (4.22a) then means that  $N' = 0 \Rightarrow N(x, t) = N(t)$  is uniform over the beam length. Then, integrating Eq. (4.24a) over the beam length leads to:

$$\int_0^L N \, dx = LN \Rightarrow N = \frac{YS}{L} \left( [u]_0^L + \frac{1}{2} \int_0^L w^2 \, dx \right). \quad (4.31)$$

where  $[\circ]$  is the variation of  $\circ$ .



If the beam's ends are immovable,  $u = 0$  at  $x = 0, L$ ,  $[u]_0^L = 0$  such that Eq. (4.31) leads to:

$$N = \underbrace{\frac{YS}{2L} \int_0^L w'^2 dx}_{\text{axial/bending coupling}} \quad (4.32)$$

This equation, along with the transverse equation of motion (4.22b), shows that the von Kármán model captures one major geometrically nonlinear effect encountered in thin structures: the *axial/bending coupling*. Indeed, a transverse deflection  $w$  creates an increase of the beam length, that manifests itself by an axial tension  $N > 0$  in the beam because the beam ends are immovable. Eq. (4.32) shows that this is a second order nonlinear effect since  $N$  is proportional to the square of  $w$ , which is logical since in a linear straight beam model, axial and bending are uncoupled. Then, the axial tension  $N \geq 0$  acts as an increase of bending stiffness because of the term  $(Nw)' = Nw''$  of Eq. (4.22b). This explains that the geometrical non-linearities for a straight beam with immovable ends always create a *hardening* effect, well captured by the von Kármán equation.

Eliminating  $N$  between Eqs. (4.32) and (4.22b) leads to the following equation of motion in  $w(x, t)$ , for all  $(x, t) \in ([0, L], \mathbb{R}^+)$ :

$$\rho S \ddot{w} + YI w'''' - \frac{YS}{2L} w'' \int_0^L w'^2 dx = p. \quad (4.33)$$

Consequently, for a straight beam, the geometrical non-linearities create *cubic* terms only.

The validity range of the von Kármán model, in term of transverse deflection, depends on the value of  $\theta$  since it relies on Eq. (4.25), valid for  $\theta(x) \lesssim 20$  deg. In term of transverse deflection, the validity limit depends on the pattern  $w(x)$  : in vibrations, if we consider the motion on a single mode shape, the higher the mode is, the higher  $\theta(x)$  will be for a given maximum value of  $w(x)$ . However, the validity limit is often given in the literature as  $w(x) \lesssim 3\phi$ , where  $\phi$  is the characteristic dimension of the cross section in the transverse direction (thickness, diameter...). This result is confirmed for the backbone curves of the first mode of a clamped-clamped beam in Debeurre et al. (2023a). However, in static buckling onto the first mode, it is shown in Neukirch et al. (2021) that the validity limit should be given with respect to the length of the beam and is found to be  $w(x) < 0.2L$ , which is much higher. This question deserve clarifications, but keeping a rough value of  $w(x) \lesssim 3\phi$  seems interesting in practice since non-linearities often appear at an order of magnitude lower, of the order, of  $w(x) \simeq \phi^2/L$ , a value often used to obtain scaled equations when using perturbation methods (see Touzé et al. (2002), Thomas et al. (2005)).

Finally, it should be noted that if the beam is free in the axial direction at one of its ends, meaning that  $N_e = 0$  at  $x = L$  for instance, Eqs. (4.23a) and (4.22a) prove that  $N = 0$  for all  $x \in [0, L]$ . As a consequence, the transverse equation of motion (4.22b) becomes  $\rho S \ddot{w} + YI w'''' = p$ , which is linear, meaning that *in the case of unrestrained axial ends, the von Kármán model is linear and does not include*

*geometrical nonlinearities*. These non-linearities appear at a higher order in  $\theta$ , that is captured by the inextensible model addressed hereafter. If the ends of the beam are not perfectly immovable, such in the case of a finite axial stiffness in the boundary conditions, the validity of the von Kármán model decreases with the stiffness of the boundary condition, requiring higher order models (or even a geometrically exact model), see Lacarbonara and Yabuno (2006). This is also the case for rotating beams under the effect of centrifugal force (Thomas et al. 2016).

**Von Kármán model (beam with initial curvature)** If the beam is not straight (it is sometimes called an arch), the above derivations must be modified according to the local curvature and twist of the beam when computing the displacement field (4.12), the deformation gradient and the strains (4.14) (see Linn et al. (2013)). However, those effects can be accounted for using Eqs. (4.32) and (4.22b) for a beam initially curved in the plane ( $\mathbf{e}_x, \mathbf{e}_z$ ). Indeed, we replace in those equations  $w(x, t)$  by  $w_0(x) + w(x, t)$  where  $w_0(x)$  is the initial profile of the beam and the “new”  $w(x, t)$  is the transverse displacement with respect to the initially curved configuration. One obtains:

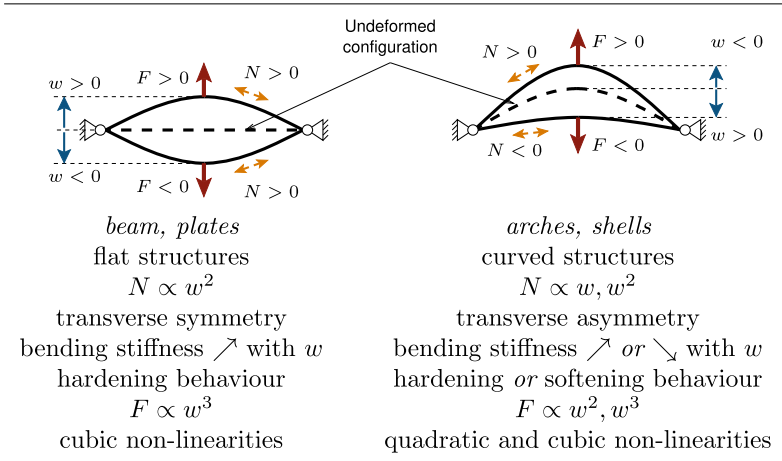
$$\rho S \ddot{w} + YS(w_0'''' + w'''' ) - N(w_0'' + w'') = p, \quad N = \frac{YS}{2L} \int_0^L (w_0'^2 + 2w_0'w' + w'^2) dx, \quad (4.34a, b)$$

Then, we enforce that the initial configuration is stress free, meaning that the above equation is verified if  $w \equiv 0$ , leading to cancel some terms (see above equation), to finally obtain:

$$\rho S \ddot{w} + YI w'''' - \frac{YS}{2L} \left[ \underbrace{2w_0'' \int_0^L w_0' w' dx}_{\text{linear}} + \underbrace{\left( 2w'' \int_0^L w_0' w' dx + w_0'' \int_0^L w'^2 dx \right)}_{\text{quadratic}} + \underbrace{w'' \int_0^L w'^2 dx}_{\text{cubic}} \right] = p. \quad (4.35)$$

This model is valid for moderate value of  $w_0(x)$  (see the discussion about the validity of the von Kármán model in the previous section) but has the advantage of highlighting the effect of curvature on the vibrations. In Eq. (4.35), the first line corresponds to the linear part of the model, with the second term that brings corrections due to the non straight initial configuration (compare to Eq. (4.33)). Then, the second line shows the effect of the geometrical nonlinearities. The cubic (last) term is unchanged with respect to an initially straight configuration, but one observes the important result that the initial curvature of the structure brings *quadratic* nonlinearities.

Physically, the appearance of quadratic and cubic non-linearities in the equations can be linked to the transverse symmetry of the structure, as summarised in Fig. 4.11. For a flat structure, the transverse behaviour is symmetric: if a given  $F$  creates  $w(x)$ ,



**Fig. 4.11** Transverse symmetry, hardening and softening behaviour

$-F$  gives  $-w(x)$ , i.e. the same pattern with opposite sign. From a structural point of view, an external force  $F$  always creates a positive axial force  $N$  (consider the term  $w^2$  in Eq. (4.32)) since the length of the beam always increases, whatever be the sign of  $w$ . As a result, the bending stiffness always increases, the behaviour is always hardening and only cubic terms  $w^3$  are present in the equations since they preserve the symmetry (if  $F$  is changed in  $-F$ ,  $w^3$  is changed in  $-w^3$ ).

The presence of an initial curvature breaks this transverse symmetry. For a positive curvature,  $F > 0$  brings tension ( $N > 0$ ) whereas  $F < 0$  brings compression ( $-N < 0$ , see the term  $w'_0 w'$  in Eq. (4.34b)) because it increases/decreases the length of the beam. As a result, the bending stiffness is modulated during an oscillation, giving rise to hardening or softening behaviour, depending on the vibration pattern and the amplitude of the oscillations. This qualitatively explains the hardening/softening behaviour of the shell in Fig. 4.6 and also the one of the arch considered in Marconi et al. (2021), Vizzaccaro et al. (2022). Naturally, this brings symmetry breaking quadratic nonlinearities, since changing the sign of  $w$  changes the absolute value of  $\alpha w + \beta w^2$ ,  $\alpha, \beta \in \mathbb{R}$ .

**Inextensible model** Another interesting and widely used analytical model is the so-called inextensible model, initially proposed in Crespo da Silva and Glynn (1978a, b). It is able to capture rotations larger than achieved by the von Kármán model, extends it to the case of loose axial boundary conditions, including the cantilever beam case. It consists in (i) assuming an Euler-Bernoulli kinematics and neglecting the rotatory inertia, (ii) using an inextensibility constraint (we assume that the curvilinear length of the beam does not change during deformation) to condense the axial motion  $u(x, t)$  into the transverse equation of motion, (iii) expanding and truncating the

geometrically exact model to *third order* in  $\theta$  and (iv) assuming cantilever boundary conditions.

Assumptions (i) and (ii) lead to  $(\gamma, e) = (0, 0)$  and

$$(1 + u')^2 + w'^2 = 1, \quad \cos \theta = 1 + u', \quad \sin \theta = w'. \quad (4.36a, b, c)$$

These relations can be obtained geometrically (see Thomas et al. (2016)) or here by solving Eq. (4.14) for  $\cos \theta$  and  $\theta$  with and  $(\gamma, e) = (0, 0)$  and using  $\cos^2 \theta + \sin^2 \theta = 1$ . Then, Eq. (4.18c) gives  $T = -M' = -YI\theta''$  and, eliminating  $N$  in Eq. (4.18b) using (4.18a) and assumption (iv) ( $N(L, t) = T(N, t) = 0 \forall t$ ), the following partial integro-differential equation is obtained:

$$\rho S \ddot{w} + \left( \frac{YI\theta''}{\cos \theta} \right)' - \left[ \tan \theta \int_L^x (\rho S \ddot{u} - n) dx \right]' = p. \quad (4.37)$$

Finally, setting  $n = 0$  (no distributed axial load), eliminating  $u$  using (4.36a) and performing a careful Taylor expansion up to order three in  $w$  leads to the following governing equation for  $w(x, t)$ , for all  $(x, t) \in ([0, L], \mathbb{R}^+)$ :

$$\rho S \ddot{w} + YI w'''' + YI \underbrace{(w' w'^2 + w''' w'^2)'}_{\text{curvature NL}} + \underbrace{\frac{\rho S}{2} \left[ w' \int_L^x \frac{\partial^2}{\partial t^2} \left( \int_0^x w'^2 dx \right) dx \right]'}_{\text{inertia NL}} = p. \quad (4.38)$$

More details are provided in Thomas et al. (2016), Debeurre et al. (2023b).

In this model, the geometrical nonlinearities create two groups of terms: (i) *inertia non-linearities*, which come from the condensation of the axial inertia  $\rho S \ddot{u}$  into the transverse equation of motion and (ii) some *curvature non-linearities*, stemming from the fact that the curvature  $\kappa$ , responsible for the bending stiffness ( $M = YI\kappa$ , Eq. (4.17c)) is a nonlinear function of  $w$ . It is interesting to notice that it is possible to write this model as a function of  $\theta(x, t)$  (see Farokhi et al. (2022)). In this case, there are only *inertia non-linearities* because the curvature  $\kappa = \theta'$  (Eq. (4.14b)) is a linear function of  $\theta$ .

**Finite-element discretisation** In practice, it is interesting to have at our disposal solutions to the geometrically exact model, necessarily fully numerical, that are not limited in amplitude range like the two analytical models addressed above. Several numerical solving strategies exist in the literature, most of them being related to time integration (see e.g. Gerstmayr et al. (2008), Lang et al. (2011), Sonnevile et al. (2014)). Since we are interested here in vibrations, especially around resonances, frequency domain techniques are interesting since they directly tackle the periodic steady state, including nonlinear mode computations (see Sects. 4.4, 4.5).

The first step in this case is to discretize the geometrically exact model in space. In the planar deformation case considered above (Eqs. (4.18–4.20)), among other solution, simple Timoshenko beam elements can be used, leading to obtained the following set of equations, for all  $t \geq 0$ :

$$\mathbf{M}\ddot{\mathbf{x}} + \mathbf{f}(\mathbf{x}) = \mathbf{f}_e, \quad (4.39)$$

with  $\mathbf{M}$  the mass matrix, of size  $N \times N$  with  $N$  the number of degrees-of-freedom of the model,  $\mathbf{f}(\mathbf{x})$  the internal force vector,  $\mathbf{f}_e$  the external force vector, both of size  $N$ , and  $\mathbf{x}(t)$ , that collects the displacement and rotation ( $u_i, w_i, \theta_i$ ),  $i \in \{1, \dots, N_n\}$  of all the nodes of the finite-element mesh (of  $N_n$  nodes, such that  $N = 3N_n$ ). In this case,  $\mathbf{f}(\mathbf{x})$  includes *trigonometric non-linearities* (see Thomas et al. (2016), Debeurre et al. (2023a) for details).

It is possible to transform the nonlinearities in  $\mathbf{f}(\mathbf{x})$  into polynomials in an exact way by parametrizing the rotation operator  $\mathbf{R}$  with quaternions (in the planar case, this leads to replace  $\theta$  by ( $q_0 = \cos(\theta/2)$ ,  $q_2 = \sin(\theta/2)$ )), with the counterpart of adding an additional unity constraint. This transforms (4.39) into a DAEs (differential algebraic equations) and adds Lagrange multipliers in the unknown  $\mathbf{x}(t)$  (see Debeurre et al. (2024b), Grolet et al. (2024)). This approach is also possible for the full three-dimensional (3D) deformation case (see Lazarus et al. (2013), Cottanceau et al. (2017), Debeurre et al. (2024b)). It must be noticed that in this 3D case, the parametrisation of the rotation operator  $\mathbf{R}$  is less straightforward, necessarily brings constraints to avoid singularities and that other solutions than quaternions are available (see G eradin and Cardona (2001), Bauchau (2011), Bagheri et al. (2024)).

### 4.3.3 Plate and Shell Models

Plates (flat) and shells (with curvature) are the extensions to a two-dimensional (2D) medium of the beam model addressed in Sect. 4.3.2. A shell is a continuous medium obtained by moving a line segment on a 2D surface  $\Sigma$ . It is thin if the length  $h(\mathbf{x})$  of the segment remains small with respect to the characteristic dimensions of  $\Sigma$  ( $\mathbf{x}$  is the position vector of any point of  $\Sigma$ ).

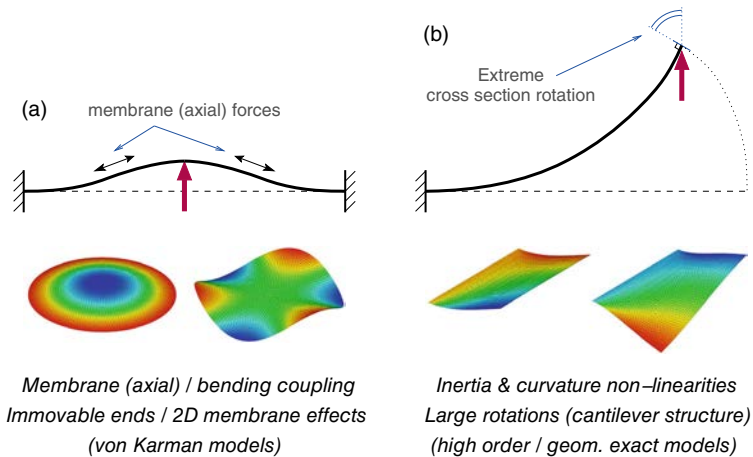
The classical plate and shell models are based on the fundamental *kinematical* assumption analogous to that of the beam models: each segment is subjected to a rigid body motion during deformation, stuck to the middle surface that deforms. Then, the Kirchhoff-Love enforces the segments to remain orthogonal to the deformed middle surface and Reissner-Mindlin assumptions allow transverse shear, in an analogous manner than the Euler-Bernoulli and Timoshenko assumptions for beams. The transverse stress  $\sigma_{zz}$  (if  $(\mathbf{e}_x, \mathbf{e}_y)$  is the plane tangent to the middle surface) is also neglected in the theory (see Chapelle and Bathe (2011)).

The issues related to geometrical non-linearities in those models bare the same general principles to what appears for beam models. Geometrically exact models exist for shells (see Simo and Fox (1989), Simo et al. (1990), Bauchau and Sonnevile (2021)), as well as von K arm an models (the fundamental von K arm an assumption (4.21) for simplifying the Green-Lagrange strains was first proposed for plates in von K arm an (1910)). However, there is *one main fundamental difference*, related to the intrinsic 2D structure of plates and shells.

For beams, von Kármán models, that account for the nonlinear axial/coupling phenomenon, as seen in Sect. 4.3.2, are valid only if the axial motion of the beam is restrained by the boundary conditions. On the contrary, in the case of plates (and shells), the coupling between the bending motion and the stresses in the middle surface (called *membrane stresses or forces*) can appear even for completely free boundary conditions, because it is linked to a *change of the metrics* of the middle surface. This *purely 2D effect* appear if the deformed shape of the structure does not create a *developable deformation* (see Audoly and Pomeau (2010)).

An example is the nonlinear vibration of free edge circular plates or spherical shells (see Thomas et al. (2003, 2007)) or the gong example in Sect. 4.2.4 (Fig. 4.6). If we consider for instance the first axisymmetric mode, a small elementary square element of the middle plane will be deformed into a trapezoid, creating in-plane stresses, whereas it will remain a square in the case of the first mode of a cantilever plate, free of in-plane stresses (see Fig. 4.12 for the two mode shapes). Due to this property, a large amount of practical applications of geometrically nonlinear plates and shells can be accurately modeled by von Kármán models (see Amabili (2008)). In the case of shells, depending on the type of curved geometry, the analytical models based on von Kármán strain-displacement relationship such as (4.21) take several names, depending on the seminal works that initiated them: Donnell, Mushtari, Vlasov, Koiter, Novozhilov... and large rotation (geometrically exact) are less necessary.

In this text, only analytical von Kármán models are quickly reported, essentially to understand that they are very similar to the beam models of Sect. 4.3.2. From Thomas and Bilbao (2008), we consider a plate of middle plane surface  $\Sigma$  and constant thickness  $h$ , and we denote by  $w(x, t)$  the displacement of any point  $\mathbf{x}$  of  $\Sigma$ . Neglecting in-plane inertia and external forces, it is possible to exactly characterize the in-plane stresses (which are the three independent components of a tensor) by a



**Fig. 4.12** The two main mechanisms of geometrical nonlinearities in slender structures

scalar Airy stress function  $F(\mathbf{x}, t)$ . The equation of motion can be written  $\forall(\mathbf{x}, t) \in (\Sigma, \mathbb{R}^+)$ :

$$\begin{cases} D\Delta\Delta w + \rho h \ddot{w} = L(w, F) + p, & (4.40a) \\ \Delta\Delta F = -\frac{Yh}{2}L(w, w), & (4.40b) \end{cases}$$

where  $\Delta$  is the 2D Laplacian,  $D = Yh^3/[12(1 - \nu^2)]$  is the bending stiffness of the plate and the  $L(\circ, \diamond)$  is the Monge-Ampère operator (see Thomas and Bilbao (2008), Audoly and Pomeau (2010)), defined by:

$$L(\circ, \diamond) = \Delta \circ \Delta \diamond - \nabla \nabla \circ : \nabla \nabla \diamond, \quad (4.41)$$

its main property being that it is *bilinear*.

In the same spirit as for curved beams, it is possible to obtain a shallow shell equation with (4.40) by replacing  $w(\mathbf{x}, t)$  by  $w_0(\mathbf{x}) + w(\mathbf{x}, t)$ , with  $w_0$  defining an initial non-plane geometry and the “new”  $w$  being the displacement with respect to the initially curved configuration, and also by enforcing a stress-free initial condition. From Camier et al. (2009), one obtains:

$$\begin{cases} D\Delta\Delta w + \rho h \ddot{w} = L(w_0, F) + L(w, F) + p, & (4.42a) \\ \Delta\Delta F = -\frac{Yh}{2}[2L(w_0, w) + L(w, w)]. & (4.42b) \end{cases}$$

All conclusions and comments raised for the beam models in Sect. 4.3.2 can also be analogously formulated for the present plate and shell models. The geometrically *membrane/bending* coupling appears here in the equations with (i) the terms  $L(w, w)$  in Eqs. (4.40b) and (4.42b), creating membrane forces  $F$  proportional to the square of the transverse displacement  $w$ , and (ii) with the term  $L(w, F)$  in Eqs. (4.40a) and (4.42a) which brings cubic non-linearities in  $w$ . Then, the initial curvatures brings a linear and quadratic terms in the equations thanks to  $L(w_0, w)$  and  $L(w_0, F)$  in Eq. (4.42b, a). The main difference in comparison to beams is that the 2D structures of the plates & shells leads to non uniform membrane forces ( $F$  depends on  $\mathbf{x}$  whereas  $N$  was uniform for straight beams, see Eq. (4.32) and related comments). As a consequence,  $F(\mathbf{x}, t)$  cannot be eliminated to obtain a single cubic partial differential equation (PDE) in  $w(\mathbf{x}, t)$ .

### 4.3.4 Piezoelectric Structures

In this section, we shortly address the inclusion of piezoelectric material coupling into the elastic geometrically nonlinear models addressed in the previous sections, with reference to Givois et al. (2021). Piezoelectric materials are able to transform a part of their strain energy into electrostatic energy and inversely (it is a reversible

thermodynamic process) and are widely used in marine sonars, M/NEMS, electronic clocks, vibration control and health monitoring...

The electromechanical coupling appears in the constitutive law of the material. In this text, we consider only a linear coupling, even if material non-linearities are often observed (see Chap. 3 of this book for MEMS applications as well as examples in Leadnham and Erturk (2015), Givois et al. (2020a) for macro-structure cases). Considering only a conservative coupling, the constitutive law (4.7) still derives from a potential energy (called here a Gibbs electrical free energy), but now depends on two new energetically conjugated electrical state variables: the electric field vector  $\mathbf{E}$  and the electric displacement vector  $\mathbf{D}$ , linked to the electrical polarisation of the medium (see Johnk (1988), Maugin (1988), Ikeda (1990)). This constitutive law, that replaces Eq. (4.7), can be written as follows, with Einstein's notation:

$$\begin{cases} \sigma_{ij} = c_{ijkl}^E \varepsilon_{kl} - e_{kij} E_k, \\ D_i = e_{ikl} \varepsilon_{kl} + \epsilon_{ik}^E E_k, \end{cases} \quad (4.43)$$

where  $c^E$  is the rank 4 stiffness tensor (at constant electric field),  $e$  is the rank 3 piezoelectric coupling tensor and  $\epsilon^E$  is the rank 2 dielectric tensor (at constant strain). In the particular case of a purely elastic and isotropic media,  $e = \mathbf{0}$  and one recovers Eq. (4.7) with  $c^E$  solely function of  $(Y, \nu)$ .

When writing the equations of motion of a piezoelectric media, it is convenient to define the electric potential  $\psi$  as:

$$\nabla \psi = -\mathbf{E}, \quad (4.44)$$

and to use it as an unknown field that replaces  $\mathbf{E}$ , such that the principle of virtual work (4.8) becomes, for all time and virtual displacement and potential  $(\delta \mathbf{u}, \delta \psi)$ :

$$\int_{\Omega} \rho \ddot{\mathbf{u}} \cdot \delta \mathbf{u} \, d\Omega + \int_{\Omega} (\boldsymbol{\sigma} : \delta \boldsymbol{\varepsilon} + \mathbf{D} \cdot \delta \mathbf{E}) \, d\Omega = \int_{\Omega} \mathbf{f}_e \cdot \delta \mathbf{u} \, d\Omega + \int_{\partial\Omega} (\mathbf{F}_e \cdot \delta \mathbf{u} + q_e \delta \psi) \, dS, \quad (4.45)$$

with  $q_e$  an external electric surface charge density.

In practice, piezoelectric materials are often introduced in a system as thin layers, onto which two other layers of conducting material are added, all being called a *piezoelectric patch*. The latter create electrodes, whose purpose is, when connected to an electric circuit, to collect the electric charges created by the piezoelectric material and to couple the mechanical deformation to the electrical circuit. These electrodes create equipotential surfaces (surfaces onto which  $\psi$  is uniform). As a consequence, the coupling with the electrical circuit is conveniently written using *global variables*, i.e. discrete variables associated to a given domain, that replace the usual *local (fields) ones* ( $\psi, \mathbf{D}$ ). These global variables are the electric potential difference  $V(t)$  (the voltage) between the electrodes and the global electric charge  $Q(t)$  (the integral of  $q_e$  onto the surface of the electrodes). In a numerical model, the equipotentiality can be enforced with Lagrange multipliers. However, since no external electric charge are applied inside the piezoelectric domain, it is possible to perform an exact



condensation of the internal electric degrees-of-freedom such that  $(V, Q)$  becomes the only electrical unknowns of the problem (see Givois et al. (2021) for details).

After applying any three-dimensional finite-element discretisation method to (4.45) with (4.43), one obtains, for all  $t \geq 0$ :

$$\begin{cases} \mathbf{M}\ddot{\mathbf{x}} + \mathbf{K}\mathbf{x} + \mathbf{f}_{\text{nl}}(\mathbf{x}) + (\mathbf{f}_c + \mathbf{P}_c\mathbf{x})V = \mathbf{f}_e, & (4.46a) \\ CV - (\mathbf{f}_c + \frac{1}{2}\mathbf{P}_c\mathbf{x})^T \mathbf{x} = Q, & (4.46b) \end{cases}$$

In the above equations, a single piezoelectric patch is considered, of electrical unknowns  $(V(t), Q(t))$ , which is coupled to the displacement of the nodes of the finite-element mesh collected in vector  $\mathbf{x}(t)$ , of size  $N$ . The first equation is associated to the mechanical behaviour of the system, which may be used for *actuator* applications (one prescribes  $V(t)$  to create mechanical deformations), whereas the second one refers to the electrical behaviour and may be used for *sensor* application, for which the electric state  $(Q, V)$  is created by the mechanical deformations in  $\mathbf{x}$ . For certain vibration control applications, both equations are coupled to an electrical circuit and need to be considered at the same time (see Ducarne et al. (2012)).

As in the case of a purely elastic structure (see Eq. (4.9)), mechanical mass  $\mathbf{M}$  and stiffness  $\mathbf{K}$  matrices appear, and, more interestingly, the geometrical non-linearities have an identical effect, separated from the piezoelectric coupling, in the vector  $\mathbf{f}_{\text{nl}}(\mathbf{x})$ , of size  $N$ , which includes the same quadratic and cubic terms. The piezoelectric coupling appear first with a constant vector  $\mathbf{f}_c$ , of size  $N$ , which, multiplied with the voltage  $V(t) \in \mathbb{R}$ , creates a forcing vector analogous to the mechanical forcing  $\mathbf{f}_e(t)$ . This term is the classical one that appears in the case of the modeling of a linear piezoelectric structure (see Thomas et al. (2009)). In the second (electrical) Eq. (4.46b),  $C$  is the electric capacitance of the piezoelectric patch.

Finally, the joint effect of geometrical non-linearities and piezoelectric coupling create a particular term with the constant symmetric matrix  $\mathbf{P}_c$ , of size  $N \times N$ , which as the sense of a *parametric* driving term since  $\mathbf{P}_c V(t)$  multiplies  $\mathbf{x}(t)$ , analogous to what appears in the parametric driven pendulum Eq. (4.4). This effect will be physically addressed in Sect. 4.6.5.

Whereas the same linear piezoelectric coupling  $\mathbf{f}_c$  appear in both Eq. (4.46) because of the reversibility of the piezoelectric process, the nonlinear (parametric) coupling appear with a factor  $1/2$  in the electric equation.

### 4.3.5 Scaling of the Equations

An important point, left aside in the present text when writing the models for the sake of conciseness, is the scaling of the equations, which has two major benefits. First, it provides the list of the independent parameters of a given model. Second, it enables to scale the equations such that the relative order of magnitude of the term can be evaluated, for perturbation developments for instance (see e.g. Nayfeh and Mook (1979)).

In the case of the geometrically exact model (Eqs. (4.18–4.20)), one can keep in mind that if  $w$  is scaled by the length  $L$  of the beam and with an Euler-Bernoulli kinematics, the model depends on only one free (dimensionless) parameter: the *slenderness parameter*  $\eta = I/(SL^2) = r^2/L^2$ , where  $r = \sqrt{I/S}$  [m] is the radius of gyration, a measure of the characteristic diameter of the beam’s cross section<sup>2</sup> (see Neukirch et al. (2021)). As a consequence, plotting results in term of  $w/L$  gives master results (see Neukirch et al. (2021) for examples). In the case of a Timoshenko kinematics, a second (shear) dimensionless parameter  $\mu = Y\eta/(kG)$  comes into play (see Debeurre et al. (2023a)).

On the contrary, scaling  $w$  by the radius of gyration  $r$  leads to a von Kármán model (4.33) independent of any parameter, irrespective of the cross section geometry, thus giving results with the largest scope (see Givois et al. (2019)). The same result apply for the plate model (4.40) if  $w$  is scaled by  $h/\sqrt{12(1-\nu^2)}$  (see Givois et al. (2019)), and for the inextensible model (4.37) if  $w$  is scaled by  $L$  (see Thomas et al. (2016)).

### 4.3.6 Synthesis

As a short summary about the beam/plate/shell models, two fundamental issues have to be kept in mind. The first one is that there are two fundamental mechanisms of geometrical non-linearities in those thin structures, sketched in Fig. 4.12: the *membrane (axial)/bending coupling* and the effect of *large rotations*, which brings *inertia non-linearities*. These two mechanisms guide the analyst in the choice of the right model (in particular, a von Kármán model should be avoided in the case of large rotations since it is linear and, inversely, if the axial motion is restrained in a way, a von Kármán model is sufficient).

The second question is about the *transverse symmetry* of the structure, summarised in Fig. 4.11: a transversely symmetric structures (a homogeneous beam/plate or a composite beam/plate with a symmetric lamination) structures is only subjected to *hardening behaviour* and the symmetry is preserved in the equations of motion (cubic nonlinearities in the transverse displacement  $w$  only). If the symmetry is broken because of curvature or/and a non-symmetric lamination, then a *softening behaviour* can occur and the equations of motion include quadratic non-linearities in  $w$ .

Finally, all those effects are taken into account in the 3D models of Sect. 4.3.1 that are the most general ones since no assumptions about the kinematics of the cross sections and the transverse stresses are formulated. However, considering the thin structures beam/plate/shell models, in addition to give very accurate solutions, it enables to get an interesting insight in the mechanisms of deformation into play and probably guide the analyst in understanding some “blind” complex 3D finite-element simulations.

---

<sup>2</sup>  $r = h/\sqrt{12}$  for a rectangular cross section of thickness  $h$  and  $r = \phi/4$  for a circular cross section of diameter  $\phi$ .

About piezoelectric coupling, it is interesting to note that all effects appear as *separated terms* in the equations (see Eq. (4.46a, b)): the elastic geometric nonlinearities on one side, the linear piezoelectric coupling on the other side and the joint effect of piezoelectric coupling and geometrical non-linearities. It is also interesting to note that this latter effect is responsible for a *parametric driving* term.

## 4.4 Nonlinear Modes and Model Reduction

As introduced in Sect. 4.2.5, several strategies exist to compute the response of a nonlinear system. When the geometry of the system is not simple, one may rely on a finite-element discretisation of the problem, which leads to EDOs (or DAEs in the case of geometrically exact model discretisation), as shown in Sect. 4.3 (see Eqs. (4.9), (4.39) and (4.46)). The size  $N$  of those sets can be huge (several thousand or million degrees-of-freedom) in realistic practical applications, at first to reach a suitable convergence of the finite-element mesh, but also because of the complex geometries often encountered in engineering applications (see examples in Chaps. 3 and 5 of the present book and also in Fig. 4.26). In this situation, direct (brute) simulations are time consuming, sometime out of reach, especially if several iterative computations are needed, in a design process for instance. This justifies the idea of model reduction, i.e. replacing the initial model by another one of a much smaller size, that is able to capture the awaited behaviour with a minimal and controlled error.

As we address in this text the computation of a dynamical system in vibrations, the main class of phenomena to capture are linked to *the resonance* of this system. In the case of a linear system, the standard reduction method is to expand the dynamics on an eigenmode basis, which transforms the initial EDOs into an uncoupled set of linear oscillators, which enables and justifies a truncation, by keeping only a few modes, basically those which have their natural frequency in the spectrum of the excitation. This reduced order model can be refined by adding static modes (Balmès 1996).

If such an expansion is applied to a nonlinear system, the eigenmodes being in this case those of the associated linearised model, the obtained oscillators become coupled by nonlinear terms, which are the mathematical source of the nonlinear phenomena described in Sect. 4.2.4. In this situation, the question of the truncation of the expansion basis is not straightforward, justifying more powerful reduction techniques.

Even if several reduction methods exist, we will focus here on the concept of *non-linear modes* and *invariant manifolds*, since they give a clear mathematical framework to efficiently reduce and compute *quantitatively* the dynamics in the case of resonant systems. Moreover, it will be seen that they also provide a powerful mean of giving *qualitative* insights into the understanding of the dynamics and in particular the phenomena enumerated in Sect. 4.2.4.

### 4.4.1 The Question of Damping

In all the models in Sect. 4.3, no damping was introduced. In contrast to inertia, elasticity or gravity forces, damping forces are delicate because the associated modelling process is much less straightforward. The reason is that the physical sources of damping in mechanical systems are multiple: internal thermoelastic or viscoelastic dissipation inside the material (Chaigne and Lambourg 2001), aeroelastic drag due to an interaction with the surrounding fluid during vibration (Colin et al. 2020; Debeurre et al. 2024a; Gallerand et al. 2024), anchor losses in M/NEMS (Chouvion et al. 2012), dry friction in the joints between several solid members (see Chap. 5 in this book), acoustical radiation (Gottlieb 1975)...

In practice, the simplest damping model is a linear viscous one. In a finite-element context, one adds a term  $C\dot{X}$  in the equations of the model (in Eqs. (4.9), (4.39) or (4.46a)), with  $C$  a constant damping matrix of size  $N \times N$ . In most commercial finite-element codes, a Rayleigh damping model is the standard choice, for which the damping matrix is mass and stiffness proportional:  $C = \alpha M + \beta K$ , with  $(\alpha, \beta) \in \mathbb{R}^2$  two coefficients. This model has no clear physical foundation and can be viewed as the easiest mathematical and numerical way of including damping in simulations. Moreover, considering that the damping ratio of the  $k$ -th mode reads  $\xi_k = (\alpha/\omega_k + \beta\omega_k)/2$  (with  $\omega_k$  the natural frequency, see e.g. G eradin and Rixen (2015)), the stiffness proportional part (of coefficient  $\beta$ ) can be very unrealistic since it leads to necessarily *overdamped* modes ( $\xi_k \simeq \beta\omega_k/2 > 1$  for a high value of  $\omega_k$ ) in the higher part of the spectrum.

In the case of viscoelastic elastomeric or rubber materials, used as vibration isolator or for vibration damping, the accurate simulation of their vibratory behaviour is usually done in the frequency domain since it enables taking into account experimentally identified material laws linked to a complex and frequency dependent Young's modulus ( $C \ni Y^* = Y'(\omega) + iY''(\omega)$ , where  $(Y', Y'') \in \mathbb{R}^2$  are the so-called storage and loss moduli, see Rouleau et al. (2017)). This linear damping model, coupled to geometrical nonlinearities, can have a nonlinear damping effect (see Debeurre et al. (2024a) and reference therein).

Another common way of including damping is to rely on a modal viscous damping model, for which modal damping coefficients are adjusted separately for each eigenmode. This is a way of obtaining very accurate simulations since the damping model can be easily adjusted, either with a general frequency dependent law or by experimental identification (see Ducceschi and Touz e (2015)).

All those models being linear, some intrinsically nonlinear damping sources can also arise, such as dry friction damping (see e.g. Vakilinejad et al. (2020)), aeroelastic drag (see Colin et al. (2020), Debeurre et al. (2024a)), piezoelectric damping (Leadenham and Erturk 2015)...

## 4.4.2 Linear Mode Expansion

As a preliminary, this section addresses eigenmode expansions, for three reasons. Firstly, this is the standard method for discretizing the nonlinear analytical models, like those reported in Sect. 4.3. Secondly, modal expansions enable to characterize, interpret and help understand mathematically the effect of the non-linearities, by observing the non-linear terms that appear in the modal oscillators. Finally, they can constitute a powerful way of computing the dynamics when a good accuracy on the values of the natural frequencies and on the damping model is required (see Ducceschi and Touzé 2015).

**Basics of linear modes** The eigenmodes (or natural or normal modes) of a linear system are fundamental solutions under free vibrations. For the reasons explained in Sect. 4.4.1, the question of having an accurate damping model is not simple and the standard practice in structural mechanics simulations is to use the eigenmodes of the *undamped* system. The eigenmodes of the undamped and linear system will be denoted here by *Conservative Linear Modes* (CLM).

It is also possible to define the modes of the *damped system*, in the case of a linear viscous damping model ( $C\dot{X}$ ), by switching to the state space (see Géradin and Rixen (2015)). Those modes, called here *Damped Linear Modes* (DLM), are theoretically interesting since they uncouple the damped linear system, include damping factors in the eigenvalues and have complex (in  $\mathbb{C}$ ) mode shapes associated to non synchronous motions. In practice, they are used as the basic model for experimental modal analysis. However, there are seldom used in computational dynamics since one has to specify the damping matrix  $C$ , unknown in most practical cases. Moreover, if the damping is light, it can be seen (see Géradin and Rixen (2015)) that, at first order, the CLMs diagonalize the *damped* system, such that DLMs are useless.

**Conservative Linear Modes** We start by linearizing the analytical and numerical models of Sect. 4.3, that can be put under the following general form in free vibrations, either PDEs (continuous in space) or ODEs (discretised in space):

$$\begin{cases} \mathcal{M}(\ddot{w}) + \mathcal{K}(w) = 0 \\ \mathcal{B}_i(w) = 0, \quad i = 1, \dots, K \end{cases}, \quad M\ddot{\mathbf{x}} + \mathbf{K}\mathbf{x} = \mathbf{0}, \quad (4.47a, b)$$

where  $(\mathcal{M}, \mathcal{K}, \mathcal{B}_i)$  are differential operators and  $K$  is the order of the stiffness operator  $\mathcal{K}$  (see Meirovitch (1967) for more details about this formalism). Their definition is straightforward: in the case of the beam model of Eq. (4.33), one has  $\mathcal{M}(\diamond) = \rho S \diamond$  and  $\mathcal{K}(\diamond) = Y I \diamond''''$ ; in the case of the plate model of Eq. (4.40), one has  $\mathcal{M}(\diamond) = \rho h \diamond$  and  $\mathcal{K}(\diamond) = D \Delta \Delta \diamond$ . In both cases,  $K = 4$  boundary conditions  $\mathcal{B}_i = 0$  are required.

Then, looking for solutions uncoupled in time and space such as  $w(x, t) = \Phi(x)q(t)$  and  $\mathbf{x}(t) = \mathbf{\Phi}q(t)$ , assuming that  $\mathbf{K}$  and  $\mathcal{K}$  are positive (i.e. the equilibrium point  $(w, \mathbf{x}) \equiv (0, \mathbf{0})$  is stable, or at least indifferent), the problems (4.4.2) leads to the following solution:

$$\ddot{q} + \omega^2 q = 0, \quad \begin{cases} \mathcal{K}(\Phi) - \omega^2 \mathcal{M}(\Phi) = 0 \\ \mathcal{B}_i(\Phi) = 0, \quad i = 1, \dots, K \end{cases}, \quad (\mathbf{K} - \omega^2 \mathbf{M}) \Phi = \mathbf{0}. \quad (4.48a, b, c)$$

The first equation above shows that  $q(t)$  oscillates at frequency  $\omega$ . Then, the two last equations are the *eigenvalue problems* that defines the CLMs  $(\omega_k, \Phi_k(x))$  and  $(\omega_k, \Phi_k)$  of the problems,  $k \in \mathbb{N}^*$ . For the analytical models,  $k$  may be theoretically infinite, whereas for the discretised model,  $k \in 1, \dots, N$ .

The families of mode shapes (or eigenvectors)  $\{\Phi_k(x)\}_{k \in \mathbb{N}^*}$  or  $\{\Phi_k\}_{k=1, \dots, N}$  constitute bases of the space of solutions which are orthogonal to the mass and stiffness operators, such that:

$$\begin{cases} \int_{\Omega} \Phi_i \mathcal{M}(\Phi_j) \, d\Omega = m_i \delta_{ij} \\ \int_{\Omega} \Phi_i \mathcal{K}(\Phi_j) \, d\Omega = \omega_j^2 m_i \delta_{ij} \end{cases}, \quad \begin{cases} \Phi_i \mathbf{M} \Phi_j = m_i \delta_{ij} \\ \Phi_i \mathbf{K} \Phi_j = m_i \omega_j^2 \delta_{ij} \end{cases}, \quad (4.49)$$

where  $\delta_{ij}$  is the Kronecker delta,  $m_i$  the modal mass of the  $i$ th CLM and  $\Omega$  is the domain of the middle line/surface of the structure under concern.

We look for a solution of the models of Sect. 4.3 in the form of the modal expansions:

$$w(x, t) = \sum_{k=1}^M \Phi_k(x) q_k(t), \quad \mathbf{x}(t) = \sum_{k=1}^M \Phi_k q_k(t), \quad (4.50a, b)$$

where the  $\{q_k\}_{k=1, \dots, M}$  are the modal coordinates and  $M$  is the number of eigenvectors kept in the expansion basis. Injecting the above solution in the equation of motion, multiplying by a mode shape  $\Phi_j(x)$  or  $\Phi_j^T$  and using the orthogonality properties (4.49) leads to modal equations that will be analysed in the following.

**Analytical models for uncurved structures** For didactic reasons, some details on the modal expansion process are first given on the straight von Kármán beam model (4.33). The CLMs  $(\omega_k, \Phi_k(x))$  are solutions of (4.4.2b), that reads in the present beam case:

$$YI \Phi'''' - \rho S \omega^2 \Phi = 0. \quad (4.51)$$

It possesses analytical solutions for simple boundary conditions (Gérardin and Rixen 2015).

Injecting Eqs. (4.50) into (4.32) leads to:

$$N(t) = \frac{YS}{2L} \sum_{i=1}^M \sum_{j=1}^M E_{ij} q_i(t) q_j(t), \quad E_{ij} = \int_0^L \Phi_i' \Phi_j' \, dx. \quad (4.52a, b)$$

Then, injecting (4.50) and the above equation in the equation of motion (4.22b), multiplying both members by  $\Phi_j(x)$ , integrating the result from  $x = 0$  to  $x = L$  and using (4.49) leads to,  $\forall k = 1, \dots, M$ :

$$\ddot{q}_k + 2\xi_k \omega_k \dot{q}_k + \omega_k^2 q_k + \sum_{i=1}^M \sum_{j=1}^M \sum_{l=1}^M \gamma_{ijl}^k q_i q_j q_l = F_k, \quad (4.53)$$

with

$$\gamma_{ijl}^k = -\frac{Y}{2\rho L} \frac{\int_0^L \Phi_i' \Phi_j' dx \int_0^L \Phi_l'' \Phi_k dx}{\int_0^L \Phi_i^2 dx}, \quad F_k(t) = \frac{\int_0^L \Phi_k(x) p(x, t) dx}{\rho S \int_0^L \Phi_i^2 dx}. \quad (4.54a, b)$$

The above coefficients are computed in practice by numerical integrations, depending on the analytical expressions for the mode shapes  $\Phi_k(x)$  and the external forcing  $p(x, t)$ . Note also that modal viscous damping terms, of modal ratio  $\xi_k$ , have been heuristically added.

Coefficients  $\gamma_{ijl}^k$  in Eq. (4.54a) take a simplified form in the case of simple boundary conditions, since the second integral in the numerator can be written  $\int_0^L \Phi_l'' \Phi_k dx = -\int_0^L \Phi_l' \Phi_k' dx + [\Phi_l' \Phi_k]_0^L$ . With any combination of clamped, hinged or guided boundary conditions, the second term  $[\Phi_l' \Phi_k]_0^L$  is zero and one simply obtains:

$$\gamma_{ijl}^k = \frac{Y}{2\rho L} \frac{E_{ij} E_{kl}}{\int_0^L \Phi_i^2 dx}, \quad (4.55)$$

with  $E_{ij} = E_{ji}$ , defined by Eq. (4.52b) and directly related to the deformed shapes of the natural modes.

For the plate model (Eq. (4.40)), with a similar algebra, the same modal model (4.54) is obtained, with the value of the cubic coefficient that also depend on membrane mode shapes (see Thomas and Bilbao (2008)).

Finally, since those structures are flat, only cubic nonlinear terms are obtained (see Fig. 4.11). They can be positive or negative depending on the four mode shapes ( $\Phi_i, \Phi_j, \Phi_l, \Phi_k$ ) involved in  $\gamma_{ijl}^k$  and their scaling. However, coefficient  $\gamma_{kkk}^k$  is always positive (it is proportional to  $E_{kk}^2$ , see Eq. (4.55)), such that the associated nonlinear behaviour is always hardening (see Sect. 4.4.5).

**Analytical models for curved structures** In the case of the models for curved structures, it is often convenient to choose the modes of the associated *uncurved structure* as an expansion basis, since those of the *curved structure* are often not known analytically. Proceeding to the same computation than for the straight beam with Eq. (4.35), one obtains,  $\forall k = 1, \dots, M$ :

$$\ddot{q}_k + 2\xi_k \omega_k \dot{q}_k + \omega_k^2 q_k + \sum_{i=1}^M \alpha_i^k q_i + \sum_{i,j=1}^M \beta_{ij}^k q_i q_j + \sum_{i,j=1}^M \gamma_{ijl}^k q_i q_j q_l = F_k, \quad (4.56)$$

where the quadratic terms arise from the initial curvature of the structure. The linear coupling appear because the expansion basis (the one of the uncurved structure) is

not the one of the eigenmodes of the curved structure, which would diagonalised the linear part of the dynamics ( $\alpha_i^k$  would vanish in this case).

If the initial profile  $w_0$  of the structure is expanded onto the same modal basis:

$$w_0(x) = \sum_{k=1}^{M_0} a_k \Phi_k(x), \quad \text{with} \quad a_k = \frac{1}{m_k} \int_0^L \mathcal{M}(w_0(x)) \Phi_k(x) dx, \quad (4.57)$$

(the second expressions comes from the mode orthogonality), nice expressions are obtained for  $\alpha_i^k$  and  $\beta_{ij}^k$ , that depend only on coefficients  $\gamma_{ijl}^k$ :

$$\alpha_i^k = \sum_{j,l=1}^{M_0} \gamma_{ijl}^k a_j a_l, \quad \beta_{ij}^k = \sum_{l=1}^{M_0} (\gamma_{ijl}^k + 2\gamma_{lji}^k) a_l. \quad (4.58)$$

This method is interesting in particular to study the effect of imperfections on the nonlinear response of a structure. It was used for plates and shells in Camier et al. (2009), Amabili (2008) and was extended more recently for arbitrary structures discretised in a finite-element context (Marconi et al. 2021).

**Inextensible model** Applying the same procedure to Eq. (4.38) leads to the following modal model,  $\forall k = 1, \dots, M$ :

$$\ddot{q}_k + 2\xi_k \omega_k \dot{q}_k + \omega_k^2 q_k + \sum_{i,j,l=1}^M \left[ \gamma_{ijl}^k q_i q_j q_l + \pi_{ijl}^k (\ddot{q}_j q_l + \dot{q}_j \dot{q}_l) q_i \right] = F_k, \quad (4.59)$$

where the coefficients  $\gamma_{ijl}^k$  and  $\pi_{ijl}^k$  are also functions of the mode shapes  $\Phi_k$ , see Thomas et al. (2016), Colin et al. (2020) for details, and can be computed by numerical integration.

**Finite-element discretisations** We first consider the 3D finite-element discretisations of a purely elastic medium. Introducing the modal expansion (4.50b) into (4.9), multiplying by  $\Phi_j^T$  and using the orthogonality properties (4.49) leads to,  $\forall k = 1, \dots, M$ :

$$\ddot{q}_k + 2\xi_k \omega_k \dot{q}_k + \omega_k^2 q_k + \sum_{i,j=1}^M \beta_{ij}^k q_i q_j + \sum_{i,j=1}^M \gamma_{ijl}^k q_i q_j q_l = F_k, \quad (4.60)$$

with  $F_k(t) = \Phi_k^T f_e(t)$ . Since the basis used for the expansion is the eigenmode basis of the associated linear problem, the linear part is diagonal and quadratic and cubic nonlinearities are obtained.

In contrast to the analytical models addressed above, the computation of the nonlinear coefficients  $\beta_{ij}^k$  and  $\gamma_{ijl}^k$  is less straightforward. Indeed, standard finite-element codes have built-in procedures to compute the eigenmode basis  $\{(\omega_k, \Phi_k)\}$ ,



but expanding the internal force vector  $\mathbf{f}_{\text{nl}}(\mathbf{x})$  onto them is not standard. However, it is possible to perform this operation non-intrusively (i.e. with numerical procedures already implemented in finite-element codes), following the so-called STiffness Evaluation Procedure (STEP), a very clever method first introduced in Muravyov and Rizzi (2003).

The STEP consists in computing  $\mathbf{f}_{\text{nl}}(\mathbf{x})$  for prescribed  $\mathbf{x}$  chosen as combination of mode shapes. As an example, if  $\mathbf{x} = \pm a \Phi_k$ , the orthogonality of the modes shows that necessarily  $q_k = \pm a$  and  $q_j = 0, \forall j \neq k$ . Introducing those equations into the nonlinear part of (4.60) leads to:

$$a^2 \beta_{kk}^k + a^3 \gamma_{kkk}^k = \Phi_k^T \mathbf{f}_{\text{nl}}(a \Phi_k), \quad (4.61a)$$

$$a^2 \beta_{kk}^k - a^3 \gamma_{kkk}^k = \Phi_k^T \mathbf{f}_{\text{nl}}(-a \Phi_k), \quad (4.61b)$$

where the second member is obtained considering the nonlinear part of Eq. (4.9) ( $F_k = \Phi_k^T \mathbf{f}_e = \Phi_k^T \mathbf{f}_{\text{nl}}(\mathbf{x})$ ). As a consequence, the nonlinear coefficients are the solutions of *linear systems* where the second member can be easily computed with any finite-element code that include geometrical non-linearities computations. In practice, the value of  $a$  must be adjusted by hand such that  $a \Phi_k$  correspond to a displacement in the validity domain of the model (see Givois et al. (2019)), with no difficulty in practice. The other coefficients can be obtained by more complex modal combinations such as  $\pm a \Phi_i + \pm b \Phi_j$  etc.

Following the same procedure, the 3D finite element discretisations of a piezoelectric structure of Eq. (4.46) leads to (see Givois et al. (2021)):

$$\left\{ \begin{array}{l} \ddot{q}_k + 2\xi_k \omega_k \dot{q}_k + \omega_k^2 X_k + \sum_{i,j=1}^M \beta_{ij}^k q_i q_j + \sum_{i,j,l=1}^M \gamma_{ijl}^k q_i q_j q_l \\ \quad + \sum_{i=1}^M \theta_{ik} V q_i = F_k - \chi_k V, \end{array} \right. \quad (4.62a)$$

$$\left\{ \begin{array}{l} CV - \sum_{k=1}^M \chi_k q_k - \sum_{i,j=1}^M \frac{1}{2} \theta_{ij} q_i q_j = Q, \end{array} \right. \quad (4.62b)$$

in which the modes must be normalised such that  $m_k = 1$  for all  $k$ , with no loss of generality (otherwise the piezoelectric coefficients  $\chi_k$  and  $\theta_{ij}$  are different by  $m_k$  in the two equations). As already analysed in Sect. 4.3.4, the piezoelectric effect creates a linear coupling, which appear here with the so-called linear piezoelectric coefficient  $\chi_k = \Phi_k^T \mathbf{f}_e$ , and with a nonlinear coupling of coefficient  $\theta_{ij} = \Phi_i^T \mathbf{P}_c \Phi_j$  that creates a parametric driving in Eq. (4.62a). The piezoelectric coefficients  $\chi_k$  and  $\theta_{ij}$  can be also computed non-intrusively in a finite-element code with piezoelectric capabilities with an extension of the STEP (see Givois et al. (2021)).

**Geometrically exact model** Finally, applying the same procedure to the discretised geometrically exact model (4.39) is not as simple. Indeed, the internal force vector  $\mathbf{f}(\mathbf{x})$  includes non-polynomial sin and cos nonlinearities that stops separating space and time, such that closed form modal models are not possible. This technique has however been successfully applied in Farokhi et al. (2022) to the analytical geometrically exact inextensible model of Eq. (4.37) by rewriting the equation in term of the single unknown  $\theta(x, t)$  in place of  $w(x, t)$ . It is used for a modal expansion onto the first six bending modes, which is sufficient to compute the first resonance of the system up to extreme amplitudes of vibrations.

**Synthesis** As a synthesis, the modal models of this section (Eqs. (4.53), (4.56), (4.59), (4.60)) show that the nonlinearities couple the modal coordinates  $q_k(t)$ . One can imagine to truncate those modal models to a few modes, i.e. with  $M$  small, in the same manner than for a fully linear model. This question will be considered in Sect. 4.6, and the next sections introduce the nonlinear mode concept, giving rigorous answers to this question.

### 4.4.3 Definition of Nonlinear Modes

The question of nonlinear modes is thoroughly addressed in Chap. 2 of this book, to which the interested reader may refer for rigorous definitions and reference list. This section may be read as a complement, as it considers only a few emerging issues, selected from the viewpoint of the practical use of the nonlinear modes as (i) *an analysis tool* to qualitatively understand the nonlinear dynamics and (ii) *a model reduction tool* to quantitatively and efficiently computing it.

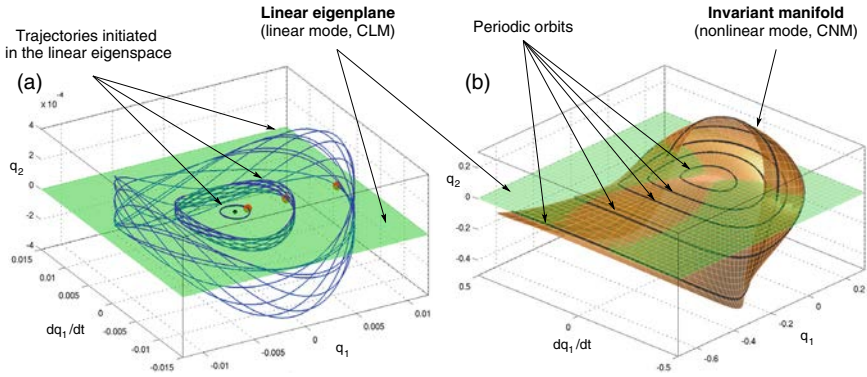
Due to the increase of complexity brought by non-linearities and the associated variety of particular phenomena (see Sect. 4.2.4) as compared to linear systems, and also because it is impossible to strictly extend the orthogonality property of the linear modes to the nonlinear range, several definitions of nonlinear modes exist and this section provides an overview of them. In this text, we simply use the terminology “nonlinear mode” in place of “nonlinear normal modes” (NNM),<sup>3</sup> for the sake of conciseness.

**Two families of definitions** The basic idea beyond nonlinear modes is to extend the eigenmode concept, well defined for linear systems, to the nonlinear range. It is first convenient to consider the basic framework of linear modes: they are the fundamental solutions of a system *in free vibrations*, the easiest case being the *conservative* one. Consequently, we first consider the solution of:

$$M\ddot{\mathbf{x}} + \mathbf{f}(\mathbf{x}) = \mathbf{0}. \tag{4.63}$$

---

<sup>3</sup> The terminology “normal” means “fundamental” in the seminal work of Rosenberg (1962) and must not be understood as “orthogonal”, which would not be appropriate for a nonlinear mode.



**Fig. 4.13** Picture of a CNM in the phase space. **a** illustration of the non invariance of the linear eigenplanes **b** periodic orbits and associated invariant manifold (computed by continuation on the two degrees-of-freedom system of Lamarque et al. (2012))

If one first expands the linearised dynamics of the above system (i.e. with  $f(\mathbf{x}) = \mathbf{K}\mathbf{x}$ ) onto a family of eigenmodes (the CLMs in this case), thanks to their orthogonality properties, a collection of *independent* oscillators are obtained, of the form  $\ddot{q}_k + \omega_k^2 q_k = 0$ ,  $\forall k$ , whose natural solution is *sinusoidal* for each modal coordinate  $q_k(t)$ . In looking for nonlinear modes, although the orthogonality property of the CLMs cannot be extended to the nonlinear range, two other interesting features can, leading to *two families* of definitions.

- Because of non-linearities, the natural solutions of a nonlinear systems are often *periodic* and not purely sinusoidal. It leads to the first idea of defining a nonlinear mode as a *family of periodic solutions of the undamped and unforced system* (4.63) (Fig. 4.13b). This definition, initially proposed in Rosenberg (1962) and taken up by many authors since (see, among others Vakakis et al. (1996), Kerschen et al. (2009)), is naturally adapted to continuation methods (see Sect. 4.5) that enable to numerically compute the CNMs *without limitation in amplitude*. One has can also compute the stability of the CNM and possible bifurcations.
- Secondly, because of the orthogonality of the modes, the modes are *invariant*. It means that if initial conditions are chosen on one particular mode, then the motion remains concentrated on this mode:

$$\mathbf{x}(0) = a\Phi_k, \quad \dot{\mathbf{x}}(0) = b\dot{\Phi}_k \quad \Rightarrow \quad \mathbf{x}(t) = \Phi_k q_k(t) \quad \forall t > 0,$$

meaning  $q_j(t) = 0$ ,  $\forall t > 0 \forall j \neq k$  ( $a, b \in \mathbb{R}$  are two constants). In the phase space, all trajectories obtained for different values of the initial amplitude ( $a, b$ ) maps to a plane (called an eigenplane), which is said invariant since each trajectory initiated in this plane remains in this plane. With non-linearities, the eigenplanes are no more invariant (Fig. 4.13a), but it is possible to find other surfaces that are (Fig. 4.13b). Consequently, the second idea is to define a nonlinear mode as an

*invariant manifold of the phase space*, as initially proposed in Shaw and Pierre (1991). This is a powerful concept since the invariance is the key property for *model order reduction*. A (weak) limitation is that most available computation techniques are asymptotic and are limited in range of amplitude from the equilibrium solution, even if the range can be large thanks to the arbitrary order of the recent numerical solvers (see examples in Chaps. 2 and 3 of this book, and in Grolet et al. (2024)).

The reader may refer to the second chapter of this book for a thorough history and list of references on those concepts, not proposed here for the sake of brevity.

**Conservative nonlinear modes (CNM)** In the case of a conservative system, the two definitions are *equivalent* since any motion initiated on a periodic orbit remains in this periodic orbit and thus lies in an invariant manifold of the phase space. A *Conservative Nonlinear Mode* (CNM) is thus equivalently an invariant manifold of the phase space or a family of periodic orbits solutions of Eq. (4.63).

More theoretically, the existence of the CNMs is proven by a theorem due to Lyapunov (Lyapunov 1907), which states that, with no internal resonance, there exist  $N$  two-dimensional CNMs in the phase space that emerge from the equilibrium point and are tangent to the  $N$  eigenplanes at this point. They are sometimes called Lyapunov Subcenter Manifolds (LSM) since their union is the center manifold (Kelley 1967; de la Llave and Kogelbauer 2019). An illustration of a CNM is given in Fig. 4.13, that shows the non-invariance of a CLM and the geometry of a CNM in the phase space, along with periodic solutions.

**Dissipative nonlinear modes (DNM)** The case of a *dissipative system* is less straightforward since several non-equivalent definitions of a nonlinear mode (called here dissipative nonlinear modes (DNM)) coexist. The invariant manifold definition is still valid, brings no large difficulties with respect to the conservative case, is mathematically the most rigorous and leads efficiently to model order reduction (see Chap. 2 of this book). On the contrary, extending the periodic solutions concept to the dissipative case, mainly to keep the numerical ease of computation brought by continuation methods, is less simple. To follow this later idea, two other definitions deserves to be mentioned. A first idea, proposed in Laxalde and Thouverez (2009), is to define a DNM as a family of pseudo-periodic motions, obtained with a Fourier-Galerkin expansion of the dynamics. Another idea, proposed in Krack (2015), is to keep the family of periodic solutions concept by adding a fictitious negative linear damping term in the equation of motion, leading to use standard continuation numerical codes. This last concept has also the advantage to be adapted to computing non-smooth dissipative non-linearities such as dry friction.

**Phase resonance nonlinear mode (PRNM)** In parallel to the above CNM and DNM definitions, a recent idea is to define a nonlinear mode as a Phase Resonance Nonlinear Mode (PRNM), which is a family of periodic solution of the harmonically forced system when a particular phase shift between the response and the forcing is

enforced, as proposed in Volvert and Kerschen (2021). This concept is interesting since phase resonance is the foundation of particular experimental continuation techniques (see Denis et al. (2018)) and enables to naturally compute fundamental solutions of a nonlinear system in the vicinity of a primary resonance (Debeurre et al. 2024a), but also for secondary resonances (Volvert and Kerschen 2022; Porter and Brake 2024). However, this definition can appear incomplete since the obtained PRNM is not unique as it depends on the chosen forcing (its space dependence and its frequency content) and also because it can be shown that with a suitable choice of the periodic forcing (enabling force appropriation), a PRNM coincide with a CNM, *irrespective of the damping of the system*. Further discussions on this subject are postponed to Sect. 4.5.

**Model reduction of a forced system** As a non autonomous system can be transformed into an autonomous one, it is possible to compute invariant manifolds in the case of a forced system, that enable to reduce the dynamics around a given resonance, being primary, secondary or parametric (see Chap. 2 of the present book).

**Synthesis** Table 4.2 gives a summary of the discussions about nonlinear modes proposed here and in the second chapter of the present book.

Analyzing the several definitions of nonlinear modes given above, the CNMs appear very interesting in many aspects. First, the equivalence between periodic orbits and invariant manifold enables a larger scope of application and computation methods. Secondly, in most practical applications for which a structure resonates, the damping is light, such that the CNMs give fundamental solutions of excellent quality to characterize the damped system, as for linear systems. Finally, experimental testing

**Table 4.2** Overview of definitions for linear and nonlinear modes. For nonlinear systems, the two columns refer to the two families of definitions: invariant manifolds, suitable for model order reduction (MOR), or families of periodic orbits, leading to continuation methods

	<i>Linear system</i>	<i>Nonlinear system</i>	
		Family 1 “MOR”	Family 2 “computation”
Free oscil. conservative	<b>CLM</b> $(\mathbf{K} - \omega^2 \mathbf{M}) \Phi = \mathbf{0}$ 2nd order ODE eigensolutions	<b>CNM</b> $\mathbf{M} \ddot{\mathbf{x}} + \mathbf{f}(\mathbf{x}) = \mathbf{0}$ Invariant manifold $\Leftrightarrow$ Family of periodic solutions	
Free oscil. dissipative	<b>DLM</b> $(\mathbf{A} - \lambda \mathbf{B}) \Psi = \mathbf{0}$ 1st order ODE eigensolutions	<b>DNM</b> $\mathbf{M} \ddot{\mathbf{x}} + \mathbf{f}_d(\dot{\mathbf{x}}) + \mathbf{f}(\mathbf{x}) = \mathbf{0}$ Invariant manifold $\not\Leftrightarrow$ Several definitions	
Forced oscil. dissipative	$(\mathbf{K} - \omega^2 \mathbf{M} + i\omega \mathbf{C}) \hat{\mathbf{x}}(\omega) = \hat{\mathbf{F}}$ FRF	$\mathbf{M} \ddot{\mathbf{x}} + \mathbf{f}_d(\dot{\mathbf{x}}) + \mathbf{f}(\mathbf{x}) = \mathbf{F} \cos \omega t$ Invariant manifold      Continuation of periodic solutions	

techniques such as phase locked loop continuation enable to directly target the CNM of a given system, whatever be its damping (see Sect. 4.5).

However, DNMs have the advantage to naturally include the effect of the damping and thus to study the possible non-linear effects of the damping due to its coupling with the conservative non-linearities. It was reported in some examples that a strong linear modal (or Rayleigh) damping can have a nonlinear effect on the amplitude of a resonance (Touzé and Amabili 2006; Vizzaccaro et al. 2021b) or even change its trend of non-linearity (hardening or softening, see Touzé and Amabili (2006)), both effects well captured by a DNM.

#### 4.4.4 Normal Form for CNM Computation and Model Reduction

While Sect. 4.4.3 is devoted to defining nonlinear modes, we address here a particular way, the so-called oscillatory normal form (ONF), of computing CNMs and using them for model reduction. The underlying idea is still to provide tools to qualitatively analyze and quantitatively compute, if possible, the nonlinear dynamics.

**Resonant terms** As a preliminary, this section covers basics of resonant terms and internal resonances. As a didactic example, let us consider the following set of two free undamped quadratic oscillators:

$$\begin{cases} \ddot{q}_1 + \omega_1^2 q_1 = \beta_1 q_1^2 + \beta_2 q_2^2 + \underline{\beta_3 q_1 q_2}, & (4.64a) \\ \ddot{q}_2 + \omega_2^2 q_2 = \underline{\beta_4 q_1^2} + \beta_5 q_2^2 + \beta_6 q_1 q_2, & (4.64b) \end{cases}$$

with  $\{\beta_k\} \in \mathbb{R}$ ,  $k = 1, \dots, 6$  coefficients and  $(q_1(t), q_2(t))$  two time functions. This can be obtained after reduction of the discretised modal model of a curved structure (such as (4.56) after diagonalisation of the linear part or (4.60)). The oscillations of this system, at first order (i.e. if  $(q_1, q_2)$  are small), are such that:

$$q_1(t) \propto \cos \omega_1 t, \quad q_2(t) \propto \cos \omega_2 t. \quad (4.65)$$

Consequently, the nonlinear terms verify:

$$\begin{aligned} q_1^2 &\propto \frac{1}{2} (1 + \underbrace{\cos 2\omega_1 t}_{\simeq \omega_2}), & q_2^2 &\propto \frac{1}{2} (1 + \cos 2\omega_2 t), \\ q_1 q_2 &\propto \frac{1}{2} (\cos[\omega_1 + \omega_2]t + \underbrace{\cos[\omega_1 - \omega_2]t}_{\simeq \omega_1}). \end{aligned}$$

**Table 4.3** Quadratic and cubic internal resonances: frequency relations and associated terminology

Order 2 (quadratic)			Order 3 (cubic)		
1:2	↔	$\omega_2 \simeq 2\omega_1$	1:1	↔	$\omega_2 \simeq \omega_1$
1:1+1	↔	$\omega_3 \simeq \omega_1 + \omega_2$	1:3	↔	$\omega_2 \simeq 3\omega_1$
			1:1+2	↔	$\omega_3 \simeq \omega_1 + 2\omega_2$
			1:1+1+1	↔	$\omega_4 \simeq \omega_1 + \omega_2 + \omega_3$

Then, if a second order internal resonance condition such as  $\omega_2 \simeq 2\omega_1$  is fulfilled, the terms  $q_1^2$  and  $q_1q_2$  contain an harmonic that oscillates with frequencies  $\omega_1$  and  $\omega_2$ , respectively, such that they can be viewed as terms that *drive the two oscillators at their respective resonances*. Consequently, the two underlined terms in Eq. (4.64) are called *resonant*, whereas the others are *non-resonant*, since they provide excitation far from the resonances. The qualification of a given nonlinear term to be resonant or non-resonant is thus linked to a particular internal resonance relationship. We will also see that the resonant terms constitute the *skeleton of the dynamics* as they are responsible for *strong energy transfers* between modes (see Sects. 4.6.3 and 4.6.4).

**Internal resonances** Internal resonance relationships are commensurable relations between a set of  $N$  frequencies linked to a particular order  $o$  of the associated resonant monomials. Order 2 and 3 internal resonances are reported in Table 4.3 with the associated terminology that specifies the integer multiples of the frequencies involved. For an arbitrary order  $o$ , they can be put under the following form:

$$\omega_j \simeq \sum_{k=1}^N (m_k + m_{k+N})\omega_k, \quad m_k \in \mathbb{Z}, \quad \sum_{k=1}^{2N} |m_k| = o, \quad (4.66)$$

This is a direct consequence of the product of sine and cosine functions, seen as a product of exponentials  $\exp(\pm i\omega_k)$  (see also an analogous formula that involves the  $2N$  eigenvalues  $\{\pm i\omega_k\}_{k=1,\dots,N}$  of the 1st order dynamical system associated to the linear part of (4.63) in Chap. 2 of this book).

Some particular monomials are called *trivially resonant* since they are always resonant, even if no internal resonance relationship are at hand. An example is the nonlinear term  $\Gamma X^3$  in the following Duffing oscillator:

$$\ddot{X} + \omega_0^2 X + \Gamma X^3 = 0. \quad (4.67)$$

This term, at first order, oscillates with two harmonics, at  $\omega_0$  and  $3\omega_0$ , the first one leading to a resonant excitation of the oscillator. The trivially resonant terms are always of odd polynomial order, thus of order 3 at least.

**Normal form** In this section, we apply the normal form method to the modal models of Sect. 4.4.2, and especially Eq. (4.60). The underlining idea is to *find a change of variables (a priori nonlinear) that transforms this system into to a “simpler” one* (with less nonlinear terms, even linear). The change of variables is chosen under a polynomial form, such that it is constructed order by order, at the same time as the new “simpler” dynamical system, called the *normal form*, which is also polynomial and that includes as few as nonlinear monomials as possible. In particular, it will be seen that all invariant breaking monomials are eliminated, such that at the end, the normal form is naturally composed of a collection of *invariant* oscillators, with a direct connection to nonlinear modes.

The first step is to rewrite (4.60) into a first order dynamical system, by adding velocity unknowns  $v_k, \forall k = 1, \dots, M$ :

$$\dot{q}_k = v_k, \quad \dot{v}_k = -\omega_k^2 q_k - \sum_{i,j=1}^M \beta_{ij}^k q_i q_j - \sum_{i,j=1}^M \gamma_{ijl}^k q_i q_j q_l. \quad (4.68)$$

Then, the change of variables (called *normal transform*) is written formally,  $\forall k, i \in \{1, \dots, M\}$ :

$$\begin{cases} q_k = r_k + \mathcal{P}_k^{(o)}(r_i, s_i) \\ v_k = s_k + \mathcal{Q}_k^{(o)}(r_i, s_i) \end{cases}, \quad (4.69)$$

where  $(\mathcal{P}_k^{(o)}, \mathcal{Q}_k^{(o)})$  are polynomials of order  $o \geq 2$  in the new so called *normal coordinates*  $(r_i(t), s_i(t))$ . Formally introducing the normal transform (4.69) into the initial dynamical system (4.68) leads to a new dynamical system in the  $(r_i, s_i)$  variables that can be written as follows,  $\forall k, i \in \{1, \dots, M\}$ :

$$\begin{cases} \dot{r}_k = s_k \\ \dot{s}_k = -\omega_k^2 r_k - \mathcal{R}_k^{(p)}(r_i, s_i) \end{cases} \Rightarrow \ddot{r}_k + \omega_k^2 r_k + \mathcal{R}_k^{(p)}(r_i, s_i) = 0, \quad (4.70)$$

where  $\mathcal{R}_k^{(p)}$  is a polynomial of order  $p \geq 2$ . Then, as shown in Touzé et al. (2004a), and also thanks to Poincaré and Poincaré-Dulac’s theorems (Poincaré 1982; Dulac 1912), the core of the method is to choose the coefficients of the monomials in  $(\mathcal{P}_k^{(o)}, \mathcal{Q}_k^{(o)})$  such that they *cancel as much monomials as possible* in  $\mathcal{R}_k^{(p)}$ . This is achieved sequentially, order by order, as detailed in Touzé (2003). All monomials can be cancelled except those which are resonant since they are related to small denominators in the normal transform that would make it singular.

**The case of no internal resonance** If no internal resonance is present, the  $k$ th oscillator of the normal form (4.70), in the case of an order  $p = 3$ , reads,  $\forall k$ :

$$\ddot{r}_k + \omega_k^2 r_k + (A_{kkk}^k + \gamma_{kkk}^k) r_k^3 + B_{kkk}^k r_k \dot{r}_k^2 + r_k \tilde{\mathcal{P}}_k^{(2)}(r_j, \dot{r}_j) + \dot{r}_k \tilde{\mathcal{Q}}_k^{(2)}(r_j, \dot{r}_j) = 0, \quad (4.71)$$



with  $j \neq k$  and where  $(\tilde{\mathcal{P}}_k^{(2)}, \tilde{\mathcal{Q}}_k^{(2)})$  are polynomials of order 2 and  $(A_{kkk}^k, B_{kkk}^k) \in \mathbb{R}$  depend on the quadratic coefficients  $\beta_{ij}^k$  and the natural frequencies  $\omega_k$  (refer to Touzé et al. (2004a) for their analytical expressions).

The first result is that the normal transform (4.69) is able to cancel all *non-resonant* terms that were present in the initial system, such that the nonlinear part of the normal form (4.70) contains, in the present case where no internal resonance is considered, only trivially resonant nonlinear terms. Since no quadratic trivially resonant term exist, all quadratic term of coefficient  $\beta_{ij}^k$  have been cancelled and only cubic terms remain in the normal form.

The second result is that all *invariance breaking* terms have been cancelled. This appears because the only coupling terms that remain in the  $k$ th oscillator are proportional to  $(r_k, \dot{r}_k)$  and to a polynomial in  $(r_j, \dot{r}_j)$  with  $j \neq k$ : if non-zero initial conditions are prescribed on the  $k$ th oscillator, such that  $(r_j, \dot{r}_j) = (0, 0) \forall j \neq k$ , all coupling terms disappear, such that the dynamics is equivalent to *only one oscillator*,  $\forall t$ :

$$\ddot{r}_k^2 + \omega_k^2 r_k + (A_{kkk}^k + \gamma_{kkk}^k) r_k^3 + B_{kkk}^k r_k \dot{r}_k^2 = 0, \quad r_j = 0, \quad \forall j \neq k \quad (4.72)$$

Thanks to this *invariance* property, the above truncated normal form is then equivalent to a dynamics that takes place on an invariant manifold of the phase space, which is identified to the  $k$ th *nonlinear mode* (a CNM in the present case, see Sect. 4.4.3). Solving this dynamics gives  $r_k(t)$  and the normal transform enables to compute all modal coordinates, with relations of the form:

$$\begin{cases} q_k = r_k + \mathcal{P}_k^{(o)}(r_k, s_k) \\ v_k = s_k + \mathcal{Q}_k^{(o)}(r_k, s_k) \end{cases}, \quad \begin{cases} q_j = \mathcal{P}_j^{(o)}(r_k, s_k) \\ v_j = \mathcal{Q}_j^{(o)}(r_k, s_k) \end{cases}, \quad \forall j \neq k. \quad (4.73)$$

The above relations, independent of time  $t$ , shows that *the normal transform gives the geometry of the  $k$ th invariant manifold of the  $k$ th nonlinear mode in the phase space* since they defined a *two-dimensional manifold mapped by the coordinates*  $(r_k, s_k = \dot{r}_k)$ .

The third result is that the elimination of monomials of the initial system (4.68) *of a given order  $n$  affects or create monomials of order  $n + 1$*  in the normal form. In the case illustrated above, the quadratic terms of coefficients  $\beta_{ij}^k$  add the cubic terms  $A_{kkk}^k r_k^3$  and  $B_{kkk}^k r_k \dot{r}_k^2$  since  $(A_{kkk}^k, B_{kkk}^k)$  are function of the  $\beta_{ij}^k$  and the natural frequencies  $\omega_k$  (refer to Touzé et al. (2004a) for their analytical expressions). It must also be noted that the normal form adds velocity-dependent terms in the dynamics, that are important and sometimes overlooked in other reduction methods (Vizzaccaro et al. 2021a; Shen et al. 2021; Touzé et al. 2021).

In Touzé et al. (2004a), the coefficients of  $(\mathcal{P}^{(3)}, \mathcal{Q}^{(3)}, \mathcal{R}^{(3)})$ , up to order 3, are computed by symbolic computations and given as a function of the coefficient of the initial (modal) system  $(\beta_{ij}^k, \gamma_{ijl}^k)$ . A numerical extension of this method, directly applicable to a finite-element discretised system under the form (4.63), with a non-diagonal linear part, is proposed in Vizzaccaro et al. (2021b).

**The case of internal resonance** If an internal resonance relation between the natural frequencies  $\omega_k$  is fulfilled, then the corresponding resonant terms create small denominators in the normal transform such that they cannot be eliminated and have to be kept in the normal form, as added terms in Eq. (4.71).

As an illustration, we consider the specific case of a 1:2 internal resonance, addressed in Shami et al. (2022c) and Sect. 4.6.4. In this situation, two natural frequencies are such that  $\omega_2 \simeq 2\omega_1$ . This creates resonant terms that couple the dynamics of the two corresponding normal oscillators, which are however still invariant with respect to all the other normal coordinates. As a consequence, the dynamics can be reduced to the two oscillators:

$$\begin{aligned} \ddot{r}_1 + \omega_1^2 r_1 + \underline{\beta_{12}^1 r_1 r_2} + (\gamma_{111}^1 + A_{111}^1) r_1^3 + \underline{(\gamma_{122}^1 + A_{122}^1) r_1 r_2^2} \\ + B_{111}^1 r_1 \dot{r}_1^2 + \underline{B_{122}^1 r_1 \dot{r}_2^2} + \underline{B_{212}^1 \dot{r}_1 r_2 \dot{r}_2} = 0, \end{aligned} \quad (4.74a)$$

$$\begin{aligned} \ddot{r}_2 + \omega_2^2 r_2 + \underline{\beta_{11}^2 r_1^2} + (\gamma_{222}^2 + A_{222}^2) r_2^3 + \underline{(\gamma_{112}^2 + A_{112}^2 - D_{112}^2) r_2 r_1^2} \\ + B_{222}^2 r_2 \dot{r}_2^2 + \underline{B_{211}^2 r_2 \dot{r}_1^2} + \underline{(B_{112}^2 - E_{112}^2) \dot{r}_2 r_1 \dot{r}_1} = 0. \end{aligned} \quad (4.74b)$$

In the above equation, as announced, one can remark the appearance of additional quadratic resonant nonlinear terms associated to the 1 : 2 internal resonance (with underlines, see also Eq. (4.64a, b)). Other cubic resonant terms also appear, stemming from the polynomials  $(\tilde{P}_k^{(2)}, \tilde{Q}_k^{(2)})$ ,  $k = 1, 2$  in Eq. (4.71). The  $(A_{ijl}^k, B_{ijl}^k)$  are coefficients that come from the elimination of the non-resonant quadratic terms, whereas the  $(D_{ijl}^k, E_{ijl}^k)$  are related to the 1 : 2 internal resonance and depend on coefficient  $(\beta_{12}^1, \beta_{11}^2)$  of the two quadratic resonant terms.

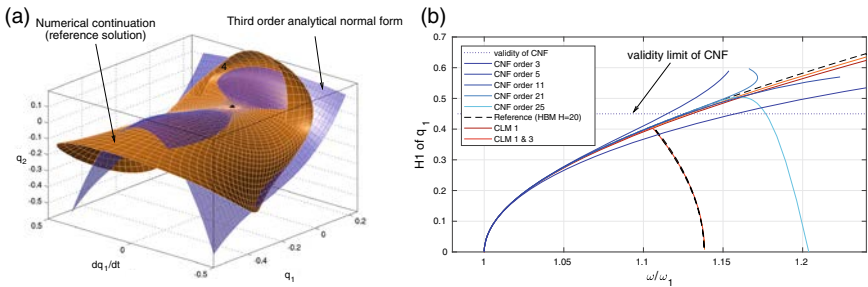
The corollary of the above two degrees-of-freedom reduced-order model is that internal resonances are responsible for a *strong coupling* between the modes of the system, created in the present case by the two underlined quadratic resonant terms. This situation arises because of the particular commensurable frequency relations of Eq. (4.66) and Table 4.3. This strong coupling is responsible for a *change of the topology* of the resonant response of the system, as illustrated in Sects. 4.6.3 and 4.6.4.

The internal resonances were analysed through a normal form, which is based on asymptotic expansions valid close to the equilibrium point  $\mathbf{x} = \mathbf{0}$ . The relationships (4.66) thus naturally appear between the *eigenfrequencies* of the linearised dynamical system. However, since the free oscillation frequencies on the nonlinear modes depend of the amplitude of the oscillations, analogous strong coupling can also appear away from the equilibrium point, if analogous frequency relations are fulfilled between the *free oscillations frequencies* of the nonlinear modes. This case will be addressed in Sect. 4.6.3.

**Validity and order of expansion** The normal form reduced-order models reported here, thanks to the invariance property, are exact in free vibration, up to the orders  $o$ ,  $p$  of the normal form expansions. Their validity is thus reduced and can be extended by increasing the orders  $o$ ,  $p$ . More generally, the normal form developments addressed above are called “oscillatory normal form” (ONF) in Chap. 2 of this book and is a particular case of the general parametrisation method of invariant manifolds. Increasing the order of this ONF above order three appear cumbersome and the current practice is to rely on normal form expansion based on complex numbers (the so-called “Complex Normal Form” (CNF)) that can be fully numerically automatised, in particular in a finite-element context, because they preserve some symmetries in the equations. On the contrary, the ONF have the advantage of keeping the equations in an oscillatory form, which is easier for vibration analyses, and, despite its current limitation to third order, is able to explain a lot of results (see examples in e.g. Sect. 4.6). Its validity limit, up to given orders  $o$ ,  $p$ , seems larger as compared to the ONF, as seen in Fig. 4.14b and addressed in Sect. 4.6.1. Moreover, analysing the validity limit of a given normal form expansion is still an open question (see some ideas in Lamarque et al. (2012), Grolet et al. (2024)) and can be checked, if possible, by comparing the geometry of the invariant manifold with respect to a reference solution or, if it is not available, to observe the convergence of the normal form for increasing orders (see Fig. 4.14).

### 4.4.5 Features of a Nonlinear Mode

**First order effect: hardening/softening behaviour** If a single CNM model reduction is considered, its oscillations are solutions of the normal oscillator (4.72). At



**Fig. 4.14** Examples of range of validity of a normal form expansion. **a** 3D view of the invariant manifold of a particular CNM, computed with a continuation method of periodic solutions and with third order ONF, showing the validity range of the latter (from Lamarque et al. (2012)); **b** convergence of backbone curves of the first CNM of a clamped-clamped beam computed with increasing order CNFs (blue) and a modal expansion (54) on 1 or 2 CLMs (red) and 20 CLMs (dashed black) (from Grolet et al. (2024)). The validity limit is also from this work

first order,<sup>4</sup> one obtains:

$$r_k(t) = \epsilon a_1 \cos(\omega_{nl} t + \varphi), \quad r_j = 0, \quad \forall j \neq k, \quad (4.75)$$

where  $\epsilon \ll 1$  is a small bookkeeping parameter,  $\varphi$  is an arbitrary phase and where the nonlinear oscillation frequency is:

$$\omega_{nl} = \omega_k \left( 1 + \frac{3\Gamma_0(\epsilon a_1)^2}{8\omega_k^2} \right), \quad (4.76)$$

with

$$\Gamma_0 = \gamma_{kkk}^k + A_{kkk}^k + \frac{B_{kkk}^k \omega_k^2}{3}. \quad (4.77)$$

Then, the oscillations of the system are obtained with the normal transform (4.69), that reads:

$$q_k = r_k + O(\epsilon^2), \quad q_j = O(\epsilon^2), \quad \forall j \neq k, \quad (4.78)$$

such that, with the modal combination (4.50b) and neglecting terms of second order:

$$\mathbf{x}(t) \simeq \epsilon \Phi_k a_1 \cos(\omega_{nl} t + \varphi). \quad (4.79)$$

Equation (4.79) shows that the first order (major) effect of the nonlinearities is to change the free oscillations frequency  $\omega_{nl}$  as a function of the amplitude  $a$  of the motion, according to Eq. (4.76). It can increase (hardening behaviour) or decrease (softening behaviour), depending on the sign of  $\Gamma_0$ , as shown in Fig. 4.15 by the backbone curve  $\omega_{nl} = f(a)$ . In addition, Eq. (4.79) shows that at this first order, meaning moderate amplitude, the motion on a given CNM is synchronous<sup>5</sup> and has the spacial shape of the *linear (CLM) mode shape*  $\Phi_k$ .

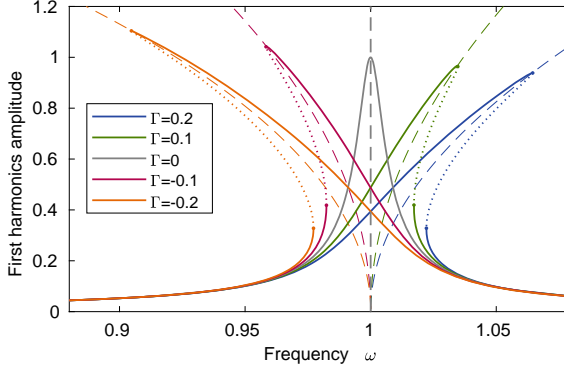
The hardening/softening behaviour of a given mode is thus governed by coefficient  $\Gamma_0$ . Its value and sign depend on the joint effect of the cubic coefficient  $\gamma_{kkk}^k$  of the  $k$ -th linear oscillator and of coefficients  $(A_{kkk}^k, B_{kkk}^k)$ , which are functions of all the quadratic coefficients  $\beta_{ij}^k$ ,  $i, j, k = 1, \dots, M$ , of the initial modal model (4.60). These quadratic coefficients are related to the  $k$ th mode but also to *all* the others, for  $i, j \neq k$ . In the case of a thin structure as those considered in Sect. 4.3, the  $\gamma_{kkk}^k$  are always positive (see Eq. (4.55)) and related to a hardening only effect due to the membrane/bending coupling (see Fig. 4.11).

A softening effect can appear because of a given curvature of the structure, or more generally of a loss of transverse symmetry in the oscillations (see Fig. 4.11), that brings the quadratic nonlinear terms into play (see Sect. 4.4.2). However, a correct estimate of this trend needs the effect of all the  $\beta_{ij}^k$  coefficients, is thus affected by all

---

<sup>4</sup> One can apply any perturbation method, such as multiple scale, averaging or harmonic balance reduced to a single harmonics.

<sup>5</sup> Synchronous means that all points of the system during the motion cross the zero position and their maximum at the same time, a characteristic of the motion onto a linear mode shape.



**Fig. 4.15** Frequency response (amplitude of the first harmonics) of a Duffing oscillator (4.81) for different values of the cubic nonlinearity coefficient  $\Gamma$ . ‘- -’: backbone curve and ‘—’: harmonically forced oscillation. HBM simulations with  $H = 20$  harmonics and  $\omega_k = 1$ ,  $\xi = 0.005$ ,  $F = 0.01$  and  $\Gamma \in \{-0.2, -0.1, 0, 0.1, 0.2\}$

linear modes in addition to the  $k$ th one and is naturally captured by the normal form through coefficients  $A_{kkk}^k$  and  $B_{kkk}^k$ . In particular, truncating the modal model (4.60) to the  $k$ th oscillator can lead to erroneous result for predicting the hardening/softening trend of the  $k$ th CNM. In this case, the analytical expressions in Touz  et al. (2004a) give:

$$A_{kkk}^k = -\frac{2(\beta_{kk}^k)^2}{3\omega_k^2}, \quad B_{kkk}^k = -\frac{4(\beta_{kk}^k)^2}{3\omega_k^4}, \quad \Rightarrow \quad \Gamma_0 = \gamma_{kkk}^k - \frac{10(\beta_{kk}^k)^2}{9\omega_k^2}, \quad (4.80)$$

such that this value of  $\Gamma_0$  can be very different from the one of Eq. (4.77) that includes the quadratic effect of all slave modes.

Including a large number of slave modes to accurately compute  $\Gamma_0$  with Eq. (4.77) was successful to predict the hardening/softening behaviour of several systems, including beams and shells, in Touz  et al. (2004a, b, 2008), Camier et al. (2009), Touz  and Thomas (2006). Since the value of  $\Gamma_0$  changes from one CNM to another one, the hardening/softening trend is mode dependent, which explains the results about the Chinese gong of Fig. 4.6.

Finally, Eqs. (4.75)–(4.77) apply as well to the simple Duffing oscillator (4.67) provided  $\Gamma_0 = \Gamma$ , such that the backbone curves of the normal oscillator (4.72) and the one of a Duffing oscillator are identical at low to moderate amplitudes: their behaviour is *equivalent*. Indeed, the effect of the cubic velocity-dependent term  $r_k \dot{r}_k^2$  can be embedded in a single cubic  $r_k^3$  by replacing the the value of its coefficient by  $\Gamma_0$  defined by Eq. (4.77). This result was numerically confirmed in Denis et al. (2018) along with the range of validity, in amplitude, of this approximation. This result will be used for experimental identification (see Sect. 4.5.2) and also for defining ex-nihilo reduced-order models (see Sect. 4.4.7).

Finally, it is possible at this first order to “artificially” add forcing and damping in Eq. (4.72), that becomes:

$$\ddot{r}_k + 2\xi_k \omega_k \dot{r}_k + \omega_k^2 r_k + \Gamma_0 r_k^3 = F \cos \Omega t. \quad (4.81)$$

This enables to simulate the forced oscillations that take place around the backbone curve (see Fig. 4.15). A more rigorous way of including damping and forcing is to consider appropriate time dependant invariant manifolds, as explained in Chap. 2 of the present book and in Opreni et al. (2023), Vizzaccaro et al. (2024).

### Second order effects: nonlinear mode shapes and backbone curves corrections

To consider higher order effects, that emerge for higher motion amplitude, we correct the result of Eq. (4.75) by adding more harmonics. Since the nonlinearity in Eq. (4.81) is odd, the constant and second harmonics have a zero amplitude, so that a higher order periodic perturbative development gives:

$$r_k = \epsilon a_1 \cos \phi + \epsilon^3 a_3 \cos 3\phi, \quad r_j = 0, \quad \forall j \neq k, \quad (4.82)$$

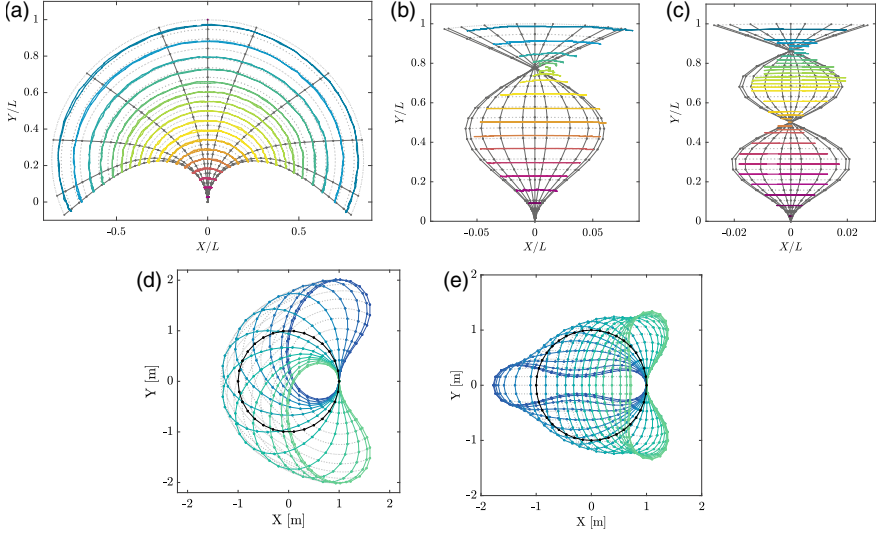
where  $\phi = \omega_{nl} t + \varphi$ . Then, thanks to the normal transform (4.69), the modal coordinate reads:

$$\begin{aligned} q_k &= r_k + \mathcal{P}_k^{(o)}(r_k, \dot{r}_k) \\ &= \epsilon^2 b_{k0} + \epsilon(a_1 + \epsilon^2 b_{k1}) \cos \phi + \epsilon^2 b_{k2} \cos 2\phi + \epsilon^3 b_{k3} \cos 3\phi + O(\epsilon^4), \\ q_j &= \mathcal{P}_j^{(o)}(r_k, \dot{r}_k) \\ &= \epsilon^2 b_{j0} + \epsilon^3 b_{j1} \cos \phi + \epsilon^2 b_{j2} \cos 2\phi + \epsilon^3 b_{j3} \cos 3\phi + O(\epsilon^4), \quad \forall j \neq k \end{aligned}$$

where the  $\{b_{ih}\}$ ,  $i = 1, \dots, M$ ,  $h = 1, \dots, H$  depend on  $(a_1, a_3)$  thanks to the polynomial  $\mathcal{P}_i^{(o)}$  of order  $o \geq 2$ . Combining the  $q_j(t)$  thanks to the modal expansion (4.50b) finally gives the oscillations of the structure on the single  $k$ th CNM as:

$$\begin{aligned} \mathbf{x}(t) &= \mathbf{\Phi}_{nl}(t) = \underbrace{\epsilon \mathbf{\Phi}_k a_1 \cos \phi}_{\text{first order, synchronous}} \\ &+ \underbrace{\epsilon^2 \sum_{i=1}^M \mathbf{\Phi}_i [b_{i0} + b_{i1} \cos \phi + b_{i2} \cos 2\phi + \epsilon b_{i3} \cos 3\phi]}_{\text{higher orders, possibly non synchronous}} + O(\epsilon^4). \quad (4.83) \end{aligned}$$

The above equation shows that the deformed shape of the  $k$ th CNM is periodic and that it is the combination of a leading sine oscillation proportional to the  $k$ th linear mode shape  $\mathbf{\Phi}_k$ , with small corrections depending on all the other mode shapes at all harmonics. Those corrections are brought by the higher harmonics of  $r_k(t)$ , but also by the normal transform (4.69), or equivalently because of the curvature of the invariant manifold. A CNM has thus a *nonlinear mode shape*,



**Fig. 4.16** Examples of nonlinear deformed shapes  $\Phi_{nl}(t)$ . **a–c** first three modes of a cantilever beam, from Debeurre et al. (2024a). Comparison between HBM computations from the geometrically exact model (Eqs. (4.18–4.20), grey) and from experiments (color); **d, e** two first modes of a ring, shown undeformed in black. HBM computations from the geometrically exact model (Debeurre et al. 2023a)

which can be *non synchronous* since it depends on time, even if this effect is *of the second order*. Some examples on nonlinear beams are given in Touzé et al. (2004b). Figure 4.16 also shows examples on a highly flexible structure at extreme amplitude. In this case,  $\epsilon$  is no more small and the deformed shape can be very amplitude and time dependant. It even happens that the nonlinear motion does not include the equilibrium position as one of its snapshots (see the ring example).

**Effect of damping** As explained in Touzé and Amabili (2006), Vizzaccaro et al. (2021b), the same normal form formalism as in Sect. 4.4.4 conducts to compute a damped nonlinear mode (DNM) that includes the effect of an initial linear diagonal damping (in the form of a modal model (4.60) or a Rayleigh model (see Sect. 4.4.1)). In this case, the dynamics onto a single DNM reads:

$$\ddot{r}_k^2 + \underbrace{2\xi_k\omega_k\dot{r}_k + C_{kkk}^k r_k^2 \dot{r}_k}_{\text{dissipative}} + \underbrace{\omega_k^2 r_k + (A_{kkk}^k + \gamma_{kkk}^k) r_k^3 + B_{kkk}^k r_k \dot{r}_k^2}_{\text{conservative}} = 0, \quad (4.84)$$

It shows that the curvature of the invariant manifold creates, in addition to the linear modal damping term of damping ratio  $\xi_k$ , a *dissipative cubic* term  $r_k^2 \dot{r}_k$ . Its coefficient  $C_{kkk}^k$  is proportional to the quadratic coefficients  $\beta_{ij}^k$  and to the damping ratio  $\xi_i$  of all the linear modes of the system (Table 4.4).

**Table 4.4** Comparisons of CLM and CNM, i.e. normal modes of conservative linear and nonlinear systems

	<i>Linear system</i>	<i>Nonlinear system</i>
Mode	<b>CLM</b> eigensolution (natural/normal mode)	<b>CNM</b> invariant manifold $\Downarrow$ family of periodic sol.
Frequency	$\omega_k$ natural/eigen frequency	$\omega_{nl} = f(\text{ampl.})$ backbone curve
Shape	$\Phi_k$ mode/eigen shape indep. of amplitude synchronous	$\Phi_{nl} = f(\text{ampl.}, t)$ nonlinear mode shape depends on amplitude non-synchronous
Coupling	Independent (orthogonality)	Invariant possible internal resonance (strongly coupled)
Invariant manifold	Flat	Curved
Free oscillations	Sinusoidal	Periodic
Stability	Always stable	Stable or unstable

As a consequence, even with an initial linear damping model, the damping of the motion onto a DNM is nonlinear and increases with the amplitude of the motion because of the non-resonant effect of all the modes. An equivalent damping ratio  $\xi_{nl}$ , that depends on the amplitude, may be defined, as in Colin et al. (2020), or may be measured by experimental continuation (see Sect. 4.5.2).

**Synthesis** In conclusion, the linear features of a CLM can be naturally extended to the nonlinear range, since:

- the natural frequency  $\omega_k$  of a CLM becomes *the free oscillations frequency*  $\omega_{nl}$  of the CNM, which depends at first order of the amplitude of the oscillations, illustrated by *the backbone curve*;
- the mode shape  $\Phi_k$  of a CLM becomes *the nonlinear mode shape*  $\Phi_{nl}(t)$  of the CNM, that is time dependent, thus non synchronous, but remains close to a synchronous motion onto  $\Phi_k$  since the nonlinear corrections are at the second order;
- a modal damping  $\xi_{nl}$  that is also amplitude-dependent.
- the motion onto a nonlinear mode is equivalent, at low amplitude, to a *single Duffing oscillator*, with the hardening/softening behaviour related to the value of the single cubic coefficient  $\Gamma_0$ .

Far from the equilibrium point, other nonlinear modes can exist, such that the number of nonlinear modes of a  $M$ -degrees-of-freedom system can be larger than  $M$  (see examples in Vakakis (1997), Cusumano and Moon (1995)).



#### 4.4.6 Reduced-Order Modelling Synthesis

Based on the above results, the reduced-order modelling strategy proposed here is based on the *invariance* of the nonlinear modes, naturally extending the CLM expansion philosophy in the case of a linear system. Two situations then arise:

- out of internal resonance areas, each nonlinear mode is invariant and a truncation to *only one master nonlinear mode*, in the form of one normal oscillator (4.72), is valid.
- if an internal resonance is observed, then *all the normal oscillators* of the nonlinear modes involved in the internal resonance must be kept in the dynamics, as exemplified by (4.74) for a 1:2 internal resonance.

This free conservative vibration reduced-order model may appear restrictive at first glance, but it constitutes in fact an excellent characterisation of the nonlinear dynamics since it constitutes *its skeleton*. In particular, the forced response of the system occurs around the *backbone curves* (see examples in Figs. 4.18 and 4.19), a result still valid in the cases of parametric excitation (see Fig. 4.26) or internal resonances (see Figs. 4.22a and 4.25), for which the topology may be more complex.

If the computation of forced and damped vibrations is under interest, a first order correction to the CNMs is to add directly in the conservative normal oscillator (4.72) the damping and forcing terms of the corresponding linear oscillator as in Eq. (4.81). A better reduced-order model may be considered with (i) the damped nonlinear mode (DNM), meaning that the invariant manifold computation includes the initial damping or (ii) the computation of a forced invariant manifold. These questions are fully discussed in Chap. 2 of this book.

#### 4.4.7 Ex-nihilo Reduced-Models

As already said, the normal form (4.70) and its resonant terms constitute the skeleton of the dynamics and thus *includes all its nonlinear dynamics features* (stability, bifurcations, number of solutions etc.). As a consequence, it can be viewed as an excellent *qualitative exploration* of the dynamics of a given system, its *quantitative aspect* being recovered by the normal transform (4.69), that enables recovering the amplitude of the initial coordinates of the system (physical or modal) but does not change qualitatively the nonlinear dynamics since its effect is at a second order in amplitude, as shown in Eq. (4.83). At first order, all modal coordinates are thus equal to the corresponding normal coordinates, such that:

$$\forall k, q_k = r_k + O(\epsilon^2), \Rightarrow \mathbf{x} = \sum_{k=1}^M \Phi_k q_k(t) = \sum_{k=1}^M \Phi_k r_k(t) + O(\epsilon^2). \quad (4.85)$$

As a consequence, the normal form method can be used as a base for building *ex-nihilo reduced-order models*. It can be built just considering a particular internal resonance, that directly leads to the number of involved nonlinear mode and the resonant terms that have to be kept in the oscillators, as detailed below.

If the dynamics appear governed by a single nonlinear mode (the  $k$ th), then, as explained in Sect. 4.4.5,  $r_j = 0 \forall j \neq k$  and a single Duffing oscillator is necessary. This reads in free conservative vibration:

$$\mathbf{x} \simeq \Phi_k r_k(t), \quad \ddot{r}_k + \omega_k^2 r_k + \Gamma_0 r_k^3 = 0. \quad (4.86)$$

If several modes are coupled by an internal resonance, then all the corresponding normal oscillators must be kept in the model, filled with suitable resonant terms. For a 1:2 internal resonance up to a cubic order, a reduced-order model can be:

$$\mathbf{x} \simeq \Phi_1 r_1(t) + \Phi_2 r_2(t), \quad \begin{cases} \ddot{r}_1 + \omega_1^2 r_1 + \beta_1 r_1 r_2 + \Gamma_1 r_1^3 + C_1 r_1 r_2^2 = 0 \\ \ddot{r}_2 + \omega_2^2 r_2 + \beta_2 r_1^2 + \Gamma_2 r_2^3 + C_2 r_2 r_1^2 = 0 \end{cases} \quad (4.87)$$

The two quadratic terms are the resonant terms associated to the internal resonance  $\omega_2 \simeq 2\omega_1$  and the cubic terms are trivially resonant.

As compared to Eq. (4.74), with the same reasoning as for the Duffing oscillator, all velocity-dependent terms have been “embedded” into the associated displacement terms, since they play the same role in the low amplitude dynamics (this can be shown by a two order multiple scale development, as shown in Shami et al. (2022c)).

This kind of strategy was successful for model identification of internal resonance: a 1:1 in circular plates (see Thomas et al. (2003), Givois et al. (2020b)), 1:2, 1:1:2 and 1:2:4 in a spherical shell, a steel pan and a chinese gong (Jossic et al. 2018; Thomas et al. 2007; Monteil et al. 2015).

## 4.5 Frequency Domain Computation and Identification

In parallel to the reduction methods discussed in Sect. 4.4, it is important to have at our disposal dedicated tools to accurately compute the nonlinear dynamics, as well as to experimentally identify it. For linear vibration analyses, the common practice is to switch to the *frequency domain*, by considering the *harmonic vibrations* of the system in the *steady state*, thanks in particular to Frequency Response Functions (FRFs, the ratio of the Fourier Transforms of the output and the input of a given linear system), that are amplitude independent characterizations of the system (see Table 4.5). FRF can be estimated by measuring the vibratory response of a system subjected to any wide-band signal (chirp, random, shock...). A sine forcing can also be equivalently used to address the behaviour of the system at a particular frequency, irrespective of its value. However, if non-linearities are at hand, the behaviour of the system is amplitude dependent and does not fulfil the superposition principle. Consequently, the choice of the excitation signal has a major influence on the measured behaviour

**Table 4.5** Summary of basic processes for analysis of linear and nonlinear vibratory systems.  $\hat{x}$  is the Fourier transform of  $x(t)$

	<i>Linear system</i>	<i>Nonlinear system</i>
<i>Free response</i> $f_e = \mathbf{0}$	Natural modes	Nonlinear modes
<i>Forced response</i>	$f_e(t)$ arbitrary $\hat{x}_i = H_{ij} \hat{f}_{ej}$ FRF $H_{ij}(\omega)$ independent of $f_e$	$f_e(t) = a f_0 \cos \omega t$ response $\mathbf{x}(t)$ to a sine forcing $\hat{x}/a$ depends on $a$ $\mathbf{x}(t)$ periodic, quasi-periodic, chaotic
<i>Analysis tools</i>	Linear systems inversion	Numerical continuation

of the system. A natural method, which is also the simplest one, is to analyse the behaviour of a nonlinear system in the *steady state*, under *harmonic forcing*.

Then, dedicated methods have to address the computation of the several classical vibratory regimes of nonlinear systems (see Sect. 4.2.4): *periodic*, *quasi-periodic* or *chaotic*, as well as the associated transitions, linked to *instabilities* and *bifurcations*. From both the numerical and experimental sides, a powerful tool is *continuation*, to which the following give a short overview.

### 4.5.1 Numerical Continuation Methods

Continuation methods, or path-following methods, consist in computing the solution of a system in a particular *steady-state*, and following its evolution when a parameter (the so called *control parameter*) is varied. This state being computed, its stability can be evaluated in a second step, as well as bifurcations. The first particular states that have received most attention is equilibrium (or stationary) solutions, in the context of structural buckling analysis (see the “Riks” like methods in commercial finite-element codes, Crisfield (1981)). Then, for nonlinear dynamics applications, continuation of stationary solutions is extended to periodic solutions, which is the basic tool addressed hereafter, currently available in many software packages AUTO (Doedel et al. 2002), MATCONT (Dhooge et al. 2003), COCO (Dankowicz and Schilder 2013), MANLAB (Guillot et al. 2018), NLVIB (Krack and Gross 2019). Continuation methods can be a fantastic tool to solve many practical problems, from the computation of manifolds in the phase space (Krauskopf et al. 2007) to more engineering based applications such as tracking of bifurcation points and isolated branches (isolas) Grenat et al. (2019) or quasi-periodic solutions continuation (Guillot et al. 2017).

**Continuation of periodic solutions** The starting point is to consider a  $K$ -dimensional first order dynamical system ( $K \in \mathbb{N}$ ):

$$\dot{\mathbf{y}} = \mathbf{g}(\mathbf{y}, t, \lambda), \quad (4.88)$$

with  $\lambda \in \mathbb{R}$  a control parameter,  $t \in \mathbb{R}$  the time,  $\mathbf{y}(t) \in \mathbb{R}^K$  and  $\mathbf{g} : \mathbb{R}^{K+2} \rightarrow \mathbb{R}^K$  a smooth vector field. Finding a periodic solution of the above problem, for a given value of  $\lambda$ , consists in finding a couple (initial solution, period)  $(\mathbf{y}_0, T) \in \mathbb{R}^K \times \mathbb{R}^{*+}$  such that it exists  $\mathbf{y}(t)$  solution of (4.88) with  $\mathbf{y}(0) = \mathbf{y}(T) = \mathbf{y}_0$ .

Time domain strategies may be considered, such as *shooting* methods (see Nayfeh and Balachandran (1995), Peeters et al. (2009), Seydel (2010)) or methods which reformulate the above problem into a boundary value problem, such as the one used in the AUTO software (see Doedel et al. (2002), Arquier et al. (2006), Karkar et al. (2014)). In this text, we focus on the frequency domain *Harmonic Balance Method* (HBM).

It consists in expanding the unknown solution into a Fourier series:

$$\mathbf{y}(t) = \hat{\mathbf{y}}^{(0)} + \sum_{h=1}^H \left( \hat{\mathbf{y}}^{(hc)} \cos h\omega t + \hat{\mathbf{y}}^{(hs)} \sin h\omega t \right), \quad (4.89)$$

with  $\omega = 2\pi/T$  the angular frequency of the periodic solution,  $\hat{\mathbf{y}}^{(0)}$ ,  $\hat{\mathbf{y}}^{(hc)}$ ,  $\hat{\mathbf{y}}^{(hs)}$ ,  $h = 1, \dots, H$  the Fourier coefficients (constant vectors) and  $H \in \mathbb{N}$  the number of harmonics. Introducing (4.89) into (4.88) and balancing the harmonics (or equivalently using a Galerkin procedure, see Krack and Gross (2019)) leads to replace (4.88) by a  $P$ -dimensional algebraic problem of the form ( $P \in \mathbb{N}$ ):

$$\mathbf{R}(\mathbf{Y}, \omega, \lambda) = \mathbf{0}, \quad (4.90)$$

where  $\mathbf{Y} \in \mathbb{R}^P$  and  $\mathbf{R} : \mathbb{R}^{P+2} \rightarrow \mathbb{R}^P$  is a smooth vector field.  $\mathbf{Y}$  contains all the Fourier coefficients  $\{\hat{\mathbf{y}}^{(0)}, \hat{\mathbf{y}}^{(hc)}, \hat{\mathbf{y}}^{(hs)}\}$ ,  $h = 1, \dots, H$ , such that the size of the problem is  $P = (2H + 1)K$ . This HBM method is often the one preferred for large scale (finite-element discretised) systems (see Krack (2015), Blahoš et al. (2020), Woiwode et al. (2020)), as compared to time domain methods.

Thanks to the implicit function theorem,<sup>6</sup> continuation consists in finding branches of solutions of (4.90) in the space  $(\mathbf{Y}, \lambda)$ , on a given range of  $\lambda$ . Since  $\mathbf{R}$  is a nonlinear function of  $\mathbf{Y}$ , several solutions exist for a given  $\lambda$ , they can have a complex shape, can fold on themselves and cross at bifurcation points... To this end, an arclength parameter  $a$  is used to re-parametrise the problem and compute  $(\mathbf{Y}, \lambda)$  as a function of  $a$  (see Crisfield (1981), Seydel (2010), Cochelin and Vergez (2009)). Then, (4.90) can be solved by standard predictor corrector/ methods or less standard high order predictor methods, such as the Asymptotic Numerical Method (ANM), considered for the numerical computations in this text, thanks to the software MANLAB (Cochelin and Vergez (2009), Guillot et al. (2018, 2019)).

---

<sup>6</sup> The implicit function theorem states that as soon as  $\partial \mathbf{R} / \partial \mathbf{Y}$  exists and is non singular, there exists a continuously differentiable function  $\mathbf{h}$  such that  $\mathbf{Y} = \mathbf{h}(\lambda)$ , constituting a branch of solution.

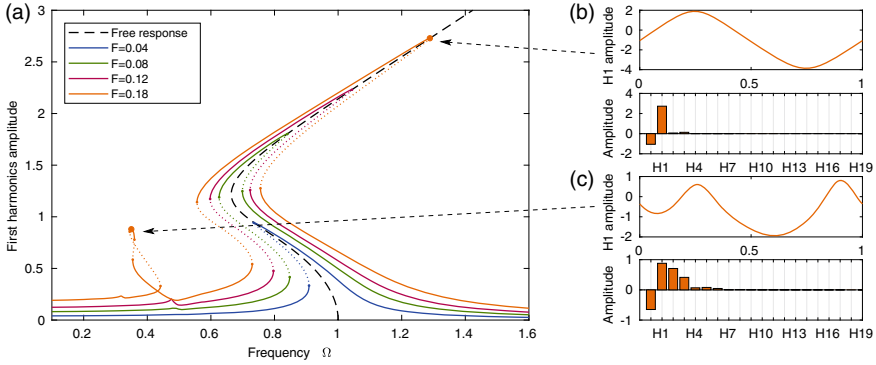
**Stability and bifurcations** Continuation methods, as described above, are able to compute solutions, whatever be their stability, that can be addressed in a second step. For time domain methods, the stability is usually computed with the eigenvalues of the so-called monodromy matrix (Nayfeh and Balachandran 1995; Peletan et al. 2013), obtained as a by product of shooting methods or by time integration over one period of a linear matrix differential equations of size  $P$ . In an HBM context, such an approach do not take advantage of the frequency nature of the HBM, which led the development of frequency domain methods, based on computing the eigenvalues of the Hill matrix, strongly related to the Jacobian of (4.88). Since the Hill matrix is of size  $P = (2H + 1)K$  and that only  $K$  eigenvalues (the Floquet exponents) are to be determined, some sorting method have been developed (Zhou et al. 2003; Lazarus and Thomas 2010; Guillot et al. 2020), recently reconsidered with the Koopman formalism (Bayer and Leine 2024; Bayer et al. 2024).

For the bifurcation analysis, one can first monitor the change of stability of a given branch and deduce the type of bifurcation from the way the real part of the characteristic eigenvalues (either those of the Jacobian of  $\mathbf{g}$  for time domain methods, or the Floquet exponents for frequency domain methods) cross the imaginary axis (Seydel 2010; Lazarus and Thomas 2010; Guillot et al. 2020). This can be made more robust by the help of bifurcation test functions (Seydel 2010). Finally, the crossing of several branches, linked to pitchfork or transcritical bifurcations, can be identified in the Taylor series using a specific method in the ANM (Cochelin and Medale 2013).

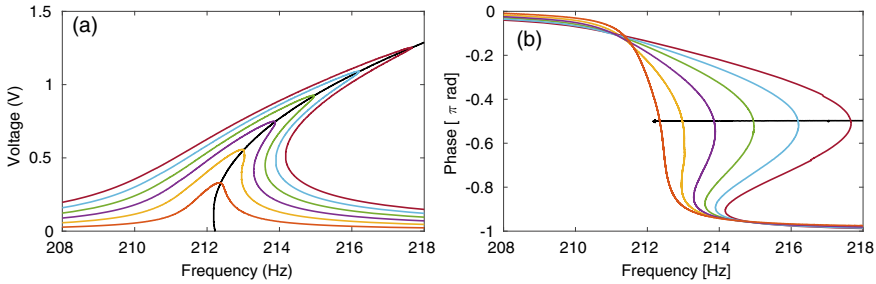
**Synthesis** Continuation methods, and especially the one based on HBM, enables a very precise computation of the dynamics since one has access to each harmonics separately, the stability and the bifurcations of all branches, but can also rely on approximate fast computations by reducing the number of harmonics. It is also easy to address the four types of practical continuation cases (self-sustained oscillations, free-conservative systems to compute conservative nonlinear modes, harmonically forced systems continued in frequency ( $\lambda = \omega$ ) or continued at fixed frequency, with  $\lambda$  being the amplitude of the forcing or another parameter, see Guillot et al. (2020)). Examples of computation are given in Figs. 4.15, 4.16, 4.17, 4.19, 4.20, 4.22, 4.23, 4.24, 4.25 (Fig. 4.21).

## 4.5.2 *Experimental Continuation Methods*

Experimental tests in the case of vibration analysis are often performed for a validation of a given model and/or the identification of its parameters. In the case of a linear system, the standard test is an experimental modal analysis, which consists first in measuring the FRFs of the system (using any kind of wide band input signal since the linearity of the system enforces the independence of the FRF on this input) and then using dedicated algorithms to identify the modal parameters (natural frequencies  $\omega_k$ , mode shapes  $\Phi_k$ , modal damping factors  $\xi_k$  and modal masses  $m_k$ , see Sect. 4.4.2 for



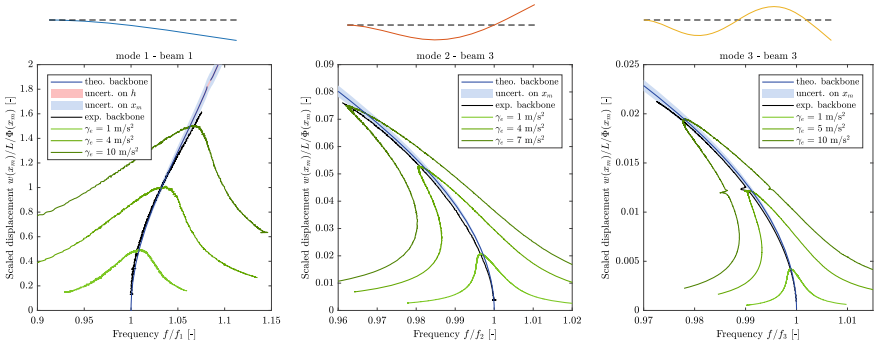
**Fig. 4.17** Response of a Duffing oscillator with a quadratic term of the form  $\ddot{x} + 0.05\dot{x} + x + x^2 + 0.3x^3 = F \cos \omega t$  computed with the HBM in Manlab. ‘—’: stable branches and ‘- -’: unstable branches. **a** Frequency response curves for various values of  $F$  as well as the backbone curve. **b, c** Time evolution of  $x(t)$  at resonance and 1 : 2 super-harmonic resonance and harmonic content



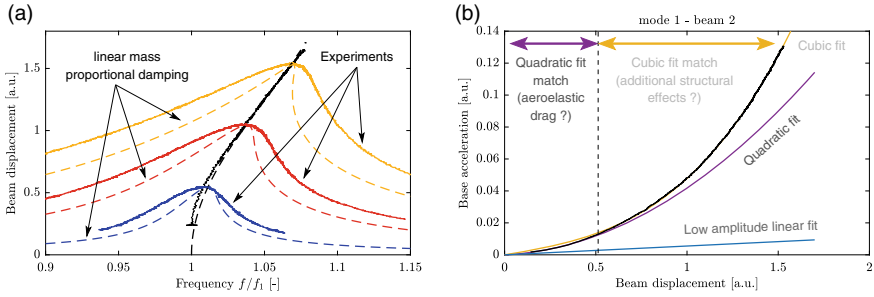
**Fig. 4.18** Experimental frequency response of a circular plate driven and measured with piezoelectric patches, obtained with PLL continuation, from Givois et al. (2020a). The backbone curve (amplitude sweep at  $\varphi = -\pi/2$ ) is plotted in black whereas several frequency response (phase sweep at constant input voltage  $V$ ) are plotted in color for different value of  $V$ . **a** output voltage as a function of the frequency  $\Omega$ ; **b** phase lag  $\varphi$  between output and input as a function of  $\Omega$

the notations and Gérardin and Rixen (2015), Ewins (2000), McConnell and Varoto (2008)).

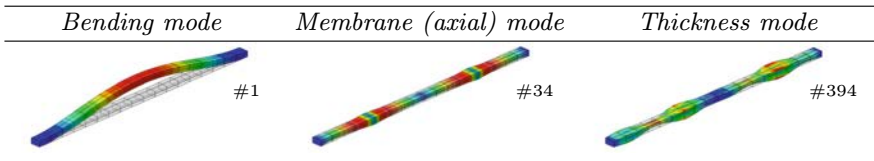
When non-linearities are at hand, as done for numerical computations in Sect. 4.5.1, it is possible to extend those linear practice to the nonlinear range, by designing dedicated methods (called *experimental continuation*) able to address the *measurement* of nonlinear frequency responses, including their unstable branches (see an example in Fig. 4.18). Then, it is also possible to proceed to the *identification* of the *nonlinear modes* and their particular features (see Sect. 4.4.5), the fundamental one being that its characteristic frequency  $\omega_{nl}$ , damping  $\xi_{nl}$  and shape  $\Phi_{nl}(t)$  are amplitude dependent, all of them well defined by the *backbone curve*, that can be also directly measured by experimental continuation in a robust way.



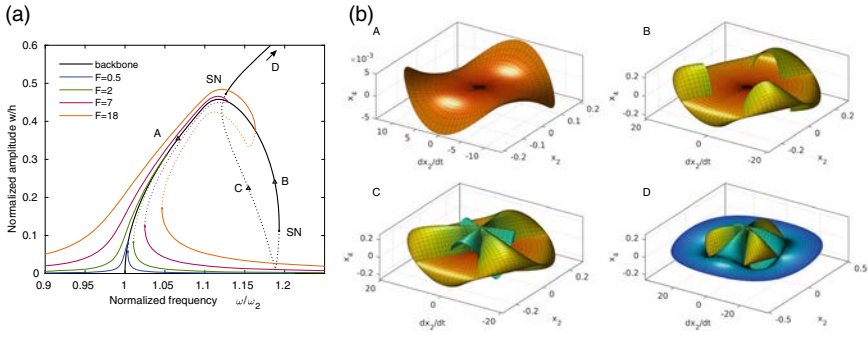
**Fig. 4.19** Frequency response of a cantilever beam at extreme amplitude, obtained both experimentally with PLL continuation and compared to HBM computations of the geometrically exact model (Eqs. (4.18–4.20)), from Debeurre et al. (2024a). The backbone curves are plotted in black (experiments) and blue (finite element computation), whereas several experimental frequency responses are plotted in green. From left to right: mode 1, mode 2 and mode 3. The nonlinear deformed shapes are shown in Fig. 4.16



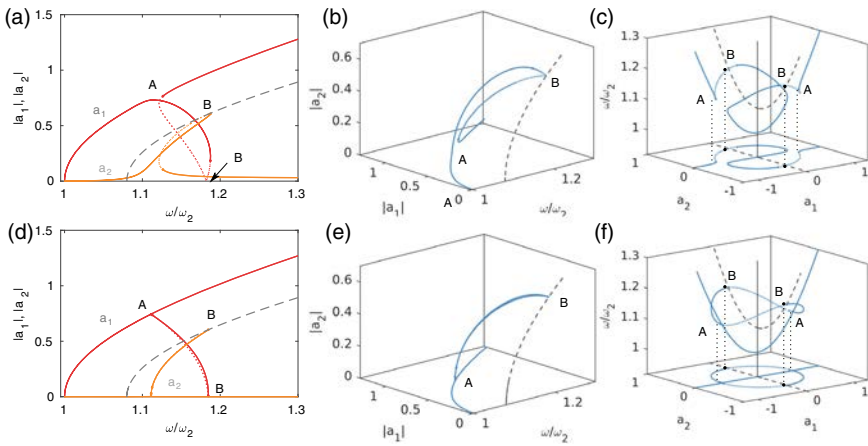
**Fig. 4.20** **a** Comparison between the experimental frequency response of the first mode of the cantilever beam of Fig. 4.19, from Debeurre et al. (2024a) (black: backbone curve; color: forced response) and a geometrically exact model with mass proportional damping adjusted at resonance ( $C = 2\omega_1\xi M$  with  $\xi \in \{1.49, 2.74, 3.81\}\%$  for the three curves, from low to high amplitude); **b** amplitude of forcing as a function of beam displacement on the backbone curve, along with several polynomial fits



**Fig. 4.21** Examples of axial and thickness mode shapes that are strongly coupled to the first bending mode, due to the quadratic non-resonant terms, and their order of appearance in the CLM modal basis



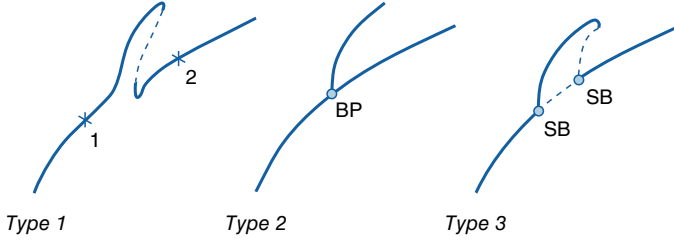
**Fig. 4.22** **a** Backbone curve (black) and resonance curve (colors) of the second bending mode of a clamped-clamped beam under harmonic forcing  $F \cos \omega t$  at  $0.275L$  (a node of the fourth natural mode shape) with amplitude  $F = \bar{F} EI / (\rho L^4)$  and  $\bar{F} \in \{0.5, 2, 7, 18\}$ . SN means Saddle-Node bifurcation. **b** Plots of the invariant manifold in the space  $(q_2, \dot{q}_2, \dot{q}_4)$  at several locations (A,B,C,D) on the backbone curve



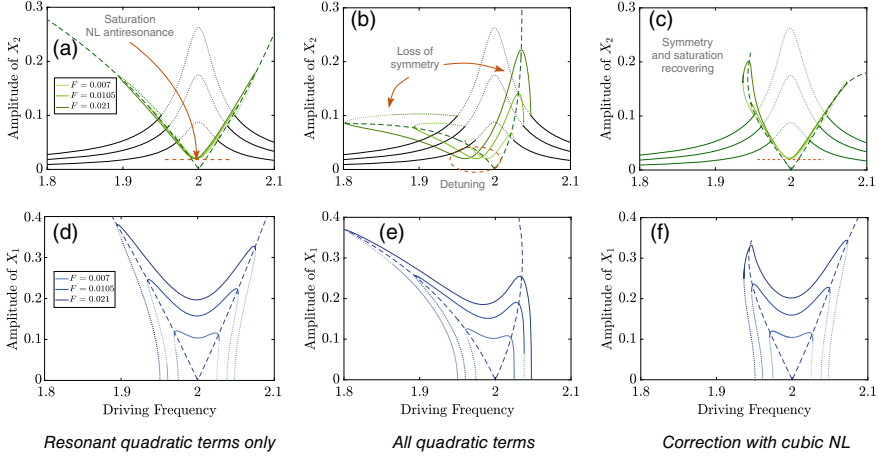
**Fig. 4.23** Topology of a 1:3 internal resonance. Periodic solutions of Eq. (4.102) in free undamped vibrations. First line: simulation with coefficients  $(\Gamma_i, C_j)$  of the internal resonance between CNM 2 and 4 of a clamped-clamped beam. Second line: same coefficient values, with vanishing resonant terms,  $C_2 = \Gamma_3 = 0$ . **a, b, d, e** 3D view in the spaces  $(a_1 = a_{1H1}, a_2 = a_{2H3}, \omega/\omega_2)$  and  $(\omega/\omega_2, |a_{1H1}|, |a_{2H3}|)$ . (blue): backbone curve of CNM2; (dashed grey): backbone curve of CNM4 plotted as a function of  $\omega/3$ . **e, f** 2D view in the plane (amplitude, frequency)

**Phase locked loop** The basic technique to measure nonlinear vibrations is the stepped sine: one chooses a frequency of excitation  $\omega$  and a forcing level  $F$ , waits for the steady state, measures the vibrations of the structure  $x(t)$  in one point and repeats this operation for a list of successive frequencies  $\omega$ , in an increasing (upward stepped sine) or decreasing (downward stepped sine) order, around a resonance. An example of result is given in Fig. 4.6, that include jumps between the low and the





**Fig. 4.24** Topology of internal resonances in a transversely (cubic only) system. BP means “branch point”, i.e. the crossing of to branches of solution; “SB” denotes a symmetry breaking bifurcation



**Fig. 4.25** 1:2 internal resonance between two tuned CNMs in a piezoelectric structure connected to a nonlinear electronic circuit, from Shami et al. (2022c). **a–c** amplitude of the first harmonics H1 of the mechanical mode as a function of driving frequency  $\omega$ ; **c–e** amplitude of the sub-harmonic H1/2 of the electrical mode, as a function of driving frequency  $\omega$

high amplitudes branches. An estimation of the backbone curve can then be obtained by plotting the couple (amplitude, frequency) at the resonance obtained after several stepped sine tests, for increasing values of  $F$ .

A powerful alternative is to rely on a *phase locked loop* (PLL) strategy. Whereas the stepped sine method consists in prescribing the driving frequency  $\omega$ , the idea is to use an external real-time control loop able to automatically adapt the driving frequency  $\omega$  such that the *phase lag* between the response  $x(t)$  and the forcing signal follows a prescribed value.

As discussed in Sect. 4.4.5, the dynamics of a given conservative nonlinear mode (CNM) without internal resonance at low amplitude is equivalent to a Duffing oscillator, of Eq. (4.81). Its response can be written:

$$r_k(t) = a \cos(\Omega t + \varphi) + \text{hh}, \quad (4.91)$$

with hh meaning “higher harmonics”. As shown in Fig. 4.18, whereas the relation  $\Omega \mapsto a$  is multivalued because of different branches of solution,  $\varphi \mapsto \Omega$  and  $\varphi \mapsto a$  are single valued functions.<sup>7</sup> With this in mind, measuring a frequency response with a PLL experimental continuation strategy simply consists in realising a *phase sweep* around  $-\pi/2$ . Then, it can be shown (see Denis et al. (2018)) that the system’s periodic steady state responses are identical with the PLL in closed loop or in open loop, at the difference that the closed loop stabilizes the unstable branches of the open loop. Consequently, the PLL enables the *measurement of full frequency responses, including its unstable parts*.

Moreover, a zoom around the resonance of a Duffing oscillator, e.g. in Fig. 4.15, would show (see the picture in Denis et al. (2018)) that three curves coexist: (i) the amplitude resonance, locus of the maximum of the frequency response when the amplitude of the forcing is varied, (ii) the saddle node bifurcation point, where the stability changes, and, in between, (iii) the *backbone curve of the CNM*, defined as the free oscillation frequency as a function of the amplitude. In experiments, for light damping, it is virtually impossible to tell them apart. Interestingly, it is shown in Peeters et al. (2011), Debeurre et al. (2024a) that the *backbone curve of the CNM* coincides with a *phase resonance curve*, associated to a particular  $\pi/2$  phase shift between the system’s periodic response and the forcing. Consequently, the same PLL apparatus is able to *directly measure the backbone curve of a CNM*, by enforcing  $\varphi = \pi/2$  and increasing the forcing amplitude. For technical details about the control loop and practical aspects about the experimental apparatus, the interested reader can refer to Denis et al. (2018), Debeurre et al. (2024a), Abeloos et al. (2022) and reference therein.

**Phase resonance** To understand the phase resonance condition, the following dynamical system is considered:

$$\mathbf{M}(\mathbf{x})\ddot{\mathbf{x}} + \mathbf{f}_d(\mathbf{x}, \dot{\mathbf{x}}) + \mathbf{f}_c(\mathbf{x}, \dot{\mathbf{x}}) = \mathbf{f}_e, \quad (4.92)$$

where  $\mathbf{x}(t) \in \mathbb{R}^N$  is the displacement vector at time  $t$ ,  $\mathbf{M}(\mathbf{x})$  is the  $N \times N$  mass matrix which may depend on  $\mathbf{x}$  because of inertial nonlinearities,  $\mathbf{f}_d(\dot{\mathbf{x}}, \mathbf{x})$  is the  $N$ -dimensional dissipative force vector, a smooth function the velocity  $\dot{\mathbf{x}}$  and the displacement  $\mathbf{x}$ ,  $\mathbf{f}_c(\mathbf{x}, \dot{\mathbf{x}})$  is the  $N$ -dimensional internal conservative force vector, also a smooth function of  $\mathbf{x}$ , and of  $\dot{\mathbf{x}}$  in the case of inertial nonlinearities, and  $\mathbf{f}_e(t)$  is the  $N$ -dimensional external force vector that depends on time. Equation (4.92) is very general and well-suited for modeling several types of systems. It includes in particular all the finite-element discretised models seen in Sect. 4.3, the modal models of Sect. 4.4.2 and also the damped normal form (4.84).

An important property, proven in Debeurre et al. (2024a), is that the conservative force vector  $\mathbf{f}_c(\mathbf{x}, \dot{\mathbf{x}})$  is an *even function* of  $\dot{\mathbf{x}}$  whereas the dissipative force vector  $\mathbf{f}_d(\mathbf{x}, \dot{\mathbf{x}})$  is an *odd function* of  $\dot{\mathbf{x}}$ . Consequently:

---

<sup>7</sup> For any value of  $\varphi \in [-\pi, 0]$ , there is a unique associated pair  $(a, \Omega)$ .

$$\begin{cases} f_c(\mathbf{x}, \dot{\mathbf{x}}) = f_c(\mathbf{x}, -\dot{\mathbf{x}}), \\ f_d(\mathbf{x}, \dot{\mathbf{x}}) = -f_d(\mathbf{x}, -\dot{\mathbf{x}}). \end{cases} \quad (4.93)$$

If we now consider a given *conservative nonlinear mode* (CNM) of (4.92), its motion  $\mathbf{x}_{\text{cnm}}(t)$  verifies the free conservative part of (4.92), reading:

$$\mathbf{M}(\mathbf{x}_{\text{cnm}})\ddot{\mathbf{x}}_{\text{cnm}} + \mathbf{f}_c(\mathbf{x}_{\text{cnm}}, \dot{\mathbf{x}}_{\text{cnm}}) = \mathbf{0}. \quad (4.94)$$

Then, since  $\mathbf{f}_c(\mathbf{x}, \dot{\mathbf{x}})$  is an even function of  $\dot{\mathbf{x}}$ , it is shown in Debeurre et al. (2024a) that the natural solution of (4.94) is a *monophase motion*, such that:

$$\mathbf{x}_{\text{cnm}}(t) = \hat{\mathbf{x}}_0 + \sum_{h=1}^H \hat{\mathbf{x}}_h \cos(h\omega t) + \text{hh}, \quad (4.95)$$

with hh meaning “higher harmonics” and  $\{\hat{\mathbf{x}}_0, \hat{\mathbf{x}}_h\}$  being Fourier components.

Moreover, since  $\mathbf{f}_d(\mathbf{x}, \dot{\mathbf{x}})$  is an even function of  $\dot{\mathbf{x}}$ , it can also be shown that it is also monophase, each of its harmonics being phase shifted of  $-\pi/2$ , reading:

$$\mathbf{f}_d(\mathbf{x}_{\text{cnm}}, \dot{\mathbf{x}}_{\text{cnm}}) = \sum_{h=1}^H -\hat{\mathbf{f}}_{dh} \sin(h\omega t), \quad (4.96)$$

with  $\{\hat{\mathbf{f}}_{dh}\}$  being the Fourier components of  $\mathbf{f}_d$ .

Finally, if one assumes that the motion of the forced and damped system (4.92) is onto a CNM,  $\mathbf{x} = \mathbf{x}_{\text{cnm}}$  verifies the conservative part (4.94). Introducing Eq. (4.94) into (4.92) shows that the equation of motion is split into a free/conservative part and a forced/dissipative part, that reads:

$$\mathbf{f}_d(\mathbf{x}_{\text{cnm}}, \dot{\mathbf{x}}_{\text{cnm}}) = \mathbf{f}_e = \sum_{h=1}^H -\hat{\mathbf{f}}_{eh} \sin(h\omega t), \quad (4.97)$$

with  $\hat{\mathbf{f}}_{eh} = \hat{\mathbf{f}}_{dh}$ . Comparing Eqs. (4.95) and (4.97), it is observed that *the external force vector associated to the motion onto a monophase CNM exactly cancels the dissipations and is also monophase, characterised by a phase lag of  $\pi/2$  of each harmonic with respect to the displacement response, regardless of the form of the dissipative forces.*

**Force appropriation** Therefore, applying a force appropriation procedure, i.e. controlling the frequency  $\omega$  of the external force  $\mathbf{f}_e(t)$  as well as the shapes  $\hat{\mathbf{f}}_{eh}$  for  $h = 1, 2, \dots, H$  of its harmonics such that their phases have a phase lag of  $\pi/2$  with respect to the corresponding harmonic of the displacement  $\mathbf{x}(t)$  enables *the conservative nonlinear mode  $\mathbf{x}_{\text{cnm}}$  to be measured, regardless of the dissipative forces.*

In practice, realizing the exact force appropriation, i.e. finding the vectors  $\hat{\mathbf{f}}_{eh}$  that exactly cancel the harmonics of  $\mathbf{f}_d(\mathbf{x}_{cnm}, \dot{\mathbf{x}}_{cnm})$  according to Eq. (4.97), needs two aspects: finding the correct space shape of the vectors  $\hat{\mathbf{f}}_{eh}$  that mirror the damping space distribution and including enough harmonics  $H$  in the forcing.

These two aspects are *a priori* unknown and impossible to fulfill exactly in practical experiments, particularly the former. However, if the motion were perfectly on a CNM (Eq. (4.97)), it would lie very close to the associated invariant manifold in the phase space (see Sect. 4.4), such that the *space distribution* of the force is not important at first order since the resonant CNM dominates. This is the extension of the linear resonance concept to the nonlinear regime: if the modes of a structure are spaced enough in frequency and lightly damped, the motion at a given resonance is governed by only one mode, almost irrespective of the space distribution of the forcing.<sup>8</sup> In practice, then, the space distribution of the forcing may be chosen according to the apparatus available: point forcing as in Peeters et al. (2011), Denis et al. (2018), Jossic et al. (2018), Givois et al. (2020b), Peter and Leine (2017), Scheel et al. (2018), Peter et al. (2019), Scheel et al. (2018), piezoelectric forcing (see Givois et al. (2020a)) or base acceleration forcing (see Debeurre et al. (2024a), Abeloos et al. (2022), Kohlmann et al. (2020), Müller et al. (2022)).

Regarding the second aspect, i.e. the number of harmonics, it is theoretically possible to synthesize several controlled harmonic components in the force, but most practical situations show that a single harmonic forcing is sufficient.

Examples of experimental resonant responses obtained by the present method are shown in Figs. 4.18 and 4.19, that includes in each case both the backbone curve and a few forced frequency responses with their unstable branches.

It must also be noticed that the PLL is part of a larger family of experimental continuation methods (see Sieber and Krauskopf (2008), Barton and Burrow (2011), Bureau et al. (2014), Renson et al. (2016), Abeloos et al. (2022)) and that force appropriation is a common practice in ground vibration testing of aircrafts (see Giclais et al. (2016)).

**Nonlinear mode identification** The above described PLL experimental continuation procedure enables the measurement of both the backbone curve and the frequency responses that lie around it. As a consequence, those results can be easily compared to a model, for validation or parameter estimation. The best strategy is to consider the backbone curve which, as addressed in the previous section, gives the *conservative response* of the system, out of any damping effects, that is, as addressed in Sect. 4.4.1, not easy to be modelled accurately.

If no structural model of the structure is available, the normal form theory (see Sect. 4.4.7) assures that at low amplitude, a simple Duffing oscillator (4.86) captures the dynamics on one mode, such that its single coefficient  $\Gamma = \Gamma_0$  can be identified as the curvature of the backbone curve, following Eq. (4.77). This has been successfully done for several modes of a circular plates (all hardening) and some modes of chinese

---

<sup>8</sup> One must in particular exclude the case of a point forcing precisely on a node of the mode shape of the considered mode, which nullifies the corresponding modal forcing and the resonance.

gong, being hardening or softening in Denis et al. (2018), Jossic et al. (2018), Givois et al. (2020b).

If a structural model is at hand, then all this can be applied for validation. As an example, Figure 4.19 shows a perfect match between the experimental and numerical backbone curve of a cantilever beam (Debeurre et al. 2024a). At several points of the backbone curve, one can also identify the *nonlinear deformed shape* of the mode (see Fig. 4.16).

Finally, the measurement of the backbone curve also enables to identify the *damping law* as a function of the amplitude, by plotting the amplitude of the forcing as a function of the structural response. An example is reported in Fig. 4.20 showing that the modal damping is an increasing function of the amplitude, as a law quadratic at low amplitude and cubic at higher amplitude (refer to Debeurre et al. (2024a) for other details).

**Synthesis** The PLL continuation tool appears to be very attractive for nonlinear structural testing since it enables the identification (i) the forced frequency response including its *unstable branches*, (ii) the *conservative backbone curve* and (iii) an associated *modal damping law*. In the case of a single nonlinear mode motion, it clearly matches with the single invariant manifold reduction proposed in Sect. 4.4.5, enabling clear identification of a nonlinear mode and in particular its hardening/softening behaviour.

In more complex cases such as those including internal resonance, it is also possible to obtain similar results, as shown in Denis et al. (2018), Givois et al. (2020a, b) for a 1:1 internal resonance. The extension to more complex internal resonance is an attractive perspective, that has to be linked to the *ex-nihilo* modelling linked to normal form and resonant term addressed in Sect. 4.4.7.

Finally, it must be noticed that the conservative/dissipative split at the origin of the coincidence between a phase resonance and a *conservative* nonlinear mode is a priori not fulfilled in the case of dry friction nonlinearities, leading to the measurement of a damped nonlinear mode (see discussions in Debeurre et al. (2024a) and references therein, as well as Chap. 5 of this book).

## 4.6 Illustrations, Applications and Test Cases

This section gathers a few applications of Sect. 4.4 in order to reduce, understand and compute the dynamics of some elastic and piezoelectric structures.

### 4.6.1 Cubic Models for Flat Structures

**Structures with membrane/bending coupling** We consider the special case of structures subjected to geometrical non-linearities stemming from a mem-

brane/bending coupling (see Fig. 4.12, left). To understand this particular mechanism, we consider the modal expansion of any *finite-element discretization* of the structure, with 3D, plate or shell elements, in the form of Eq. (4.60), in which each (linear) modal coordinate  $q_k(t)$  is coupled to the others by quadratic and cubic terms.

If we first consider a flat (or transversely symmetric structure), an analytical von Kármán model shows that the axial motion is *quadratically coupled* to the bending motion (see Eqs. (4.32), (4.40b)). Moreover, because the structure is flat, the membrane and bending motions are uncoupled at the linear level (see Eq. (4.22) without the  $Nw'$  term, or Eq. (4.40) without the  $L(\diamond, \diamond)$  terms). Then, the CLMs can be exactly split into a family of  $M_w \in \mathbb{N}$  bending only modes (of coordinates  $\{q_k(t)\}_{k=1\dots M_B}$ ) and a second family of the remaining  $M_u = M - M_B$  non bending modes (membrane or thickness modes, of coordinates  $\{\eta_p(t)\}_{p=1\dots M_u}$ ), see Fig. 4.21. As a consequence, it is possible to rewrite Eq. (4.60) under the following form (see Givois et al. (2019), Vizzaccaro et al. (2020)),  $\forall k = 1, \dots, M_w, \forall p = 1, \dots, M_u$ :

$$\ddot{q}_k + \omega_k^2 q_k + \sum_{p=1}^{M_u} \sum_{i=1}^{M_w} C_{pi}^k \eta_p q_i + \sum_{i=1}^{M_w} \sum_{j=1}^{M_w} \sum_{l=1}^{M_w} D_{ijl}^k q_i q_j q_l = F_k \quad (4.98a)$$

$$\ddot{\eta}_p + \varpi_p^2 \eta_p - \sum_{i=1}^{M_u} \sum_{j=1}^{M_w} G_{ij}^p q_i q_j = 0 \quad (4.98b)$$

where we changed notations for clarity:  $\varpi_p$  corresponds to  $\omega_\diamond$  for the non-bending modes,  $D_{ijl}^k$  correspond to a cubic coefficient  $\gamma_{\diamond\diamond\diamond}^k$  that couples four bending modes,  $(C_{pi}^k, G_{ij}^p)$  are two quadratic coefficients  $\beta_{\diamond\diamond}^k$  that couple one membrane mode and two bending modes, and all the other coefficients are zero. One can also notice that the membrane forcing is set to zero since only transverse loads are considered.

If one considers that the non-bending modes are of much higher frequency than the bending modes, then their inertia can be neglected (this assumption is also used for the von Kármán analytical models, see Sect. 4.3) and it is possible to exactly condense the non-bending motion into the bending motion, leading to a purely cubic model in the  $\{q_k(t)\}_{k=1\dots M_B}$  of the form (4.53). Indeed, one replaces  $\eta_p$  as a function of  $\{q_i\}$  from Eq. (4.98b) into Eq. (4.98a).

In practice, the fact that this model (4.53) is purely cubic is interesting for model reduction. Indeed, following the normal form approach of Sect. 4.4.4, no quadratic terms are present in the normal transform (4.69), implying  $A_{kkk}^k = B_{kkk}^k = 0$ , such that the normal form at cubic order, reduced to the  $k$ th CNM, in the form of Eq. (4.72), coincides exactly with the cubic oscillators (4.53) reduced to the  $k$ th CLM ( $q_j = 0, \forall j \neq k$ ), with only one cubic term of coefficient

$$\gamma_{kkk}^k = D_{kkk}^k - \sum_{p=1}^{M_B} \frac{G_{kk}^p C_{pk}^k}{\gamma_p^2}, \quad (4.99)$$

stemming from the static condensation described in the previous paragraph. The effect of the other CLMs ( $q_j(t)$  with  $j \neq k$ ), coupled through invariance breaking cubic terms in Eq. (4.53), are embedded in the cubic part of the normal transform. If one would expand the normal form at a higher order, one would replace Eq. (4.72) with an oscillator with additional quintic terms, of the form (see Touzé et al. (2004b)):

$$\ddot{r}_k^2 + \omega_k^2 r_k + \gamma_k^k r_k^3 + \Xi_k r_k^5 + \Upsilon_k r_k^3 \dot{r}_k^2 = 0, \quad r_j = 0, \quad \forall j \neq k \quad (4.100)$$

As a consequence, at cubic order, the normal form reduction is quasi-equivalent to a modal model reduced to a single CLM oscillator, which usually gives a very good reduced-order model, that can be completed by a few other CLM oscillators to increase accuracy. This has been successfully tested for straight beams and plates of various edge in Lazarus et al. (2012), Givois et al. (2019), Vizzaccaro et al. (2020) and for piezoelectric symmetric structures in Givois et al. (2021) (see also Sect. 4.6.5).

Figure 4.14b provides an illustration of the quality of a cubic modal model, with the backbone curve of the first bending CNM of a clamped-clamped beam. The result of Eq. (4.53) truncated to a single bending CLM model ( $q_1(t) \neq 0$  and also to a two bending CLMs model ( $(q_1(t), q_3(t)) \neq (0, 0)$ ) is compared to a high order complex normal form (CNF) and to a reference model with  $M = 20$  bending CLMs. It first shows that the single (cubic  $\Leftrightarrow$  third order) CLM model is valid up to a large amplitude of  $\simeq 0.4h$ , contrary to the cubic CNF that diverges at  $\simeq 0.2h$  and which needs an order 11 to compete. Then, the two CLMs model is able to capture the internal resonance tongue with an excellent accuracy, improving also the convergence of the main part of the backbone curve. The difference between CNF and ONF here is mainly due to the complexification of the normal form in the CNF, that approximates a single Duffing oscillator, whereas the ONF keeps it exact (see Grolet et al. (2024), de Figueiredo Stabile et al. (2024)).

Another example is the second resonance of a clamped-clamped beam, computed with Eq. (4.53) truncated to the first 10 CLMs and shown in Fig. 4.22a. As observed in Givois et al. (2019), there is virtually no difference in the backbone curve with this 10 mode computation and another one with Eq. (4.53) truncated to CLMs 2 and 4, the two modes involved in the internal resonance. In this case, the influence of the non-resonant cubic terms is thus negligible. The same results were obtained in Vizzaccaro et al. (2021b) for the convergence of the cubic order ONF for 3D finite-element discretised structures.

**Computation of coefficients** In practice, one has to compute the coefficients of the reduced-order model (4.53). In a finite-element context, the (brute) method consists in choosing a few master bending modes, to compute with the STEP (see Sect. 4.4.2) all quadratic and cubic coefficients ( $D_{ijl}^k, C_{pi}^k, G_{ij}^p$ ) associated to the master bending modes and a family of non-bending ones, as large as possible, and to compute the cubic coefficient  $\gamma_{ijl}^k$  of the master (bending only) model with relations analogous to Eq. (4.99) (in particular if  $i \neq j \neq k \neq l$ , see Givois et al. (2019)). It works in theory, but in practice, the truncation of the non-bending mode basis, in order to achieve convergence in (4.99), is always delicate and one often needs a lot since

the convergence is slow, especially for plate structures with a complex boundary (see Givois et al. (2019)). Moreover, in the case of 3D finite-elements, as addressed in Vizzaccaro et al. (2020), a surprising strong coupling appears with very high-frequency thickness modes (one of them is shown in Fig. 4.21), which makes this method unusable in practice.

To overcome this limitation, it is possible to directly compute the  $\gamma_{ijl}^k$  coefficients of (4.53) with any finite-element discretization in a non intrusive manner, using a modified version of the STEP (called M-STEP). In this case, one proceeds to the non-linear static computations of the STEP without prescribing the in-plane displacement field, thus relaxing the in-plane constraints, which is equivalent to statically condense the quadratic coupling with the non-bending modes (see Vizzaccaro et al. (2020) for all details).

Finally, the most rigorous method is to apply a normal form method directly to the finite-element discretised model (4.9), since the effect of all the quadratically coupled non-resonant modes is automatically embedded in one master normal coordinate. One can rely on the ONF (see Vizzaccaro et al. (2021b)), with a numerical method up to an order three normal form, or with a CNF (see Vizzaccaro et al. (2022)), with the advantage of dealing with an arbitrary order.

**Structures with inertia and curvature non-linearities** In the case of structures subjected to large rotations, because of loose in-plane motion restriction (see Fig. 4.12, right), a reduced-order model in bending must include the coupling with slave modes, which is in this case quadratic and *inertial*. This can be observed in the beam inextensible geometrically exact model (see the  $\ddot{u}$  term in Eqs. (4.37) and (4.36a) which states that  $u' \simeq -w^2/2$ ). This prevents a priori the use of a static condensation, even if some methods can include inertia (see Nicolaidou et al. (2021)).

Nevertheless, the normal form method is able to naturally capture the inertial effect of the slave modes, as shown in Vizzaccaro et al. (2022), Martin et al. (2023), Grolet et al. (2024) for cantilever beams, in Vizzaccaro et al. (2021b) for a turbomachinery blade and in Openi et al. (2021) for an electromechanical micro-mirror.

## 4.6.2 The Case of Curved/Non Symmetric Structures

In practice, the transverse symmetry of the bending vibrations is often broken (see Fig. 4.11, right), either because of an initially curved structure, because of stiffeners (see e.g. Legay and Combescure (2002)) or because of a non symmetric lamination, in the case of a composite material or a piezoelectric structure (see the softening behaviour of a mode of a NEMS laminated plate in Thomas et al. (2013)), to cite a few. In this case, the modal model naturally includes quadratic terms and the split between bending and non-bending motion of the previous section is not allowed anymore. This prevents applying the M-STEP method.

In the case of a not too strong asymmetry, it is still possible to use the brute method with a modal model (4.60) and try to artificially split the modal basis into



mainly bending and mainly axial modes, in order to reduce the dynamics on a few master “bending modes” and a number of slave “axial modes”, for the axial/bending coupling, but the convergence of the model is often slow (see an example on an asymmetric piezoelectric structure in Lazarus et al. (2012)).

Some authors promote the use of an implicit condensation method (ICE), that leads to neglect the inertia of *all* slave modes, except the one of a given (or a few) master modes. It was shown in Shen et al. (2021) that a *slow/fast* assumption must hold between slave and master coordinates for this assumption to be valid. Indeed, one must fulfill  $\omega_s > 6\omega_m$ , with  $(\omega_s, \omega_m)$  the natural frequencies of slave and master modes, respectively. For flat structures, this assumption is always fulfilled between the first bending modes and all the axial modes, thus justifying the success of the M-STEP method. On the contrary, with a transverse asymmetry, if one applies the ICE method to compute a single (bending) mode reduced-order model, the slow/fast assumption is not always fulfilled, especially with the other bending (slave) modes. Other methods, like modal derivatives and dual modes can also be used, see Touzé et al. (2021) for comparisons.

On the contrary, applying a normal form reduction leads to rigorously take into account all the non-resonant couplings with all slave modes in one operation. If the model is reduced to an ONF at order three, the dynamics is equivalent to a single Duffing oscillator (4.81), where the eventual softening effect of the slave modes, due to the transverse asymmetry, is naturally included in the value of the coefficient  $\Gamma_0$  (see Sects. 4.4.5 and 4.5.2). However, if the behaviour is softening at low amplitude ( $\Gamma_0 < 0$ ), it usually becomes hardening at high amplitude, in the form of Fig. 4.15. In this case, one needs a normal form of at least a fifth order, such that the quintic terms bring the hardening behaviour. The high order CNF naturally includes those effects (see an example in Vizzaccaro et al. (2022)).

### 4.6.3 Mechanism of Internal Resonances

This section addresses with more details the coupling mechanism that arise between two nonlinear modes involved in an internal resonance, and its associated reduced-order model. As an example, we consider here the particular case of a 1:3 internal resonance. It is observed when the free oscillation frequencies of two nonlinear modes are such that:

$$\omega_{n12} \simeq 3\omega_{n11}. \quad (4.101)$$

This can appear at very low amplitude if the above relationship is verified by the eigenfrequencies of the system, i.e.  $\omega_2 \simeq 3\omega_1$ . If not, the internal resonance can still appear at larger amplitude since the free oscillation frequencies of the nonlinear modes depend on the amplitude of the motion, because of the cubic nonlinear terms (see Eq. (4.77)).

This kind of internal resonance often appears in the vibration response of straight beam with axial/coupling nonlinearities. Examples are 1:3 internal res-

onances between the first and third bending modes of a hinged-hinged beam, shown in Fig. 4.14b, and between the second and fourth bending modes of a clamped-clamped beam, see Fig. 4.22a. Focusing on those two cases, the idea of this section is to thoroughly address how the coupling between the modes occurs, in term of the topology of the response curves, in relation with the reduced-order model.

**Reduced-order model** We consider the von Kármán model expanded on the CLM mode basis, Eq. (54), restricted to the two linear oscillators involved in the internal resonance, named  $(q_k(t), q_l(t))$ , that read:

$$\ddot{q}_k + 2\xi_k\omega_k\dot{q}_k + \omega_k^2 q_k + \Gamma_1 q_k^3 + \underline{C_1 q_k q_l^2} + \underline{C_2 q_k^2 q_l} + \Gamma_2 q_l^3 = F_1, \quad (4.102a)$$

$$\ddot{q}_l + 2\xi_l\omega_l\dot{q}_l + \omega_l^2 q_l + \underline{\Gamma_3 q_k^3} + C_3 q_k q_l^2 + \underline{C_4 q_k^2 q_l} + \underline{\Gamma_4 q_l^3} = 0. \quad (4.102b)$$

According to Sect. 4.4.4, the above equation includes *resonant terms due to the 1:3 internal resonance*, *trivially resonant terms*, the two others being non-resonant terms. The coefficients  $\Gamma_i$  and  $C_i$  are related to coefficients  $\gamma_{mnp}^r$ .

As analysed in Sect. 4.4.4, a correct normal form able to capture the internal resonance must include the two involved master modes. Then, as seen in Sect. 4.6.1, since no quadratic terms are present in the initial model (54), the normal form is exactly Eq. (4.102) without the two non-resonant terms, whose effect is very weak, except at large amplitude. In fact, in this particular case, it was observed that neglecting  $\Gamma_2$  and  $C_3$  leads to no difference in the response curves.

**Values of the coefficients** Coefficients  $(\Gamma_i, C_i)$  of Eq. (4.102) have the following values:

$$\Gamma_1 = \gamma_{kkk}^k, \quad \Gamma_2 = \gamma_{lll}^l, \quad \Gamma_3 = \gamma_{kkk}^l, \quad \Gamma_4 = \gamma_{lll}^k, \quad (4.103a)$$

$$C_1 = 3\Gamma_3, \quad C_2 = \gamma_{kkl}^k + \gamma_{klk}^k + \gamma_{kll}^k = C_3, \quad C_4 = 3\Gamma_2, \quad (4.103b)$$

where the relationships between the coefficients come from the existence of a potential energy (see Givois et al. (2019)). Coefficients  $\gamma_{mnp}^r$  are defined by Eq. (4.55).

Considering first the clamped-clamped boundary conditions and the 1:3 internal resonance of Fig. 4.22, between CNM2 and 4, numerical integrations show that the three necessary coefficients  $E_{22}$ ,  $E_{24}$  and  $E_{44}$  in Eq. (4.55) are non-zero. On the contrary, since the mode shapes of a hinged-hinged beam are simply sine functions,  $E_{24} = 0$  (whereas  $E_{22} \neq 0$  and  $E_{44} \neq 0$ ). This leads to  $C_2 = \Gamma_3 = 0$ , such that the two *resonant terms that drive the 1:3 internal resonance vanish* in the case of hinged-hinged boundary conditions.

**Degeneracy and resonant terms** The backbone curve of the conservative nonlinear modes (CNM) in this 1:3 internal resonance are computed as families of periodic orbits, by numerical continuation, as explained in Sect. 4.5.1. To this end, the two modal coordinates read:

$$q_k(t) = a_{1H_1} \cos \omega t + a_{1H_3} \cos 3\omega t + hh, \quad (4.104a)$$

$$q_l(t) = a_{2H_1} \cos \omega t + a_{2H_3} \cos 3\omega t + hh, \quad (4.104b)$$

since the motion onto a CNM is monophasic (see Sect. 4.5.2). The continuation algorithm enables computing the graphs  $(a_{iH_j}, \omega)$ .

We first consider the backbone curve of the clamped-clamped beam case of Fig. 4.22, detailed in Fig. 4.23a–c. The internally resonant modes are CNM2 and 4 ( $k = 2, l = 4$ ). In Fig. 4.23a, one observes that the backbone curve of CNM2 naturally starts at the natural frequency  $\omega = \omega_2 = \omega_l$  and that it is bent to the right because of a hardening behaviour. Then, the 1:3 internal resonance with CNM4 appears as a tongue of the branch, or offshoot, around  $\omega \simeq 1.1\omega_2$  (point A). In this area, the first (leading) harmonic  $a_{1H_1}$  of  $q_2(t)$  decreases, in favor of a transfer of energy toward the third harmonic  $a_{2H_3}$  of  $q_4(t)$  that increases, in the form of a super-harmonic resonance. This is qualitatively explained by remarking that the non-linearities create harmonics, and that the third one excites the second oscillator close to its resonance, this responding with a high amplitude on its third harmonic.

A particular feature is the connection of this branch, at point B where  $a_{1H_1} = 0$ , to the backbone of CNM4 (shown in dashed line), plotted as a function of  $\omega/3$ . A more correct view may be to look at this branch in 3D, as plotted in Fig. 4.23b, c. One can see that most of the backbone is contained in (or close to) the plane  $a_{2H_3} = 0$ , except in the area of the tongue, in which the branch emerges out of this plane to connect it with the plane  $a_{1H_1} = 0$  that contains the backbone curve of CNM4.

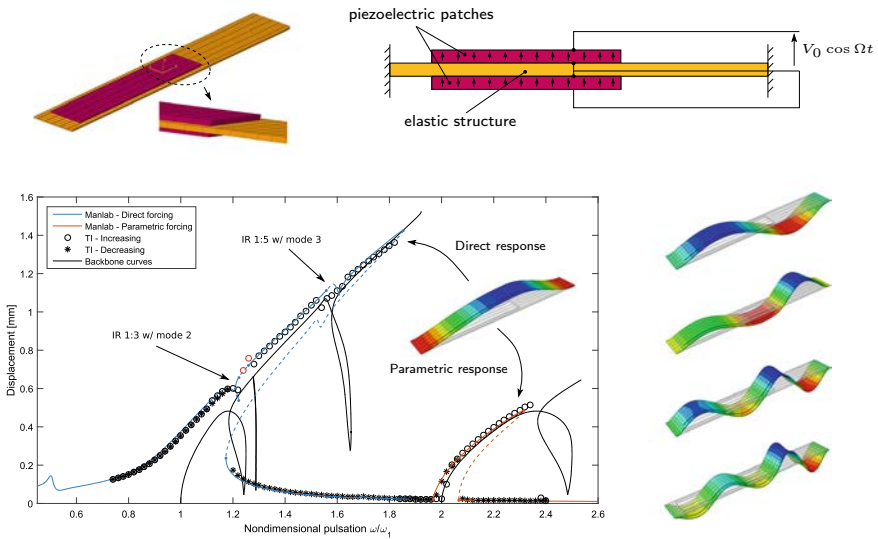
Now, considering the backbone curve of the hinged-hinged beam case of Fig. 4.14b, one observes that the two branches of the tongues are merged and that they emerge from the main part of the backbone through a bifurcation in A, without smooth turns. Indeed, Fig. 4.23d shows that the *full diagram is now composed of three branches*, connected at points A and B. This fact, already addressed in Lewandowski (1994, 1996), is revisited here in the light of resonant terms. Indeed, as seen above, the particularly simple mode shapes of the hinged-hinged beam lead to *the vanishing ( $C_2 = \Gamma_3 = 0$ ) of the two resonant terms responsible for the 1:3 internal resonance*. This explains the collapse of the two turns of the main branch into a single bifurcation point, from Fig. 4.23a–d. To illustrate the effect, Fig. 4.23d–f are similar to Fig. 4.23a–c, except that  $C_2$  and  $\Gamma_3$  are set to zero. More specifically, without these two resonant terms, the internal resonance still exist but becomes *degenerate*.

A cross-section of the invariant manifold associated to the CNM in internal resonance, in the space  $(q_2(t), \dot{q}_2(t), q_4(t))$ , is shown in Fig. 4.22b at various points of the backbone in Fig. 4.22a. Its tri-lobed shape is characteristic of the leading harmonics of the periodic orbit: H1 for  $q_2(t)$  and H3 for  $q_4(t)$  and its folding linked

to the internal resonance.

**Topology** In practice, according to the experience of the author, if the system has only cubic nonlinearities such as a transversely symmetric structure, multiple internal resonances of the type  $1:n$ , with  $n > 1$  an integer, can appear on the backbone curves of a given CNM. They can be classified in three types, as illustrated in Fig. 4.24. Type 1 is an odd internal resonances ( $1:n$  with  $n$  odd) in the form of the above described clamped-clamped beam  $1:3$  internal resonance. It shows a change of stability through two saddle node bifurcations, with vertical tangents in a frequency-energy plot (see examples in Givois et al. (2019)). Type 2 is also an odd internal resonance, but degenerate, because the associated resonant terms are absent of the normal form, as in the first backbone curve of the hinged-hinged beam considered above. Then, type 3 is an even internal resonance ( $1:n$  with  $n$  even), for which the tongue emerge from the main branch through symmetry breaking bifurcations. It can also appear that the two emerging branches are not connected to each other. Various examples can be found in Guillot et al. (2020) and reference therein. Two type 1 resonances are also visible in Fig. 4.26.

In the case of  $n > 3$ , such as a  $1:5$ ,  $1:7$  internal resonance, the corresponding resonant terms would appear in an order  $n$  normal form. In this case, the coefficients of the order  $n$  resonant monomials are created by the canceling of the non-resonant



**Fig. 4.26** Frequency response of an elastic plate driven in vibration by two piezoelectric patches. (top) Sketches of the simulated structure and the finite-element mesh. (bottom) comparison between a stepped-sine computation with brute time integrations in Abaqus ('o': increasing; '\*': decreasing) and the result of a 5 CLMs reduced-order model (the corresponding five bending mode shapes are shown) computed by numerical continuation. The direct and parametric resonances of the first bending mode are shown, along with the associated backbone curve (from Givois et al. (2021))

terms of order  $n - 1$ , and thus of coefficients cubic coefficients  $\gamma_{mnp}^r$ . This explains how cubic terms can create order  $n > 3$  resonant terms.

#### 4.6.4 *Non-resonant Terms and a 1:2 Internal Resonance*

In this section, we consider the case of a 1:2 internal resonance, intentionally caused by tuning two natural frequencies of the system such that  $\omega_2 \simeq 2\omega_1$ . This is realised in practice by coupling the deformation of an elastic structure, with a targeted natural frequency  $\omega_2$ , to a resonant and nonlinear electronic circuit of natural frequency  $\omega_1$ , thanks to a piezoelectric transducer. The main goal is to use the internal resonance to transfer the energy from the mechanical mode to the electronic circuit in order to damp the mechanical vibrations. All details are provided in the series of articles: Shami et al. (2022a, c) for theory and Shami et al. (2022b, 2023b) for the experimental proof of concept.

To achieve this goal, a quadratic nonlinearity is created in the electronic circuit. The particular (and well known, see i.e. Nayfeh and Mook (1979)) topology of the vibratory response is shown in Fig. 4.25a, d: in the vicinity of the driving frequency  $\omega \simeq \omega_2 \simeq 2\omega_1$ , a nonlinear antiresonance is created, associated to a saturation of the amplitude of the mechanical mode, through a sub-harmonic energy transfer to the electrical mode.

However, the nonlinearity in the electronic circuits, in addition to the two resonant quadratic terms underlined in Eq. (4.64), is also responsible for all the other non-resonant terms of Eq. (4.64). If their effect is often negligible, as seen in Sect. 4.4 or Sect. 4.6.3, in the present case, the value of their coefficients is large, leading to a noticeable detuning of the antiresonance. This effect is well explained by the normal form (4.74). Indeed, the quadratic non-resonant terms create cubic terms in the normal form (of coefficients  $A_{ijl}^k, B_{ijl}^k \dots$ ) responsible for a softening effect, visible in Fig. 4.25b, e.

Finally, adding cubic nonlinearities in the electronic circuit naturally adds coefficients  $\gamma_{ijl}^k$  in create coefficients the normal form (4.74), that can be tuned to cancel the effect of the quadratic resonant terms, thus recovering the symmetry of the resonance curves, as shown in Fig. 4.25c, f. This operation is made possible thanks to an analytical relationship between quadratic and cubic nonlinearities of the electronic circuit, obtained through the normal form.

#### 4.6.5 *Piezoelectric Structures Nonlinear Dynamics*

The final example of this chapter is a reduced-order model of a transversely symmetric structures, in the form of a flat plate that includes collocated piezoelectric elements on both sides. The reduced-order model is obtained by exactly condensing the in-plane modes thanks to the M-STEP method briefly addressed in Sect. 4.6.1, that was

extended in to compute also the coupling coefficients  $\chi_k$  and  $\theta_{ij}$  in Eq. (4.62). All details are provided in Givois et al. (2021).

The reduced-order model has the form of Eq. (4.62), reduced to the first 5 bending modes. For the reasons addressed in Sect. 4.6.1, and in particular the absence of quadratic terms because of the transverse symmetry, the quality of the modal reduced-order model is excellent, in comparison to a reference simulation in Abaqus. Anecdotally, the computation time gain is huge: several days are necessary for the Abaqus computation, whereas a few minutes are necessary for the computation of the whole branch with the Manlab continuation software (Guillot et al. 2018).

Interestingly, a parametric resonance, analogous to the one of a simple pendulum of Fig. 4.5, is obtained. In fact, driving the piezoelectric patches with a harmonic voltage signal results in a periodic creation of in-plane stresses since the patches alternatively stretch and contract. The resulting modulation of the in-plane stresses modulate the bending stiffness and thus the natural frequencies of the system, creating a parametric driving. This effect was also studied in Lazarus et al. (2012) and sometimes used to artificially change the quality factor of a resonator (Thomas et al. 2013).

## 4.7 Conclusion

Despite the condensed material presented in the present chapter, the leading idea was to show how the normal form can help reducing the size of a model, but also how it enables to understand the particular features of a particular nonlinear dynamics. All important features of modern practices in structural nonlinear dynamics were addressed: models, nonlinear phenomena, numerical computations and experimental identifications. The particular case of mechanical structures subjected to geometrical non-linearities was considered as it naturally creates interesting and varied nonlinear dynamics. The question of internal resonances was particularly considered. The influence of possible symmetries of the system was also particularly addressed. Finally, the two sides (numerical and experimental) of continuation method as a fundamental tool to accurately compute and experimentally identify a nonlinear system were also presented.

Normal form appears as a fantastic and currently well mastered tool for nonlinear dynamics analysis and model-reduction. However, a lot of questions remain open or incompletely understood: non-smooth non-linearities, material non-linearities in electromechanically coupled systems (piezoelectric, electrostatic, electromagnetic...), damped nonlinear modes...

**Acknowledgements** The author would like to thank all the colleagues and students for their joint work and uncountable discussions, without which the material of this chapter would not exist: C. Touzé, J.-F. Deü, B. Cochelin, A. Grolet, C. Giraud-Audine, A. Lazarus, V. Denis, C. Camier, M. Jossic, M. Colin, A. Sénéchal, É. Cottanceau, A. Givois, M. Debeurre, Z. Shami, H. Fayolle, M. Monteil and more recently A. Vizzaccaro, K. Dekemele, R. Leine and F. Bayer. A. Chaigne, who

initiated this work 27 years ago, is also warmly thanked. A special and warm thought goes out for S. Benacchio†, who left us far too soon.

## References

- Abaqus. (2024). Simulia user assistance 2024. [https://help.3ds.com/2024/English/DSSIMULIA\\_Established/SIMACAEGSARefMap/simagsa-m-NlnSourcenonlin-sb.htm](https://help.3ds.com/2024/English/DSSIMULIA_Established/SIMACAEGSARefMap/simagsa-m-NlnSourcenonlin-sb.htm). Accessed April 2024.
- Abeoos, G., Müller, F., Ferhatoglu, E., Scheel, M., Collette, C., Kerschen, G., Brake, M. R. W., Tiso, P., Renson, L., & Krack, M. (2022). A consistency analysis of phase-locked-loop testing and control-based continuation for a geometrically nonlinear frictional system. *Mechanical Systems and Signal Processing*, *170*, 108820.
- Acary, V., & Brogliato, B. (2008). *Numerical methods for nonsmooth dynamical systems*. Springer.
- Amabili, M. (2008). *Nonlinear vibrations and stability of shells and plates*. Cambridge University Press.
- Amandolèse, X., Gabillet, C., & Watine, Y. (2024). Adaptation of the facchinetti, de langre and biolley model for the hydroelastic vortex-induced vibrations of a cantilevered flat plate. *Journal of Fluids and Structures*, *124*, 104017.
- Antman, S. S. (1974). Kirchhoff's problem for nonlinearly elastic rods. *Quarterly of Applied Mathematics*, *32*, 221–240.
- Arquier, R., Bellizzi, S., Bouc, R., & Cochelin, B. (2006). Two methods for the computation of nonlinear modes of vibrating systems at large amplitude. *Computers & Structures*, *84*, 1565–1576.
- Aster. (1989–2024). Finite element *code\_aster*, Analysis of Structures and Thermomechanics for Studies and Research. Open source at [www.code-aster.org](http://www.code-aster.org)
- Audoly, B., & Pomeau, Y. (2010). *Elasticity and geometry*. Oxford University Press.
- Bagheri, A. K., Sonnevile, V., & Renson, L. (2024). Nonlinear normal modes of highly flexible beam structures modelled under the  $se(3)$  lie group framework. *Nonlinear Dynamics*, *112*, 1641–1659.
- Balmès, É. (1996). Parametric families of reduced finite element models. Theory and applications. *Mechanical Systems and Signal Processing*, *10*(4), 381–394.
- Barton, D. W., & Burrow, S. G. (2011). Numerical continuation in a physical experiment: Investigation of a nonlinear energy harvester. *Journal of Computational and Nonlinear Dynamics*, *11*(10), 11010.
- Bauchau, O., & Sonnevile, V. (2021). Formulation of shell elements based on the motion formalism. *Applied Mechanics*, *2*, 1009–1036.
- Bauchau, O. A. (2011). *Flexible multibody dynamics*. Springer.
- Bayer, F., & Leine, R. I. (2024). Sorting-free hill-based stability analysis of periodic solutions through Koopman analysis. *Nonlinear Dynamics*, *111*(9), 8439–8466.
- Bayer, F., Leine, R. I., Thomas, O., & Grolet, A. (2024). Koopman-hill stability computation of periodic orbits in polynomial dynamical systems using a real-valued quadratic harmonic balance formulation. *International Journal of Non-linear Mechanics*. Under review.
- Bažant, Z., & Cedolin, L. (2010). *Stability of structures*. World Scientific.
- Blahoš, J., Vizzaccaro, A., Salles, L., & El Haddad, F. (2020). Parallel harmonic balance method for analysis of nonlinear dynamical systems. In *Proceedings of ASME Turbo Expo 2020, Turbo-machinery Technical Conference and Exposition, GT2020*.
- Bottom, V. A. (1982). *Introduction to quartz crystal unit design*. Van Nostrand Reinhold.
- Bryant, P., & Miles, J. W. (1990). On a periodically forced, weakly damped pendulum. Part 1: Applied torque. *The Journal of the Australian Mathematical Society Series B*, *32*, 1–22.

- Bureau, E., Schilder, F., Elmegård, M., Santos, I. F., Thomsen, J. J., & Starke, J. (2014). Experimental bifurcation analysis of an impact oscillator - determining stability. *Journal of Sound and Vibration*, 333, 5464–5474.
- Cadot, O., Ducceschi, M., Humbert, T., Miquel, B., Mordant, N., Josserand, C., & Touzé, C. (2016). Wave turbulence in vibrating plate. In C. Skiadas (Ed.), *Handbook of applications of Chaos theory*. Chapman and Hall/CRC.
- Camier, C., Touzé, C., & Thomas, O. (2009). Non-linear vibrations of imperfect free-edge circular plates and shells. *European Journal of Mechanics - A/Solids*, 28(3), 500–515. <https://doi.org/10.1016/j.euromechsol.2008.11.005>
- Chaigne, A., & Lambourg, C. (2001). Time-domain simulation of damped impacted plates. *Journal of the Acoustical Society of America*, 109(4), 1422–1432.
- Chaigne, A., Touzé, C., & Thomas, O. (2005). Nonlinear vibrations and chaos in gongs and cymbals. *Acoustical Science and Technology*, 26(5), 403–409. <https://doi.org/10.1250/ast.26.403>
- Chapelle, D., & Bathe, K. J. (2011). *The finite element analysis of shells - fundamentals* (2nd ed.). Springer.
- Chouvion, B., McWilliam, S., Popov, A. A., & Fox, C. H. J. (2012). Review and comparison of different support loss models for micro-electro-mechanical systems resonators undergoing in-plane vibration. *Proceedings of the Institution of Mechanical Engineers, Part C: Journal of Mechanical Engineering Science*, 226(1), 283–295.
- Ciarlet, P. G. (1980). A justification of the von-Kármán equations. *The Archive for Rational Mechanics and Analysis*, 73, 349–389.
- Cochelin, B., & Medale, M. (2013). Power series analysis as a major breakthrough to improve the efficiency of asymptotic numerical method in the vicinity of bifurcations. *Journal of Computational Physics*, 236, 594–607.
- Cochelin, B., & Vergez, C. (2009). A high order purely frequential harmonic balance formulation. *Journal of Sound and Vibration*, 324(1–2), 243–262.
- Colin, M., Thomas, O., Grondel, S., & Cattan, É. (2020). Very large amplitude vibrations of flexible structures: Experimental identification and validation of a quadratic drag damping model. *Journal of Fluids and Structures*, 97, 103056. <https://doi.org/10.1016/j.jfluidstructs.2020.103056>
- Corigliano, A., Ardito, R., Comi, C., Frangi, A., Ghisi, A., & Mariani, S. (2018). *Mechanics of microsystems*. Wiley.
- Cottanceau, É., Thomas, O., Véron, P., Alochét, M., & Deligny, R. (2017). A finite element/quaternion/asymptotic numerical method for the 3D simulation of flexible cables. *Finite Elements in Analysis and Design*, 139, 14–34. <https://doi.org/10.1016/j.finel.2017.10.002>
- Crespo da Silva, M. R. M., & Glynn, C. C. (1978a). Nonlinear flexural-flexural-torsional dynamics of inextensional beams. Part 1: Equations of motion. *Journal of Structural Engineering*, 6(4), 437–448.
- Crespo da Silva, M. R. M., & Glynn, C. C. (1978b). Nonlinear flexural-flexural-torsional dynamics of inextensional beams. Part 2: Forced motions. *Journal of Structural Engineering*, 6(4), 449–461.
- Crisfield, M. A. (1981). A fast incremental/iteration solution procedure that handles “snap-through”. *Computers and Structures*, 13, 55–62.
- Cusumano, J. P., & Moon, F. C. (1995). Chaotic non-planar vibrations of the thin elastica, Part 1: Experimental observation of planar instability. *Journal of Sound and Vibration*, 179(2), 185–208.
- Dankowicz, H., & Schilder, F. (2013). *Recipes for continuation*. SIAM.
- de Figueiredo Stabile, A., Touzé, C., & Vizzaccaro, A. (2024). Normal form analysis of nonlinear oscillator equations with automated arbitrary order expansions. *Journal of Theoretical, Computational and Applied Mechanics*. Under review.
- de la Llave, R., & Kogelbauer, F. (2019). Global persistence of Lyapunov subcenter manifolds as spectral submanifolds under dissipative perturbations. *SIAM Journal of Applied Dynamical Systems*, 18(4), 2099–2142.
- Debeurre, M., Grolet, A., Cochelin, B., & Thomas, O. (2023). Finite element computation of nonlinear modes and frequency response of geometrically exact beam structures. *Journal of Sound and Vibration*, 548, 117534. <https://doi.org/10.1016/j.jsv.2022.117534>



- Debeurre, M., Grolet, A., & Thomas, O. (2023). Extreme nonlinear dynamics of cantilever beams: Effect of gravity and slenderness on the nonlinear modes. *Nonlinear Dynamics*, *111*, 12787–12815. <https://doi.org/10.1007/s11071-023-08637-x>
- Debeurre, M., Benacchio, S., Grolet, A., Grenat, C., Giraud-Audine, C., & Thomas, O. (2024). Phase resonance testing of highly flexible structures: Measurement of conservative nonlinear modes and nonlinear damping identification. *Mechanical Systems and Signal Processing*, *215*, 111423. <https://doi.org/10.1016/j.ymsp.2024.111423>
- Debeurre, M., Grolet, A., & Thomas, O. (2024). Quaternion-based finite element computation of nonlinear modes and frequency responses of geometrically exact beam structures in three dimensions. *Multibody System Dynamics*. Accepted for publication.
- Denis, V., Jossic, M., Giraud-Audine, C., Chomette, B., Renault, A., & Thomas, O. (2018). Identification of nonlinear modes using phase-locked-loop experimental continuation and normal form. *Mechanical Systems and Signal Processing*, *106*, 430–452. <https://doi.org/10.1016/j.ymsp.2018.01.014>
- Dhooge, A., Govaerts, W., & Kuznetsov, Y. A. (2003). Matcont: A matlab package for numerical bifurcation analysis of odes. *ACM Transactions on Mathematical Software*, *29*(2), 141–164.
- Doedel, E. J., Paffenroth, R., Champneys, A. R., Fairgrieve, T. F., Kuznetsov, Y. A., Oldeman, B. E., Sandstede, B., & Wang, X. (2002). Auto 2000: Continuation and bifurcation software for ordinary differential equations.
- Ducarne, J., Thomas, O., & Deü, J.-F. (2012). Placement and dimension optimization of shunted piezoelectric patches for vibration reduction. *Journal of Sound and Vibration*, *331*(14), 3286–3303. <https://doi.org/10.1016/j.jsv.2012.03.002>
- Ducceschi, M., & Touzé, C. (2015). Modal approach for nonlinear vibrations of damped impacted plates: Application to sound synthesis of gongs and cymbals. *Journal of Sound and Vibration*, *344*, 313–331.
- Dulac, H. (1912). Solutions d'un système d'équations différentielles dans le voisinage de valeurs singulières. *Bulletin de la Société Mathématique de France*, *42*, 324–383. [http://www.numdam.org/item?id=BSMF\\_1912\\_\\_40\\_\\_324\\_0](http://www.numdam.org/item?id=BSMF_1912__40__324_0)
- Eringen, A. C. (1952). On the non-linear vibration of elastic bars. *Quarterly of Applied Mathematics*, *9*, 361–369.
- Ewins, D. J. (2000). *Modal testing: Theory, practice and application*. Research Studies Press Ltd.
- Farokhi, H., Xia, Y., & Erturk, A. (2022). Experimentally validated geometrically exact model for extreme nonlinear motions of cantilevers. *Nonlinear Dynamics*, *107*, 457–475.
- Frangi, A., Opreni, A., Boni, N., Fedeli, P., Carminati, R., Merli, M., & Mendicino, G. (2020). Nonlinear response of PZT-actuated resonant micromirrors. *Journal of Microelectromechanical Systems*, *29*(6), 1421–1430.
- Gallerand, L., Legrand, M., Panneton, R., Leclaire, P., & Dupont, T. (2024). Added nonlinear damping of homogenized fluid-saturated microperforated plates in Forchheimer flow regime. *Journal of Sound and Vibration*. Submitted.
- Gérardin, M., & Cardona, A. (2001). *Flexible multibody dynamics*. Wiley.
- Gérardin, M., & Rixen, D. J. (2015). *Mechanical vibrations: Theory and application to structural dynamics* (3rd ed.). Wiley.
- Gerstmayr, J., Matikainen, M. K., & Mikkola, A. M. (2008). A geometrically exact beam element based on the absolute nodal coordinate formulation. *Multibody System Dynamics*, *20*(359).
- Giclais, S., Lubrina, P., & Stephan, C. (2016). Aircraft ground vibration testing at ONERA. *Aerospace Lab Journal*, *12*, AL12–15. <https://doi.org/10.12762/2016.AL12-05>
- Givois, A., Grolet, A., Thomas, O., & Deü, J.-F. (2019). On the frequency response computation of geometrically nonlinear flat structures using reduced-order finite element models. *Nonlinear Dynamics*, *97*(2), 1147–1781. <https://doi.org/10.1007/s11071-019-05021-6>
- Givois, A., Giraud-Audine, C., Deü, J.-F., & Thomas, O. (2020). Experimental analysis of nonlinear resonances in piezoelectric plates with geometric nonlinearities. *Nonlinear Dynamics*, *102*, 1451–1462. <https://doi.org/10.1007/s11071-020-05997-6>

- Givois, A., Tan, J.-J., Touzé, C., & Thomas, O. (2020). Backbone curves of coupled cubic oscillators in one-to-one internal resonance: Bifurcation scenario, measurements and parameter identification. *Meccanica*, 55, 581–503. <https://doi.org/10.1007/s11012-020-01132-2>
- Givois, A., Deü, J.-F., & Thomas, O. (2021). Dynamics of piezoelectric structures with geometric nonlinearities: A non-intrusive reduced order modelling strategy. *Computers & Structures*, 253, 106575. <https://doi.org/10.1016/j.compstruc.2021.106575>
- Gottlieb, H. P. W. (1975). Acoustical radiation damping of vibrating solids. *Journal of Sound and Vibration*, 40(4), 521–533.
- Grenat, C., Baguet, S., Lamarque, C.-H., & Dufour, R. (2019). A multi-parametric recursive continuation method for nonlinear dynamical systems. *Mechanical Systems and Signal Processing*, 127, 276–289.
- Grolet, A., Vizzaccaro, A., Debeurre, M., & Thomas, O. (2024). High order invariant manifold model reduction for systems with non-polynomial non-linearities: Geometrically exact finite element structures and validity limit. *Nonlinear Dynamics*. Under review
- Guillot, L., Vigué, P., Vergez, C., & Cochelin, B. (2017). Continuation of quasi-periodic solutions with two-frequency harmonic balance method. *Journal of Sound and Vibration*, 394, 434–450.
- Guillot, L., Lazarus, A., Thomas, O., Vergez, C., & Cochelin, B. (2018). Manlab 4.0: An interactive path-following and bifurcation analysis software.
- Guillot, L., Cochelin, B., & Vergez, C. (2019). A Taylor series-based continuation method for solutions of dynamical systems. *Nonlinear Dynamics*, 98, 2827–2845.
- Guillot, L., Lazarus, A., Thomas, O., Vergez, C., & Cochelin, B. (2020). A purely frequency based floquet-hill formulation for the efficient stability computation of periodic solutions of ordinary differential systems. *Journal of Computational Physics*, 416, 109477. <https://doi.org/10.1016/j.jcp.2020.109477>
- Hairer, E., Nørsett, S. P., & Wanner, G. (2008). *Solving ordinary differential equations (Part I and II)*. Springer.
- Holzappel, G. A. (2000). *Nonlinear solid mechanics*. Wiley.
- Ikeda, T. (1990). *Fundamentals of piezoelectricity*. Oxford University Press.
- Johnk, C. T. A. (1988). *Engineering electromagnetic fields and waves* (2nd ed.). Wiley.
- Johnson, K. L. (1985). *Contact mechanics*. Cambridge University Press.
- Jossic, M., Chomette, B., Denis, V., Thomas, O., Mamou-Mani, A., & Roze, D. (2018). Effects of internal resonances in the pitch glide of Chinese gongs. *The Journal of the Acoustical Society of America*, 144(1), 431–442. <https://doi.org/10.1121/1.5038114>
- Karkar, S., Cochelin, B., & Vergez, C. (2014). A comparative study of the harmonic balance method and the orthogonal collocation method on stiff nonlinear systems. *Journal of Sound and Vibration*, 333, 2554–2567.
- Kelley, A. (1967). On the Liapunov subcenter manifold. *Journal of Mathematical Analysis and Applications*, 18, 472–478.
- Kerschen, G., Peeters, M., Golinval, J. C., & Vakakis, A. F. (2009). Nonlinear normal modes, part I: A useful framework for the structural dynamicist. *Mechanical Systems and Signal Processing*, 23(1), 170–194.
- Krack, M. (2015). Nonlinear modal analysis of nonconservative systems: Extension of the periodic motion concept. *Computers and Structures*, 154, 59–71.
- Krack, M., & Gross, J. (2019). *Harmonic balance for nonlinear vibration problems*. Springer.
- Krauskopf, B., Osinga, H. M., & Galán-Vioque, J. (eds.). (2007). *Numerical continuation methods for dynamical systems*. Springer.
- Lacarbonara, W., & Yabuno, H. (2006). Refined models of elastic beams undergoing large in-plane motions: Theory and experiment. *International Journal of Solids and Structures*, 43, 5066–5084.
- Lacarbonara, W., Bernardini, D., & Vestroni, F. (2004). Nonlinear thermomechanical oscillations of shape-memory devices. *International Journal of Solids and Structures*, 41, 1209–1234.
- Lamarque, C.-H., Touzé, C., & Thomas, O. (2012). An upper bound for validity limits of asymptotic analytical approaches based on normal form theory. *Nonlinear Dynamics*, 70(3), 1931–1949. <https://doi.org/10.1007/s11071-012-0584-y>

- Lang, H., Linn, J., & Arnold, M. (2011). Multi-body dynamics simulation of geometrically exact Cosserat rods. *Multibody System Dynamics*, 25, 285–312.
- Laxalde, D., & Thouverez, F. (2009). Complex non-linear modal analysis for mechanical systems application to turbomachinery bladings with friction interfaces. *Journal of Sound and Vibration*, 322(4–5), 1009–1025.
- Lazarus, A., & Thomas, O. (2010). A harmonic-based method for computing the stability of periodic solutions of dynamical systems. *Comptes Rendus Micanique*, 338(9), 510–517. <https://doi.org/10.1016/j.crme.2010.07.020>
- Lazarus, A., Thomas, O., & Deü, J.-F. (2012). Finite elements reduced order models for nonlinear vibrations of piezoelectric layered beams with applications to NEMS. *Finite Elements in Analysis and Design*, 49(1), 35–51. <https://doi.org/10.1016/j.finel.2011.08.019>
- Lazarus, A., Miller, J. T., & Reis, P. M. (2013). Continuation of equilibria and stability of slender elastic rods using an asymptotic numerical method. *Journal of the Mechanics and Physics of Solids*, 61(8), 1712–1736.
- Leadenham, S., & Erturk, A. (2015). Unified nonlinear electroelastic dynamics of a bimorph piezoelectric cantilever for energy harvesting, sensing, and actuation. *Nonlinear Dynamics*, 79, 1727–1743.
- Legay, A., & Combescure, A. (2002). Efficient algorithms for parametric non-linear instability analysis. *International Journal of Non-linear Mechanics*, 37(4–5), 709–722.
- Leine, R. I., & Nijmeijer, H. (2004). *Dynamics and bifurcations of non-smooth mechanical systems*. Springer.
- Lewandowski, R. (1994). Solutions with bifurcation points for free vibration of beams: An analytical approach. *Journal of Sound and Vibration*, 177(2), 239–249.
- Lewandowski, R. (1996). On beams, membranes and plates vibration backbone curves in cases of internal resonance. *Meccanica*, 31, 323–346.
- Linn, J., Lang, H., & Tuganov, A. (2013). Geometrically exact Cosserat rods with Kelvin-Voigt type viscous damping. *Mechanical Sciences*, 4, 79–96.
- Lyapunov, A. (1907). Problème général de la stabilité du mouvement. *Annales de la faculté des sciences de Toulouse*, 9(2), 203–474.
- Marconi, J., Tiso, P., Quadrelli, D. E., & Braghin, F. (2021). A higher-order parametric nonlinear reduced-order model for imperfect structures using Neumann expansion. *Nonlinear Dynamics*, 104, 3039–3063.
- Martin, A., Opreni, A., Vizzaccaro, A., Debeurre, M., Salles, L., Frangi, A., Thomas, O., & Touzé, C. (2023). Reduced order modeling of geometrically nonlinear rotating structures using the direct parametrisation of invariant manifolds. *Journal of Theoretical, Computational and Applied Mechanics*. <https://doi.org/10.46298/jtcam.10430>
- Matlab. (2017). Matlab version: 9.3.0 (r2017b). <https://www.mathworks.com>
- Maugin, G. A. (1988). *Continuum mechanics of electromagnetic solids*. North-Holland.
- McConnell, K. G., & Varoto, P. S. (2008). *Vibration testing: Theory and practice* (2nd ed.). Wiley.
- Meier, C., Popp, A., & Wall, W. A. (2019). Geometrically exact finite element formulations for slender beams: Kirchhoff-love theory versus Simo-Reissner theory. *Archives of Computational Methods in Engineering*, 26, 163–243.
- Meirovitch, L. (1967). *Analytical methods in vibrations*. Macmillian Publishing Co.
- Mettler, E. (1951). Zum problem der stabilität erzwungener schwingungen elastischer körper. *Zeitschrift für Angewandte Mathematik und Mechanik (ZAMM)*, 31(8–9), 263–264.
- Millet, O., Hamdouni, A., & Cimetière, A. (2001). A classification of thin plate models by asymptotic expansion of non-linear three-dimensional equilibrium equations. *The International Journal of Non-linear Mechanics*, 36, 165–186.
- Monteil, M., Thomas, O., & Touzé, C. (2015). Identification of mode couplings in nonlinear vibrations of the steelpan. *Applied Acoustics*, 89, 1–15. <https://doi.org/10.1016/j.apacoust.2014.08.008>
- Morin, B., Legay, A., & Deü, J.-F. (2018). Reduced order models for dynamic behavior of elastomer damping devices. *Finite Elements in Analysis and Design*, 143, 66–75.

- Müller, F., Woiwode, L., Gross, J., Scheel, M., & Krack, M. (2022). Nonlinear damping quantification from phase-resonant tests under base excitation. *Mechanical Systems and Signal Processing*, *177*, 109170.
- Muravyov, A. A., & Rizzi, S. A. (2003). Determination of nonlinear stiffness with application to random vibration of geometrically nonlinear structures. *Computers & Structures*, *81*(15), 1513–1523.
- Nayfeh, A. H., & Balachandran, B. (1995). *Applied nonlinear dynamics. analytical, computational and experimental methods*. Wiley.
- Nayfeh, A. H., & Mook, D. T. (1979). *Nonlinear oscillations*. New-York: Wiley.
- Neukirch, S., Yavari, M., Challamel, N., & Thomas, O. (2021). Comparison of the von Kármán and Kirchhoff models for the post-buckling and vibrations of elastic beams. *Journal of Theoretical, Computational and Applied Mechanics*. <https://doi.org/10.46298/jtcam.6828>
- Nicolaidou, E., Hill, T. L., & Neild, S. A. (2021). Indirect reduced-order modelling: Using nonlinear manifolds to conserve kinetic energy. *Proceedings of the Royal Society A*, *476*, 20200589.
- Ogden, R. W. (1997). *Non-linear elastic deformations*. Dover.
- Opreni, A., Vizzaccaro, A., Frangi, A., & Touzé, C. (2021). Model order reduction based on direct normal form: Application to large finite element mems structures featuring internal resonance. *Nonlinear Dynamics*, *105*, 1237–1272.
- Opreni, A., Vizzaccaro, A., Touzé, C., & Frangi, A. (2023). High-order direct parametrisation of invariant manifolds for model order reduction of finite element structures: Application to generic forcing terms and parametrically excited systems. *Nonlinear Dynamics*, *111*, 5401–5447.
- Païdoussis, M. P., Price, S. J., & de Langre, E. (2011). *Fluid-structure interactions*. Cambridge University Press.
- Peeters, M., Viguier, R., Sïrandour, G., Kerschen, G., & Golinval, J. C. (2009). Nonlinear normal modes, part II: Toward a practical computation using numerical continuation techniques. *Mechanical Systems and Signal Processing*, *23*(1), 170–194.
- Peeters, M., Kerschen, G., & Golinval, J. C. (2011). Dynamic testing of nonlinear vibrating structures using nonlinear normal modes. *Journal of Sound and Vibration*, *330*, 486–509.
- Peletan, L., Baguet, S., Torkhani, M., & Jacquet-Richardet, G. (2013). A comparison of stability computational methods for periodic solution of nonlinear problems with application to rotordynamics. *Nonlinear Dynamics*, *72*(3), 671–682.
- Peter, S., & Leine, R. I. (2017). Excitation power quantities in phase resonance testing of nonlinear systems with phase-locked-loop excitation. *Mechanical Systems and Signal Processing*, *96*, 139–158.
- Peter, S., Schreyer, F., & Leine, R. I. (2019). A method for numerical and experimental nonlinear modal analysis of nonsmooth systems. *Mechanical Systems and Signal Processing*, *120*, 193–807.
- Poincaré, H. (1982). *Les méthodes nouvelles de la mécanique céleste*. Paris: Gauthiers-Villars.
- Porter, J. H., & Brake, M. R. W. (2024). Tracking superharmonic resonances for nonlinear vibration of conservative and hysteretic single degree of freedom systems. *Mechanical Systems and Signal Processing*, *215*, 111410.
- Preumont, A. (2011). *Vibration control of active structures* (3rd ed.). Springer.
- Reissner, E. (1972). On one-dimensional finite strain beam theory: The plane problem. *Zeitschrift für Angewandte Mathematik und Physik*, *23*(5), 795–804.
- Renson, L., Gonzalez-Buelga, A., Barton, D. A. W., & Neild, S. A. (2016). Robust identification of backbone curves using control-based continuation. *Journal of Sound and Vibration*, *367*, 145–158. <https://doi.org/10.1016/j.jsv.2015.12.035>
- Rosenberg, R. M. (1962). The normal mode of n-degree-of-freedom systems. *Journal of Applied Mechanics*, *33*(4), 877–880.
- Rouleau, L., Deü, J.-F., & Legay, A. (2017). A comparison of model reduction techniques based on modal projection for structures with frequency-dependent damping. *Mechanical Systems and Signal Processing*, *90*, 110–125.
- Salençon, J. (2001). *Handbook of continuum mechanics*. Springer.

- Sanders, J. A., Verhulst, F., & Murdock, J. (2007). *Averaging methods in nonlinear dynamical systems* (2nd ed.). Springer.
- Scheel, M., Peter, S., Leine, R. I., & Krack, M. (2018). A phase resonance approach for modal testing of structures with nonlinear dissipation. *Journal of Sound and Vibration*, *435*, 56–73.
- Seydel, R. (2010). *Practical bifurcation and stability analysis* (3rd ed.). Springer.
- Schwarz, S., Kohlmann, L., Hartung, A., Gross, J., Scheel, M., & Krack, M. (2020). Validation of a turbine blade component test with frictional contacts by phase-locked-loop and force-controlled measurements. *Journal of Engineering for Gas Turbines and Power*, *142*, 051006.
- Shami, Z. A., Giraud-Audine, C., & Thomas, O. (2022). A nonlinear piezoelectric shunt absorber with a 2:1 internal resonance: Theory. *Mechanical Systems and Signal Processing*, *170*, 108768. <https://doi.org/10.1016/j.ymssp.2021.108768>
- Shami, Z. A., Giraud-Audine, C., & Thomas, O. (2022). A nonlinear piezoelectric shunt absorber with 2:1 internal resonance: Experimental proof of concept. *Smart Materials and Structures*, *31*, 035006. <https://doi.org/10.1088/1361-665X/ac4ab5>
- Shami, Z. A., Shen, Y., Giraud-Audine, C., Touzé, C., & Thomas, O. (2022). Nonlinear dynamics of coupled oscillators in 1:2 internal resonance: Effects of the non-resonant quadratic terms and recovery of the saturation effect. *Meccanica*, *57*, 2701–2731. <https://doi.org/10.1007/s11012-022-01566-w>
- Shami, Z. A., Giraud-Audine, C., & Thomas, O. (2023). A nonlinear tunable piezoelectric resonant shunt using a bilinear component: Theory and experiment. *Nonlinear Dynamics*, *111*, 7105–7136. <https://doi.org/10.1007/s11071-022-08217-5>
- Shami, Z. A., Giraud-Audine, C., & Thomas, O. (2023). Saturation correction for a piezoelectric shunt absorber based on 2:1 internal resonance using a cubic nonlinearity. *Smart Materials and Structures*, *32*, 055024. <https://doi.org/10.1088/1361-665X/acc994>
- Shaw, S., & Pierre, C. (1991). Nonlinear normal modes and invariant manifolds. *Journal of Sound and Vibration*, *150*(1), 170–173.
- Shen, Y., Béreux, N., Frangi, A., & Touzé, C. (2021). Reduced order models for geometrically nonlinear structures: Assessment of implicit condensation in comparison with invariant manifold approach. *European Journal of Mechanics - A/Solids*, *86*, 104165.
- Sieber, J., & Krauskopf, B. (2008). Control based bifurcation analysis for experiments. *Nonlinear Dynamics*, *51*, 365–377.
- Simo, J. C., & Fox, D. D. (1989). On a stress resultant geometrically exact shell model. Part i: Formulation and optimal parametrization. *Computer Methods in Applied Mechanics and Engineering*, *72*(3), 267–304.
- Simo, J. C., & Vu-Quoc, L. (1988). On the dynamics of rods undergoing large motions - a geometrically exact approach. *Computer Methods in Applied Mechanics and Engineering*, *66*, 125–161.
- Simo, J. C., Fox, D. D., & Rifai, M. S. (1990). On a stress resultant geometrically exact shell model. Part III: Computational aspects of the nonlinear theory. *Computer Methods in Applied Mechanics and Engineering*, *79*(1), 21–70.
- Sonneville, V., Cardona, A., & Brüls, O. (2014). Geometrically exact beam finite element formulated on the special Euclidean group SE(3). *Computer Methods in Applied Mechanics and Engineering*, *268*, 451–474.
- Thomas, O., & Bilbao, S. (2008). Geometrically non-linear flexural vibrations of plates: In-plane boundary conditions and some symmetry properties. *Journal of Sound and Vibration*, *315*(3), 569–590. <https://doi.org/10.1016/j.jsv.2008.04.014>
- Thomas, O., Touzé, C., & Chaigne, A. (2003). Asymmetric non-linear forced vibrations of free-edge circular plates, part 2: Experiments. *Journal of Sound and Vibration*, *265*(5), 1075–1101. [https://doi.org/10.1016/S0022-460X\(02\)01564-X](https://doi.org/10.1016/S0022-460X(02)01564-X)
- Thomas, O., Touzé, C., & Chaigne, A. (2005). Non-linear vibrations of free-edge thin spherical shells: Modal interaction rules and 1:1:2 internal resonance. *International Journal of Solids and Structures*, *42*(11–12), 3339–3373. <https://doi.org/10.1016/j.ijsolstr.2004.10.028>

- Thomas, O., Touzé, C., & Luminais, É. (2007). Non-linear vibrations of free-edge thin spherical shells: Experiments on a 1:1:2 internal resonance. *Nonlinear Dynamics*, 49(1–2), 259–284. <https://doi.org/10.1016/j.ijssolstr.2004.10.028>
- Thomas, O., Deü, J.-F., & Ducarne, J. (2009). Vibration of an elastic structure with shunted piezoelectric patches: Efficient finite-element formulation and electromechanical coupling coefficients. *International Journal of Numerical Methods in Engineering*, 80(2), 235–268. <https://doi.org/10.1002/nme.2632>
- Thomas, O., Mathieu, F., Mansfield, W., Huang, C., Trolier-McKinstry, S., & Nicu, L. (2013). Efficient parametric amplification in MEMS with integrated piezoelectric actuation and sensing capabilities. *Applied Physics Letters*, 102(16), 163504. <https://doi.org/10.1063/1.4802786>
- Thomas, O., Sénéchal, A., & Deü, J. F. (2016). Hardening/softening behaviour and reduced order modelling of nonlinear vibrations of rotating cantilever beams. *Nonlinear Dynamics*, 86(2), 1293–1318. <https://doi.org/10.1007/s11071-016-2965-0>
- Touzé, C. (2003). A normal form approach for non-linear normal modes. Publications du LMA, numéro 156. ISBN: 2-909669-20-3.
- Touzé, C., & Amabili, M. (2006). Non-linear normal modes for damped geometrically non-linear systems: Application to reduced-order modeling of harmonically forced structures. *Journal of Sound and Vibration*, 298(4–5), 958–981.
- Touzé, C., & Thomas, O. (2006). Non-linear behaviour of free-edge shallow spherical shells: Effect of the geometry. *International Journal of Non-linear Mechanics*, 41(5), 678–692. <https://doi.org/10.1016/j.ijnonlinmec.2005.12.004>
- Touzé, C., Thomas, O., & Chaigne, A. (2002). Asymmetric non-linear forced vibrations of free-edge circular plates, part 1: Theory. *Journal of Sound and Vibration*, 258(4), 649–676. <https://doi.org/10.1006/jsvi.2002.5143>
- Touzé, C., Thomas, O., & Chaigne, A. (2004). Hardening/softening behaviour in non-linear oscillations of structural systems using non-linear normal modes. *Journal of Sound Vibration*, 273(1–2), 77–101. <https://doi.org/10.1016/j.jsv.2003.04.005>
- Touzé, C., Thomas, O., & Huberdeau, A. (2004). Asymptotic non-linear normal modes for large amplitude vibrations of continuous structures. *Computers and Structures*, 82(31–32), 2671–2682. <https://doi.org/10.1016/j.compstruc.2004.09.003>
- Touzé, C., Camier, C., Favraud, G., & Thomas, O. (2008). Effect of imperfections and damping on the type of nonlinearity of circular plates and shallow spherical shells. *Mathematical Problems in Engineering*, page ID 678307. <https://doi.org/10.1155/2008/678307>
- Touzé, C., Thomas, O., & Amabili, M. (2011). Transition to chaotic vibrations for harmonically forced perfect and imperfect circular plates. *International Journal of Non-linear Mechanics*, 46(1), 234–246. <https://doi.org/10.1016/j.ijnonlinmec.2010.09.004>
- Touzé, C., Vizzaccaro, A., & Thomas, O. (2021). Model order reduction methods for geometrically nonlinear structures: A review of nonlinear techniques. *Nonlinear Dynamics*, 105, 1141–1190. <https://doi.org/10.1007/s11071-021-06693-9>
- Vakakis, A. F. (1997). Non-linear normal modes and their applications in vibration theory: An overview. *Mechanical Systems and Signal Processing*, 11(1), 3–22.
- Vakakis, A. F., Manevitch, L. I., Mikhlin, Y. V., Philipchuck, V. N., & Zevin, A. A. (1996). *Normal modes and localization in non-linear systems*. New-York: Wiley.
- Vakilinejad, M., Grolet, A., & Thomas, O. (2020). A comparison of robustness and performance of linear and nonlinear Lanchester dampers. *Nonlinear Dynamics*, 100, 269–287. <https://doi.org/10.1007/s11071-020-05512-x>
- Vizzaccaro, A., Givois, A., Longobardi, P., Shen, Y., Deü, J.-F., Salles, L., Touzé, C., & Thomas, O. (2020). Non-intrusive reduced order modelling for the dynamics of geometrically nonlinear flat structures using three dimensional finite elements. *Computational Mechanics*, 66, 1293–1319. <https://doi.org/10.1007/s00466-020-01902-5>
- Vizzaccaro, A., Salles, L., & Touzé, C. (2021). Comparison of nonlinear mappings for reduced-order modeling of vibrating structures: Normal form theory and quadratic manifold method with modal derivatives. *Nonlinear Dynamics*, 103, 3335–3370.

- Vizzaccaro, A., Shen, Y., Salles, L., Blahoš, J., & Touzé, C. (2021). Direct computation of nonlinear mapping via normal form for reduced-order models of finite element nonlinear structures. *Computer Methods in Applied Mechanics and Engineering*, 384, 113957.
- Vizzaccaro, A., Opreni, A., Salles, L., Frangi, A., & Touzé, C. (2022). High order direct parametrisation of invariant manifolds for model order reduction of finite element structures: Application to large amplitude vibrations and uncovering of a folding point. *Nonlinear Dynamics*, 110, 525–571.
- Vizzaccaro, A., Gobat, G., Frangi, A., & Touzé, C. (2024). Direct parametrisation of invariant manifolds for non-autonomous forced systems including superharmonic resonances. *Nonlinear Dynamics*.
- Volvvert, M., & Kerschen, G. (2021). Phase resonance nonlinear modes of mechanical systems. *Journal of Sound and Vibration*, 511, 116355. <https://doi.org/10.1016/j.jsv.2021.116355>
- Volvvert, M., & Kerschen, G. (2022). Resonant phase lags of a duffing oscillator. *International Journal of Non-linear Mechanics*, 146, 104150.
- von Kármán, Th. (1910). Festigkeitsprobleme im maschinenbau. *Encyklopädie der Mathematischen Wissenschaften*, 4(4), 311–385.
- Woinowsky-Krieger, S. (1950). The effect of axial force on the vibration of hinged bars. *Journal of Applied Mechanics*, 17, 35–36.
- Woiwode, L., Balaji, N. N., Kappauf, J., Tubita, F., Guillot, L., Vergez, C., Cochelin, B., Grolet, A., & Krack, M. (2020). Comparison of two algorithms for harmonic balance and path continuation. *Mechanical Systems and Signal Processing*, 136, 106503. <https://doi.org/10.1016/j.ymssp.2019.106503>
- Wriggers, P. (2008). *Nonlinear finite element methods*. Springer.
- Younis, M. I. (2011). *MEMS linear and nonlinear statics and dynamics*. Springer.
- Zhou, J., Hagiwara, T., & Araki, M. (2003). Spectral characteristics and eigenvalues computation of the harmonic state operators in continuous-time periodic systems. *Systems & Control Letters*, 53(2), 141–155.